Dissertation

submitted to the

Combined Faculty of Mathematics, Engineering and Natural Sciences

of Heidelberg University, Germany

for the degree of

Doctor of Natural Sciences

Put forward by

Mattis Magg

born in Ulm

Oral examination: 25.05.2022

The Cosmological Transition to Metal-Enriched Star-Formation

Referees Prof. Dr. Ralf S. Klessen

PD. Dr. Anna Pasquali

Abstract

The first stars in the Universe mark the beginning of the epoch referred to as Cosmic Dawn. Due to their metal-free nature, they are believed to be distinctively different from present-day stars. While they are considered to be important in shaping the early Universe, little is known about their properties. This thesis addresses several indirect methods of constraining these properties, with a particular focus on the transition from metal-free to metal-enriched star formation. To this end, I employ and develop a variety of analytical estimates, semi-analytical models and a numerical simulation. By analysing the non-detection of metal-free stars, I confirm that these stars must on average have been far more massive than present-day stars. An analytical model and a careful review of numerical simulations demonstrate that the interaction between the first supernovae and their ambient medium is key to understanding the most metal-poor stars known today. With a simulation of the massive metal-free stars exploding as pair-instability supernovae, I highlight the tension implied by the non-detection of their nucleosynthetic fingerprint. Finally, I use a semi-analytical model to reveal the sensitivity of future 21 cm absorption detections to the time-delay between the first supernovae and the second generation of stars. The results, tools, and methods of this thesis will find application in future theoretical studies and in the analysis of upcoming observations.

Zusammenfassung

Die ersten Sterne im Universum entstanden am Anfang der Epoche die als kosmische Dämmerung bekannt ist. Da sie von Natur aus metallfrei sind, wird angenommen, dass diese Sterne sich stark von den heutigen Sternen unterscheiden. Obwohl sie einen wichtigen Einfluss auf das frühe Universum ausüben, ist nur wenig über ihre Eigenschaften bekannt. In dieser Arbeit werde ich mehrere unterschiedliche Methoden verwenden um ihre Eigenschaften durch Beobachtungen einzugrenzen. Der Fokus liegt dabei auf dem Übergang von metallfreier zu mit metallen angereicherter Sternentstehung. Zu diesem Zweck werden analytische Abschätzungen, semi-analytische Modelle sowie eine numerische Simulation entwickelt und eingesetzt. Durch Analyse der bisherigen Nichtbeobachtung metallfreier Sterne bestätige ich, dass sie im Durchschnitt viel massereicher waren als heutige Sterne. Ein analytisches Modell und eine gründliche Auswertung vorhandener Simulationen unterstreicht, dass die Interaktion zwischen den ersten Supernovae und ihrer Umgebung eine zentrale Rolle im Verständnis heutiger metallarmer Sterne spielt. Eine Simulation massereicher metallfreier Sterne und deren Paarinstabilitätssupernovae unterstreicht die Diskrepanz zwischen Modellen dieser Supernovae und der Nichtbeobachtung des vorhergesagten nukleosynthetischen Fingerabdrucks. Mit einem semi-analytischen Modell entdecke ich, dass zukünftige 21 cm Absorptionsbeobachtungen Hinweise auf den zeitlichen Abstand der ersten Supernovae und der zweiten Sternengeneration enthalten werden. Die Ergebnisse, Methoden und Werkzeuge die in dieser Arbeit entwickelt wurden werden in zukünftigen theoretischen Modellen und in der Analyse neuer Beobachtungsdaten Anwendung finden.

Contents

1

Introduction: the first stars

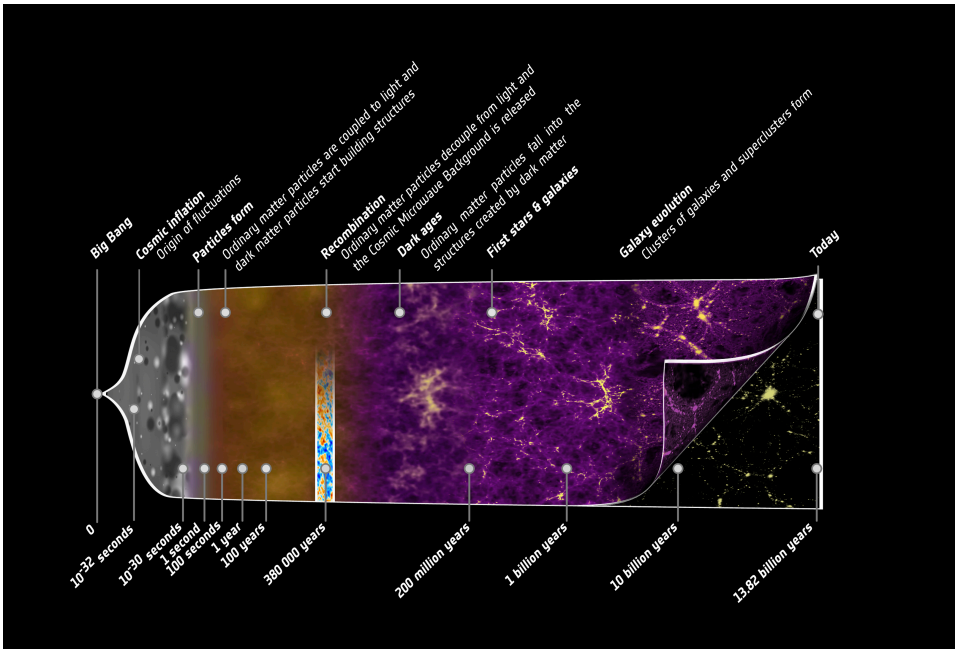

Figure 1.1: A depiction of the history and evolution of the Universe. Image by © ESA, C. Carreau.

The first stars in the Universe are thought to have formed around 60 Myr after the Big Bang (Naoz et al., 2006, Fialkov et al., 2012). These metal-free, so-called Population III (or Pop III), stars mark the end of the cosmic Dark Age, start the process of reionization and shape the early Universe (Bromm, 2013, Dayal & Ferrara, 2018). Yet, little is known about their nature and their properties remain poorly constrained (Greif, 2015). This thesis investigates several avenues to constrain the properties of the first stars and explore the implications of the transition from metal-free to metal-enriched (Population II or Pop II) star formation.

1.1 Setting the stage: the Universe before star formation

1.1.1 Big Bang, recombination and the cosmic microwave background

According to the cosmological standard model (see also a depiction of the evolution of the Universe in Fig. 1.1), the Λ cold dark matter (ΛCDM) model, the Universe began 13.8 billion years ago (Planck Collaboration et al., 2016a), from a point-like extremely hot, dense state, which is commonly referred to as the Big Bang. In the first few minutes, the Universe is hot and dense enough for the first chemical elements to form. The mix of plasma and photons that is created in this process cools as the

Universe expands. Tiny initial density fluctuations in dark matter increase due to gravity. In contrast to dark matter, the baryons are interacting with the radiation and with that comes a large radiation pressure that prevents the baryons from forming similar density fluctuations. As the dark matter density fluctuations get larger, the deepening potential wells of the dark matter attract baryons and pull in the gas. The gas compresses and the radiation pressure rises until the collapse stalls and the gas expands again. Thus the gas density embedded in the dark matter structures oscillates (Sunyaev & Zeldovich, 1970, Peebles & Yu, 1970, Eisenstein et al., 2005), which is referred to as Baryon Acoustic Oscillations (BAOs). Around 400,000 years after the Big Bang, the mean photon energy falls sufficiently far below the ionization energy of atomic hydrogen for the gas to recombine and the Universe to become neutral. The photons are seen today as the cosmic microwave background (CMB). The BAOs mentioned above and the resulting variations in gas density are one of the causes for the observed anisotropies in the CMB. Additionally, the BAOs lead to large-scale gas-flows, which are – due to the sudden drop in the speed of sound at recombination – supersonic (Tseliakhovich & Hirata, 2010).

1.1.2 Structure formation

As the Universe expands the initial density perturbations in the matter distributions grow. Initially, the growth of the perturbations is linear. Once they grow large enough, the perturbations decouple from the Hubble flow and collapse. These collapsed objects are commonly referred to as haloes. Press & Schechter (1974) developed a theoretical framework that allows to investigating spherical halos, their properties, their evolution and the halo mass function (HMF) based on an initial power-spectrum of perturbations. A key result from this study is that structure formation in a ΛCDM universe is a hierarchical self-similar process in which smaller halos merge to form larger ones. This framework was extended by Bond et al. (1991), Lacey & Cole (1993) to allow the use of a Monte-Carlo method to construct possible merger-histories of a chosen halo. Further Sheth et al. (2001), extended the (Press & Schechter, 1974) description to describe haloes as ellipsoidal rather than spherical. This improved description matches the aspherical nature of the haloes and the HMF found in simulations much better.

The strong hierarchy of structures has since been established as one of the central features of the ΛCDM model. The *Millennium* simulations (Springel et al., 2005b) showed the fractal properties of dark matter structures and substructures in much

greater detail than what can be described with the analytical methods discussed above. These simulations predicted a large number of gravitationally bound dark matter substructures within the dark matter halo of the Milky Way, far larger than the number of observed satellite galaxies. This tension is part of the so-called small-scale crisis of the ΛCDM model and is subject to ongoing research (Bullock & Boylan-Kolchin, 2017). The *Millennium* simulations also demonstrated that relying solely on the above mentioned analytical methods for the description of dark matter structures and their evolution may lead to missing some very central features of structure formation. This initiated a significant effort to explore the formation of the Milky Way (Springel et al., 2008, Griffen et al., 2016, Garrison-Kimmel et al., 2014, Ishiyama et al., 2016) as well as structure formation at large scales (Boylan-Kolchin et al., 2009, Klypin et al., 2011, Ishiyama et al., 2021) with dark-matter-only simulations. These simulations also require advanced methods for finding haloes and for constructing the merger trees (Springel et al., 2001, Knollmann & Knebe, 2009, Behroozi et al., 2013a).

1.1.3 The onset of star formation

During the growth of haloes, they accumulate more and baryonic matter, until the matter becomes gravitationally unstable, collapses and forms the first stars. This is expected to occur in minihaloes, i.e., haloes with total masses of around $10^6\,\mathrm{M}_\odot$ (Glover, 2013, Hummel et al., 2012, Greif, 2015). The first star in the observable Universe is expected to form around a redshift of $z \approx 60$ in this fashion (Fialkov et al., 2012).

Several key-factors influence at which halo mass the gas can collapse. Primarily the collapse is governed by how quickly the gas can radiate away its thermal energy and cool. In the absence of metals, this cooling occurs primarily via emission from molecular hydrogen (Tegmark et al., 1997, Glover, 2013). Lyman-Werner (LW) radiation, i.e., radiation with photon energies in the range of 11.2–13.6 eV, can photodissociate molecular hydrogen inhibiting the cooling of the gas and delaying the collapse (Haiman et al., 2000, Machacek et al., 2001, O'Shea & Norman, 2008, Schauer et al., 2021). Additionally, radiation with a photon energy above 0.76 eV can photodissociate H^- ions, thus inhibiting the formation of H_2, which relies on these ions (Agarwal & Khochfar, 2015). The supersonic baryon streaming velocities mentioned above also delay the collapse (Greif et al., 2011b, Stacy et al., 2011, Fialkov et al., 2012, Naoz et al., 2013, Schauer et al., 2017a, 2019a). The reason for this

delay is that at the early stages the escape velocity from the minihaloes is smaller than the typical streaming velocities, and therefore gas does not become gravitationally bound to the halos as early as without streaming. A heated intergalactic medium (IGM) or an ionizing radiation background will also reduce the ability of the haloes to bind the gas. If the IGM is ionized the haloes generally only collapse if they can bind the heated gas. This is quantified by the virial temperature, which is the temperature corresponding to the escape velocity from the halo. Halos that can bind ionized gas, i.e., halos with a virial temperature of more than $T_{\rm vir} = 10^4\,{\rm K}$ are referred to as atomic cooling haloes. For a redshift z, the virial temperature corresponds to a mass limit of

$$M_{\rm vir} = 10^6\,{\rm M}_\odot \left(\frac{T_{\rm vir}}{1000\,{\rm K}}\right)^{1.5} \left(\frac{1+z}{10}\right)^{-1.5}. \tag{1.1}$$

A very strong ionizing radiation background can even push the mass-limit about an order of magnitude above the atomic cooling threshold (Visbal et al., 2016). If we are only interested in the first metal-free stars, the picture slightly simplifies, as there are no sources for ionizing or LW radiation. Despite the complexity of these effects, the current consensus is that haloes with masses around $10^6\,{\rm M}_\odot$ are expected to host the first stars in the Universe (Park et al., 2021, Kulkarni et al., 2021, Schauer et al., 2021).

1.2 The formation of the first stars: theoretical perspective

1.2.1 Hydrogen chemistry and cooling

Since the first stars (Population III or Pop III) stars are by definition free of metals, their formation sites cool predominantly via emission from molecular hydrogen. The detailed physics of the relevant chemistry and cooling processes are described in Glover (2013) and I give only a short summary here. The cooling by molecular hydrogen is inefficient for three main reasons: firstly at low densities ($n \lesssim 10^8\,{\rm cm}^{-3}$)the formation of H_2 occurs primarily via the reactions

$$H + e^- \longrightarrow H^- + \gamma \tag{1.2}$$

and

$$H^- + H \longrightarrow H_2 + e^-. \tag{1.3}$$

This formation channel is inefficient as the probability of the radiative attachment reaction (1.2) is small and because it is limited by the number of free electrons in the interstellar medium (ISM). Secondly, molecular hydrogen is a symmetric diatomic molecule, which means it has neither a dipole moment nor dipole transitions between the rotational and vibrational energy levels. Thus, excited states of the H_2 molecule can only radiatively decay via the much rarer quadrupole transitions. Thirdly, the hydrogen atoms are very light, which leads to a larger separation between the rotational energy levels in the H_2 molecule. The transition primarily responsible for the cooling of primordial gas is the transition between the $J = 0$ and the $J = 2$ rotational states. These levels are separated by an energy equivalent to a temperature of $T = 500\,\mathrm{K}$, which greatly diminishes the cooling capabilities of metal-free gas below this temperature.

For these reasons, the pristine star-forming gas can not cool below temperatures of around $T = 200\,\mathrm{K}$. Somewhat lower temperatures can be reached when considering the cooling by HD molecules (Glover & Abel, 2008). These temperatures are large in comparison to present-day molecular clouds, which, as we will see in the following, has important consequences for the properties of the first stars.

1.3 The origin of elements

1.3.1 Primordial nucleosynthesis

The first elements form in the first few minutes of the Universe. At this time, the Universe is hot and dense enough for some of the free protons and neutrons to fuse to form heavier elements. After this brief episode of nuclear fusion, the baryonic matter in the Universe is primarily composed of hydrogen and helium (^{4}He, Alpher et al., 1948). Since there are no stable nuclei with mass-numbers of 5 (helium+hydrogen) or 8 (helium+helium), no stable atoms more massive than helium can form from collisions of the two main constituents of the matter. This leads to a bottle-neck and only small traces of heavier elements form (specifically lithium and beryllium, for recent predictions see Fields et al., 2020). All heavier elements are originating in astrophysical objects, mostly stars, and I will follow Kippenhahn et al. (2012) for the description of the nucleosynthetic processes.

1.3.2 Hydrogen burning

Main-sequence stars fuse hydrogen to helium in their centres. There are two reaction processes for this fusion: the pp-chain and the CNO-cycle. The pp-chain typically becomes active at temperatures of 4×10^6 K. It is a series of proton-proton collisions and β^+ decays, that progressively turn hydrogen into deuterium, tritium, ^{3}He. Finally, ^{4}He is fused from ^{3}He via three different reactions. As the reaction rates, and therefore the energy production increases with increasing temperatures, the reaction process acts as a thermostat and stabilizes[1] the stellar core against further contraction. The CNO-cycle is a fusion process in which carbon, nitrogen and oxygen capture free protons and turn protons into neutrons via β^+ decays until a ^{4}He nucleus is split off and the cycle can repeat. To become active, the CNO-cycle needs only trace amounts of CNO elements, and somewhat higher temperatures of at least $T \approx 1.5 \times 10^7$ K. This process has a much steeper dependence on temperature than the pp-chain and is, therefore, a much better thermostat. It is the dominant process in massive main-sequence stars, whereas the pp-chain dominates in low-mass stars.

1.3.3 α elements

When helium fusion ignites at the tip of the red giant branch, the stellar core consists predominantly of helium. Thus, further elements are formed by the reaction of several ^{4}He nuclei (also called α particles). Two ^{4}He nuclei react to the unstable ^{8}Be nucleus, and some of these react with an additional ^{4}He to ^{12}C before they can decay. Once the carbon has built up sufficiently it can further absorb α particles to form ^{16}O and ^{20}Ne. When even larger temperatures are reached, a core consisting mostly of ^{12}C and ^{16}O forms. After helium fusion, collisions of two ^{12}C nuclei yield ^{24}Mg which then decays. A significant fraction of these decays yield more α particles, allowing the synthesis of heavier and heavier elements (Mg, Si, S, Ar, Ca, Ti, Cr and Fe) by α capture. The elements that are predominantly formed in these hydrostatic burning processes, i.e., C, Ne, Mg, Si, S, Ar, Ca and Ti are commonly referred to as α elements.

[1] Systems bound by self-gravity have, according to the virial theorem, a negative heat capacity. Thus, when adding energy to the star, it expands and cools. Therefore, an increased reaction rate cools the stellar interior.

1.3.4 Iron group

The majority of elements around iron (referred to as the iron group) originates in supernovae (SNe), both type Ia and core-collapse. In SNe, the material is so hot and dense that all nuclear reaction rates that preserve the number of protons and the number of neutrons are in statistical equilibrium. The elemental abundances are determined by the binding energy of the elements. This is a stark contrast to the dependence on the available reactions and on whether nuclei can be made by α absorption that we have seen above. In nuclear statistical equilibrium, the most common elements are the ones with the largest binding energy per nucleon, mostly Ni and Fe, but also Co, Mn and Cr.

1.3.5 Neutron-capture

Elements beyond the iron group, i.e., with mass numbers above 56, can only be synthesized by a series of neutron-captures and β decays. To facilitate these reactions, a large number of free neutrons is required. Generally, neutrons start being captured by seed-nuclei from the iron group. The characteristic outcome of the neutron-capture depends on the duration of the process and the abundance of free neutrons.

In the slow neutron-capture process (or s-process), the time-scale for neutron-capture is larger than the half-life of the neutron-rich unstable heavy isotopes. This leads to the population of nuclei evolving along the valley of stability. The s-process occurs mainly in asymptotic giant branch stars which eject their outer shells.

The other extreme is the r-process (or rapid neutron-capture process), in which extremely large neutron fluxes lead to neutron-capture time-scales much smaller than the β decay half-lives of the neutron-rich heavy nuclei. Thus the nuclei accumulate mass first and then, once the process ends, decay towards the valley of stability. Due to the large number of neutrons required, the site of the r-process has been a long-standing question. The detection of the neutron-star merger GW170817 including the optical counter-part (Abbott et al., 2017) and subsequent analysis (Watson et al., 2019) has confirmed that neutron star mergers are a site of the r-process.

Since the r-process and the s-process progress very differently, both come with a unique abundance pattern. The s-process is the primary source of Sr and Ba. The heaviest long-lived radioactive elements, e.g., uranium and thorium, can only be formed in the r-process.

1.4 Life and death of the first stars

1.4.1 Main-sequence and post-main-sequence evolution

A key to both understanding the formation of the first stars and their interaction with their environment lies in their evolution and their final fates. I will here give a brief summary of their stellar evolution and emphasize the differences to later generations of stars. For the description for their main-sequence and post-main-sequence evolution, I will follow Kippenhahn et al. (2012) for the general stellar evolution and Marigo et al. (2001) for the Pop III specific details.

Stars generally start their main-sequence life when nuclear fusion in their core ignites. During the main-sequence, the stars fuse hydrogen to helium. This fusion typically starts at temperatures of 4×10^6 K. The CNO-cycle ignites at $T \approx 1.5 \times 10^7$ K and, as the reaction rates rise steeply with rising temperature, the CNO-cycle quickly dominates the fusion. However, this occurs only in stars that are massive enough to reach these temperatures during their main-sequence.

When the hydrogen in the stellar core is exhausted, nuclear fusion continues in the outer shells of the star, leading to a contraction and heating of the stellar core, and an expansion of the outer layers. The star becomes a red giant. The fusion occurs in layers further and further away from the centre of the star until the centre is hot enough for helium to fuse to heavier elements. The steep rise in luminosity caused by the ignition of helium-burning is called the helium flash. In principle, elements as heavy as iron can form in a way similar to this. However, not all stars are massive enough to sustain the required internal pressure for fusing such elements. The Sun, for example, will form a degenerate carbon-oxygen core at the end of the helium-burning phase, eject its outer layers as a planetary nebula and become a white dwarf.

Low mass Pop III stars are expected to evolve similarly to present-day stars. Due to the lack of C, N and O, helium can only be fused via the pp-chain, not via the CNO-cycle. This means that stars that normally can fuse hydrogen into helium via the CNO-cycle have a weaker increase of reaction rates with temperature. In hydrostatic equilibrium, these stars will therefore have higher internal temperatures. Additionally, the opacity of the stellar atmosphere is lower due to the lack of metals, which means it is possible to see deeper into the star. For these two reasons, main-sequence metal-free stars are bluer and more luminous than solar metallicity stars of the same mass. This is important as it leads to higher ionizing photon emission

rates compared to present-day stars.

Higher mass stars are eventually able to fuse carbon and oxygen in their cores via the tripe-alpha process. If these newly fused elements mix into the outer layers, the CNO-cycle can be ignited during the later evolutionary phases of the stars. Even more massive Pop III stars ($M \geq 20\,\mathrm{M}_\odot$) reach sufficient internal temperatures to form trace amounts of C and O in their core during their main-sequence. As relative CNO-abundances of $\sim 10^{-10}$ are sufficient for the CNO-cycle, these stars ignite CNO-cycle in their core before they leave the main-sequence. This leads to a short-lived additional loop along the evolutionary track of massive Pop III stars in the Hertzsprung-Russell diagram.

Massive metal-rich stars lose a significant fraction of their mass during their life via radiation-driven stellar winds. Atoms, ions and dust particles in the upper stellar atmosphere or in the vicinity of the star absorb photons from the star and re-emit them in a random direction. Thus, there is a net momentum transfer in radially outwards direction, away from the star. The absorption occurs either due to transitions between the energy levels of the atoms and ions (line-driven winds) or due to continuum absorption in the dust particles (dust-driven wind). Notably for line-driven winds to be effective, there need to be many different absorption lines, as each line only absorbs in a very small range of photon energies, and, unless the atoms are accelerated enough for Doppler shifts to become relevant, the photons within that energy-range are quickly exhausted. Pop III stars by definition do not have metals, except for the ones they synthesised. Thus there are no metal-lines to drive winds and no dust. Therefore, it is thought that the mass-loss of non-rotating Pop III stars is negligibly small (Marigo et al., 2003).

1.4.2 The final fates of Pop III stars by mass

The final fate of a star is primarily determined by its initial mass, and by the mass-loss it incurs during its life. I will only discuss non-rotating stars here and discuss rotation separately in Section 1.4.5. As we discussed before, this also means that we can neglect mass-loss in this section. The final fates of such non-rotating Pop III stars as a function of initial mass are summarized in Fig. 1.2.

Metal-free stars below around 8–12 $\mathrm{M}_\odot$ are not expected to explode as SN at the end of their lives (Heger & Woosley, 2002, 2010, Kobayashi et al., 2011), rather they end up as a white dwarf. These white dwarfs consist mostly of carbon and oxygen and they are stabilized by the Fermi-pressure of the free electrons. If they accrete

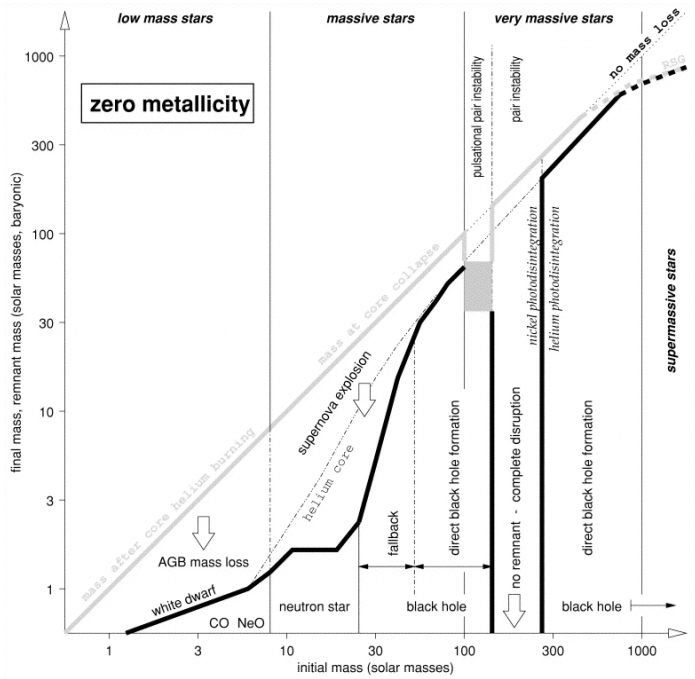

Figure 1.2: Final fates of non-rotating Pop III stars as a function of their initial mass. This figure is from Heger & Woosley (2002) and has been derived with one-dimensional stellar evolution and SN models.

sufficient mass to exceed the Chandrasekhar limit (Chandrasekhar, 1931), either by merging with another white dwarf or via Roche-lobe overflow from a companion star, they will explode as type Ia SNe. As these white dwarfs are dominated by the carbon and oxygen fused during their lives, Pop III white dwarfs are unlikely to be significantly different from later populations.

Stars in the mass range $10\,\mathrm{M}_\odot \lesssim M \lesssim 40\,\mathrm{M}_\odot$ explode as core-collapse supernovae (CCSNe) (Heger & Woosley, 2002, Nomoto et al., 2013). These SNe are similar to the type II SNe of present-day massive stars. Their explosion energy is thought to be around 1 foe and they yield a large amount of α and iron-group elements (see Section 1.3). After the explosion a compact remnant, either a neutron star or a black hole remains.

At masses of around $40\,\mathrm{M}_\odot$ and above, a CCSN is typically not energetic enough to eject large amounts of matter out of the collapsing star. Largely, the matter of the star ends up in the compact remnant, a black hole.

In the mass range of $140\,\mathrm{M}_\odot \lesssim M \lesssim 260\,\mathrm{M}_\odot$ Pop III stars are thought to explode as pair-instability supernovae (PISNe) (Heger & Woosley, 2002, Heger et al., 2003). With explosion energies of up to $\sim$100 foe, these SNe are very energetic. The star is fully destroyed and no compact remnant remains. At masses below this mass range, the pair-instability is not quite energetic enough to disrupt the star and one or several pair-pulsations occur, in which the outer shells of the star are ejected. At masses above this mass range, due to photo-disintegration of the synthesized nuclei, there is no SN, and the entire star collapses into a black hole.

1.4.3 Core-collapse supernovae

CCSNe occur at the end of the lives of massive Pop III as well as in massive metal-enriched stars. Here, I will give a qualitative summary (following Branch & Wheeler, 2017) of the stages of a CCSN. The qualitative processes are similar in metal-free and metal-enriched stars.

When the star approaches the end of its life, an increasingly massive iron core forms. As iron and nickel have the two nuclei with the largest binding energy per baryon, no further energy can be generated by the fusion of these nuclei. The forming iron core is surrounded by onion-like layers composed of different elements (Si, Mg, O, C, He and H), ordered by atomic mass, with the inner shells containing the heaviest atoms. Once fusion ceases in the core it increasingly contracts and heats up. During this process, more and more protons are turned into neutrons via

electron capture. This reduces the number of available electrons for stabilizing the core with electron-degeneracy pressure. Additionally, thermal energy gets converted into the binding energy of the baryons and part of the energy escapes via neutrinos. This rapidly energy loss leads to a runaway, homological collapse of the core of the star.

Due to the rapidly rising degeneracy pressure of the nucleons, this collapse comes to a sudden halt when the density reaches nuclear levels. As the collapse of the outer shells of the iron core occurs at supersonic velocities at this point, the collapsing matter crashes onto the newly formed compact centre and bounces off. This core-bounce leads to a shock-wave travelling outwards. Due to dense matter still rapidly collapsing onto the centre, this shock quickly stalls and accumulates mass. When the stalled shock becomes dense enough, it becomes optically thick to the energetic neutrinos originating from the runaway neutron-captures in the compact remnant. These neutrinos push the shock outwards and revive the shock.

The revived shock travels outwards through the star, the extreme densities and pressures enable nuclear fusion of elements such as magnesium and iron as it travels through the onion-like structure of layers. Most layers are unbound in this process and the ejected material enriches the ISM with the synthesized elements. However, how much of the star is ejected in this fashion depends on the exact explosion energy and mass of the remnant.

It should be noted that this picture is strongly simplified. The involved physics are very complex and remain extremely computationally challenging to simulate. Most models of CCSNe are one-dimensional, and assume spherical symmetry, with mixing and other 3-D effects being included via parametrized empirical models (Ishigaki et al., 2014, Heger & Woosley, 2010, Chen et al., 2017a). Recently 3D simulations of such SNe have become increasingly feasible (Janka et al., 2016, Chan et al., 2018, 2020, Bollig et al., 2021), but often these models fail to explode (e.g. Chan et al., 2018). This indicates that the theoretical models are still insufficient or lacking in physics.

1.4.4 Pair-instability supernovae and pair-pulsation

Very massive metal-free stars are predicted to have a unique way of exploding, which was first predicted by Rakavy & Shaviv (1967). For the qualitative description of the processes and phases of these SNe, I will follow Branch & Wheeler (2017) and Heger & Woosley (2002), Heger et al. (2003). At the end of the central carbon

burning in a massive star, the core becomes extremely hot, such that a part of thermal radiation reaches photon energies above $E_\gamma = 1022\,\mathrm{keV}$. At this point, the radiation starts to engage in electron-positron pair creation. As the radiation pressure is vital to stabilize the core against gravitational collapse, the sudden drop in radiation pressure caused by this loss of photons destabilizes the core. As the core contracts, it heats up and more radiation can engage in pair production. Thus the radiation pressure decreases further, leading to runaway collapse.

This runaway collapse, however, causes rapid nuclear fusion in the core. A large fraction of the stellar mass is converted into ^{56}Ni which releases up to 100 foe in a short time. How energetic the pair-instability mostly depends on the mass of the helium core that formed inside the star. At core masses in the range of $40\,\mathrm{M}_\odot \lesssim M_\mathrm{He} \lesssim 65\,\mathrm{M}_\odot$ this processes releases around 1 foe of energy, which is insufficient to disrupt the core of the star completely. Rather, the outer layers of the star get ejected. These events are referred to as pulsational PISNe and several such pulses can occur in succession. At core masses in the range $65\,\mathrm{M}_\odot \lesssim M_\mathrm{He} \lesssim 130\,\mathrm{M}_\odot$ the star is fully disrupted by the pair-instability, and no compact remnant remains. Due to a large amount of radioactive ^{56}Ni ejected by PISNe they can be extremely bright and are potentially observable up to very high redshifts (Whalen et al., 2013a).

The heavy elements formed during PISNe are formed by α-capture. As Pop III stars initially contain no CNO-elements, at the time of the SN there are neither the required neutrons nor the seed elements for the s-process (see Section 1.3.5). These circumstances lead almost exclusively to the production of elements with even atomic numbers. Therefore, the difference in abundances of neighbouring even- and odd-numbered elements is far larger in these SNe than in the sun (Heger & Woosley, 2002)

1.4.5 Stellar rotation

Stellar rotation is known to have an important effect on stellar evolution and the internal structure of stars (Yoon et al., 2012, Maeder & Meynet, 2000). The two main effects relevant for Pop III stars are mass-loss and the increased size of the convective cores. These effects are summarized in (Meynet & Maeder, 2017).

Stars that are rapidly rotating are usually not rotating as a solid body, but rather show differential rotation. Thus, there are additional shear forces between the layers of the star. These shear forces lead to additional convection and therefore additional mixing in the stellar interior and larger convective cores. As the final mass of the

helium core is the deciding factor for PISNe, rotating stars can encounter PISNe at lower stellar masses than non-rotating stars (Chatzopoulos & Wheeler, 2012, Takahashi et al., 2018). The effects on the stellar structure can also change the nucleosynthetic yields, both of the hydrostatic- and the explosive nucleosynthesis (Takahashi et al., 2014, Choplin et al., 2017, Choplin & Hirschi, 2020). As the rotation leads to some of the CCSNe occurring in blue rather than in red supergiants, the SN light-curves are also affected (Murphy et al., 2021).

If stars reach large enough rotation velocities for the centrifugal force to overcome the stellar surface gravity, they will lose a substantial amount of mass. Murphy et al. (2021) find that this is the case for Pop III stars with masses above $M = 60\,\mathrm{M}_\odot$. How large the effect of the mass loss is and which stars are affected is strongly dependent on the initial rotation rates, which are still highly uncertain. Very large rotation rates can additionally lead to several exotic SNe, such as magneto-rotational jet-SNe (Nishimura et al., 2015) or collapsars (Siegel et al., 2019). Altogether stellar rotation introduces various important, yet poorly understood changes to the life and death of the first stars.

1.4.6 Present day star formation

The multiphase interstellar medium

Star formation in the local Universe occurs by gravitational collapse of molecular clouds in the ISM. Thus, it is instructive to start by looking at the ISM. I will follow the description of the ISM given in Draine (2011). The ISM separates into several relatively discrete phases:

- The **hot ionized medium** consists of very diffuse gas with hydrogen nucleon number densities of only $n \sim 0.004\,\mathrm{cm}^{-3}$ and temperatures of $T \gtrsim 10^{5.5}\,\mathrm{K}$. This phase fills around half of the volume of the Milky Way. It is found primarily in SN remnants and the hot corona of the Milky Way

- The **warm ionized medium** or **HII gas** is the less diffuse ionized gas. The temperature is maintained mostly by ionizing radiation and photoelectric heating from dust. Typically it has temperatures of $T \approx 10^4\,\mathrm{K}$ and spans a wide range of densities $0.2\,\mathrm{cm}^{-3} \lesssim n \lesssim 10^4\,\mathrm{cm}^{-3}$.

- The **warm neutral medium** is mostly atomic hydrogen with temperatures of around $T = 5000\,\mathrm{K}$ and densities $n = 0.6\,\mathrm{cm}^{-3}$. Most of the gas mass is

found in this medium. This phase is similar to the warm ionized medium, except that there is insufficient ionizing radiation to keep the medium ionized.

- The **cold neutral medium** is much denser ($n \approx 30\,\mathrm{cm}^{-3}$) and has typical temperatures of only 100 K.

- **Molecular clouds** form when sufficiently large column densities are reached for the gas to self-shield from photodissociating radiation. Molecular clouds typically have densities of $n = 100\,\mathrm{cm}^{-3}$ and contain collapsing clumps of much higher densities. Their temperatures are in the range of $10 - 50\,\mathrm{K}$.

Molecular clouds are especially interesting, as they host star-forming regions. The molecular clouds themselves are hierarchically structured (see e.g. Stutzki et al., 1998), i.e., they are composed of smaller dense clumps and larger, more diffuse inter-clump structures. Star formation is governed by the collapse and fragmentation of these clouds.

The most simple model of star formation

The first discussion of the stability of molecular clouds goes back to Jeans (1902). Even without the observational tools used today to infer the properties of the ISM, e.g. with the complete lack of radio or infrared observations, it was evident that the stability of an interstellar cloud is determined by the interplay of gravity and gas physics. This very first stability analysis can be used to derive a strongly simplified estimate of star formation rates (SFRs) in molecular clouds. Following the Jeans (1902) stability analysis a uniform homogeneous spherical cloud is gravitationally unstable if its mass is larger than the Jeans Mass

$$M_{\mathrm{Jeans}} = \frac{\pi^{5/2}}{6} \frac{{\mathrm{c}_s}^3}{G^{3/2}\rho^{1/2}}, \tag{1.4}$$

where c_s is the speed of sound, G is the gravitational constant and ρ is the initial average density of a cloud. For typical conditions in the molecular phase of the ISM ($c_s \approx 0.2\,\mathrm{km\,s}^{-1}$, $\rho \approx 10^{-21}\,\mathrm{g\,cm}^{-3}$, taken from Krumholz, 2011), the Jeans mass is on the order of tens of solar masses. Molecular clouds of $\sim 10^5\,\mathrm{M}_\odot$ should therefore be Jeans unstable. Once the gravitational collapse sets in, the density increases. This also enhances collision and cooling rates and therefore gravity becomes more and more dominant. Thus, thermal pressure can be neglected for simplicity. The

gas then collapses in a free fall time:

$$t_{\rm ff} = \sqrt{\frac{3\pi}{32G\rho}}. \tag{1.5}$$

If the cloud initially has a mass of $M_{\rm cloud}$ and all of the gas ends up in the stars, the star formation rate can be estimated as

$$\mathrm{SFR} = \frac{M_{\rm cloud}}{t_{\rm ff}} \approx 0.06\,\mathrm{M_\odot\,yr^{-1}}, \tag{1.6}$$

where the estimate has been done with $M_{\rm cloud} = 10^5\,\mathrm{M_\odot}$ and a particle number density of $n = 500\,\mathrm{cm^{-3}}$, which are typical values for molecular clouds (e.g. Sanders et al., 1985).

Considering that there are thousands of clouds like these (Sanders et al., 1985) and the actual SFR of the Milky Way is about 1-2 $\mathrm{M_\odot\,yr^{-1}}$ (Robitaille & Whitney, 2010) this simplified estimate overpredicts the star formation rate by more than an order of magnitude. Additionally, three dimensional spherical Jeans instabilities collapse outside-in, meaning the large scale density perturbations grow fastest. Therefore, all the cloud mass is expected to collapse into a single object, rather than fragmenting into many stars, leading to much more massive stars than we observe.

The strong discrepancy between observations and this simplified picture is caused by all the neglected properties of molecular clouds and physical processes that shape their evolution.

The collapse of molecular clouds

Since the earliest studies, the field of star formation has produced a complex body of observational insights and theoretical frameworks. I will only give a short summary of these topics and follow the reviews by (McKee & Ostriker, 2007) and (Girichidis et al., 2020) for the qualitative description.

Whether and how molecular clouds collapse depends on various physical processes. Among the important effects are:

- Gravity: how strong is the gravitational self-attraction of the cloud.
- Gas pressure: how well is the thermal pressure able to stabilize the cloud.
- Metallicity or chemical composition: these can significantly impact the ability of the gas to cool.

- Turbulence: how fast are the turbulent motions, is the turbulence driving compressive, and how does the turbulent kinetic energy compare to the gravitational binding energy.

- Magnetic fields: both the strength and the direction of the magnetic fields can impact the stability.

- Environment: the immediate surroundings of a molecular cloud can impact it in several ways, e.g., via the ambient gas pressure, shear forces and background cosmic ray and ionizing photon fluxes.

The interplay of these effects is modelled in increasingly complex simulations of the ISM (e.g. Walch et al., 2015). The collapse process of an individual cloud is significantly influenced by its macroscopic properties, such as mass, size and density. However, even clouds randomly generated to have the same macroscopic properties and merely differing by the seed of the random number generator show large variations in star formation rates and efficiencies (Geen et al., 2018). While there has been progress in finding predictive, macroscopic models of star formation (Krumholz & McKee, 2005, Padoan & Nordlund, 2011, Hennebelle & Chabrier, 2011, Federrath & Klessen, 2012), these models do not account for the full complexity of the star formation process yet.

The present-day initial mass function

Collapsing molecular clouds fragment into smaller and smaller clumps, referred to as cores. As these cores collapse, they form protostellar disks, inside of which a central accreting protostar is embedded. The protostar collapses, accretes gas and radiates away energy until its centre becomes hot enough for the ignition of nuclear fusion. At this point, the star enters its main-sequence life. A key question in the field of star formation is what masses such newly formed stars have and how this depends on the conditions of their formation. These masses are quantified as the initial mass function (IMF), i.e., the distribution function of the masses of stars at the beginning of their main-sequence lives. While star formation is not yet fully understood, observationally it is known that stars within the Milky Way form with a surprisingly universal IMF (Salpeter, 1955, Kroupa, 2001, Chabrier, 2003). While the details of these IMFs slightly vary between studies, two major features of the present-day IMF are considered well established:

- At large masses ($M \gtrsim 1\,\mathrm{M}_\odot$) the IMF follows a power-law relation of

$$\frac{\mathrm{d}N}{\mathrm{d}M} \propto M^{-\alpha} \tag{1.7}$$

with an exponent of $\alpha \approx 2.3$. This was the key finding of the Salpeter (1955) study and it implies that the initial mass function is bottom heavy. Not only are most stars low mass stars, but also most stellar mass is found towards the low mass end of the IMF.

- There is a turnover of the IMF at low masses. It can easily be seen that the Salpeter (1955) IMF can not be continued to infinitely small masses, as otherwise the integral of the IMF would not converge, i.e., for any star of a certain mass, there would need to be an infinite mass of smaller stars. Indeed it is found that the IMF turns over towards lower masses. Scalo (1998) and Kroupa (2001) realises this by broken power-laws whereas Larson (1998) and Chabrier (2003) introduce more complex but smooth functions.

1.4.7 Simulating the primordial initial mass function

We have seen above, the present-day IMF is observationally well constrained and there is agreement on its main properties. For Pop III stars, the situation is more complicated. As there are to date no observations of metal-free stars, observationally, their IMF remains mostly unconstrained.

The key reason why the IMF of the first stars is thought to be different from the IMF of present-day populations lies in the inefficient cooling in pristine gas. As mentioned above, pristine star-forming clouds are expected to be much warmer than their present-day counterparts. While present-day molecular clouds have typical temperatures of $T \approx 10 - 20\,\mathrm{K}$, the birth-clouds of the first stars can not cool to temperatures below $T \approx 200\,\mathrm{K}$ (e.g. Abel et al., 2000, Bromm et al., 2002). The Jeans-criterion (Jeans, 1902) for such a cloud implies that only clumps more massive than $\sim 1000\,\mathrm{M}_\odot$ can become gravitationally unstable. In early studies, this was thought to result in Pop III stars that are very massive (a few hundred to a thousand solar masses, e.g. Bromm et al., 1999).

Using advances in computational technology and methods, later studies indicate that the massive protostellar accretion discs of primordial stars are themselves unstable and fragment into smaller clumps (Clark et al., 2011b, Greif et al., 2011a), enabling the formation of low-mass metal-free stars as shown in Fig. 1.3. This

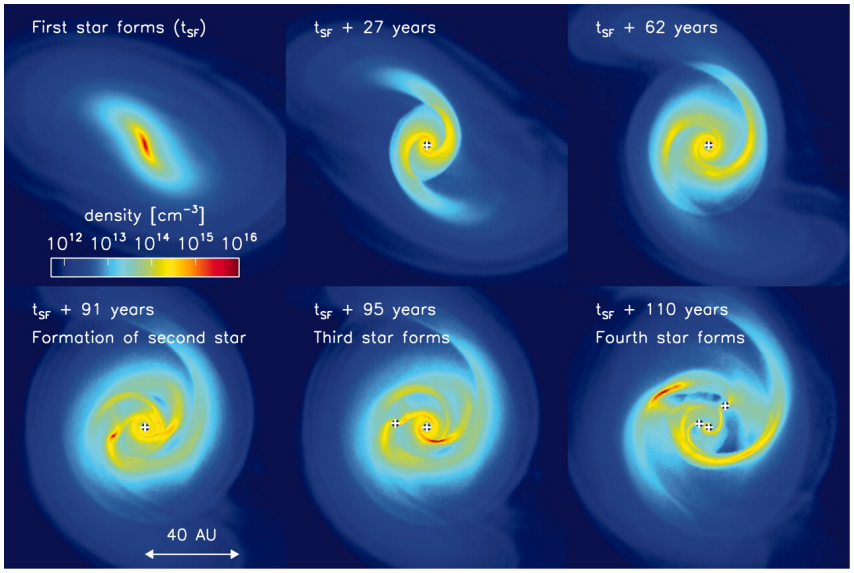

Figure 1.3: Gas density around newly formed Pop III protostars. This image illustrates that protostellar discs of Pop III stars are unstable and fragment. Contradicting the findings of earlier models, this process enables the formation of low-mass Pop III stars. The figure is from Clark et al. (2011b).

insight turns the problem of the pristine IMF into a question of whether and how frequently these clumps become individual stars, merge or get ejected from their formation sites. There have been numerous attempts to simulate these processes (Stacy et al., 2010, 2012, Stacy & Bromm, 2014, Stacy et al., 2016, Clark et al., 2011a, Greif et al., 2012, Hosokawa et al., 2011, 2016, Hirano et al., 2014, Hirano & Bromm, 2017, Hirano et al., 2018, Susa et al., 2014, Susa, 2019, Riaz et al., 2018, Sharda et al., 2021, Latif et al., 2021), yet the results still diverge. This divergence is likely caused by variations in the set-ups used, numerical methods employed and the approximations made in the various simulations.

Detailed simulations of these star-forming regions are inherently difficult and computationally expensive. This is caused by the large variety of physical processes that need to be considered and by the multi-scale nature of the problem, both in terms of spatial- and in terms of time-scales. The reasons for the large required dynamic range are the Truelove criterion (Truelove et al., 1997) and the Courant-Friedrichs-Levi (CFL) criterion (Courant et al., 1928). The former implies that to avoid artificial numerical fragmentation the Jeans length must always be resolved with several resolution elements. As the Jeans mass decreases with increasing temperature, simulations of collapsing gas clouds require super-Lagrangian refinement,

i.e., the densest regions require more and more resolution elements such that the mass enclosed within each resolution element decreases with increasing density. At the same time the CFL criterion demands that, in order to have numerical stability, for a resolution element of size L, the time-step must be smaller than the minimum of the crossing time (L/v) and the sound-crossing time (L/c_s). Thus, when simulating collapse, we need to simulate more and more resolution elements at smaller and smaller time-steps, until either the collapse stops or the simulation stalls. Greif et al. (2012) modelled the formation of several Pop III protostars in their cosmological context with still unmatched resolution. However, the price for this high resolution is that they were only able to simulate $\sim$10 years after the formation of the first protostar.

There are several different numerical techniques to reduce the computational cost of such simulations, albeit at the price of introducing systematic effects on the fragmentation behaviour. For example, Clark et al. (2011b), Greif et al. (2011a), Stacy et al. (2016) and Wollenberg et al. (2020) use so-called sink particles, inserted at the highest densities. These are particles of changing mass that accrete ambient gas that is falling onto them. In these simulations, each sink particle represents an individual star. Sink particles are mostly treated as collisionless particles, i.e., they do not have gas pressure and while they remove gas from their ambient medium they are not considered when solving the hydrodynamic equations. As this method turns every collapsing clump into an individual sink particle and by default does not allow different clumps to merge, this method tends to over-estimate the number of fragments. Some works (e.g. Stacy et al., 2016) implement mergers of colliding sink particles to address this problem. An alternative to this method is the stiff equation-of-state approach (Springel et al., 2005a), in which above a certain density threshold the gas pressure increases rapidly, suppressing fragmentation at the smallest scales. This approach is used e.g. by Hirano & Bromm (2017). As it leads to more extended, puffier clumps, this method naturally predicts fewer clumps and larger likelihoods that clumps merge.

In addition to variations in the resolution and the treatment of the fragmentation behaviour, the simulations also differ in the range of physical processes considered. As a bare minimum, such simulations need to solve the hydrodynamic equations and self-gravity as well as some approximation for cooling processes. These basics are often complemented with detailed modelling of the non-equilibrium chemistry of metal-free gas and the associated cooling and heating processes (Clark et al., 2011b, Wollenberg et al., 2020). Also relevant are radiative feedback (Hosokawa

et al., 2011, Stacy et al., 2012, Hirano & Bromm, 2017) and magnetic fields (Turk et al., 2012, Sharda et al., 2021).

A further factor that plays into the differences among the simulations are the methods for solving the hydrodynamical equations and specifically the geometry of the problem: to reduce the computational cost, some of the simulations (Hosokawa et al., 2011) assume cylindrical symmetry and solve the star formation in 2D. Others model the problem in 3D but use a spherical grid around the first forming protostar (Hosokawa et al., 2016, Hirano et al., 2018). Such a spherical grid puts the central protostar into a privileged position and resolves its immediate vicinity better than the vicinity of potential secondary clumps or protostars. It should also be noted that, in analogy to Noether's theorem (Noether, 1918), there is a relation between symmetries in the employed numerical methods and their ability to accurately reproduce physical conservation laws (Dorodnitsyn, 2001). What this means in practice is that, since the grid is spherically symmetric, matter that is orbiting a star in the centre of the grid preserves its angular momentum better than matter that orbits an off-centre star.

The predictions for Pop III stellar masses made in the last decade range from predicting stellar masses more than $\sim 250\,\mathrm{M}_\odot$ (Hosokawa et al., 2016) to predicting mostly stars in the subsolar regime (e.g. Stacy et al., 2016). Given the intricacies mentioned above, it is likely that these discrepancies will not be conclusively resolved in the near future and further advances in computational capabilities and numerical methods will be needed before we can grow confident in the predicted IMFs.

1.4.8 Kinetic and radiative feedback

After the first stars form they start affecting their environment with a variety of physical processes which are called stellar feedback. In the present-day, stellar winds significantly contribute to feedback (Rahner et al., 2017). However, as Pop III stars have no or comparatively weak winds (Tanaka et al., 2017), we can neglect this kind of feedback here.

The first feedback mechanism that takes action is radiative feedback, which I summarize following Draine (2011). LW radiation destroys the molecular hydrogen. Ionizing radiation heats and ionizes the surrounding gas. The ionizing radiation has a much larger absorption cross-section, and therefore the mean-free path of ionizing radiation in neutral gas is – for our purposes – negligibly small. A star located in initially uniform neutral pure atomic hydrogen gas quickly ionizes a region, called

the Strömgren sphere (Strömgren, 1939). The radius of this region is computed by equating the total hydrogen recombination rate within the sphere with the ionizing photon emission rate. This defines the Strömgren radius

$$R_{\rm str} = \left(\frac{3\dot{N}_{\rm ion}}{4\pi n^2 \alpha_B} \right)^{1/3}, \tag{1.8}$$

where $\dot{N}_{\rm ion}$ is the ionizing photon emission rate, n is the nucleon number density of the gas and α_B is the case B recombination rate coefficient. If the ionized region is significantly smaller than the Strömgren radius, the ionization front expands as a so-called R-type ionization front. Characteristic for this process is that there is no hydrodynamic response, i.e., the ionization front is marked by a change in chemical composition and gas temperature, but not by a change in gas density. As the ionization front approaches the Strömgren radius it slows down. When its expansion velocity becomes comparable to the speed of sound in the ionized medium, the overpressured ionized gas expands and forms a D-type ionization front, which is characterised by a hydrodynamic shock preceding the ionization front.

The speed of sound in metal-free ionized gas is typically on the order of $\mathrm{c}_s = 18\,\mathrm{km\,s^{-1}}$ (see e.g., Abel et al., 2007). As this speed is larger than the escape velocity in minihaloes, the radiative feedback in these haloes is very efficient, and massive stars can easily drive outflows and photoevaporate their host haloes (Whalen et al., 2008). This radiative pre-processing of the gas is of key importance for the subsequent SN feedback (Chiaki et al., 2018).

SNe eject a vast amount of energy into their environments. The evolution of an isolated energetic explosion in a uniform ambient medium was independently derived by Sedov (1959), von Neumann (1947), and Taylor (1950) in the context of nuclear weapons. The SN remnants go through the following phases (see e.g. Draine, 2011):

Free expansion: initially the star ejects $M_{\rm ej}$ of matter with an energy E. In this phase, there is only a negligible interaction with the ambient medium, and therefore the remnant expands with constant velocity.

Sedov-Taylor phase: when the expanding SN remnant has swept up a significant amount of mass relative to the mass of the ejecta it slows down. As the expansion is supersonic the inner parts of the SN remnant will crash into the slowing shell and form a reverse shock, which converts the kinetic energy into

thermal energy. The Sedov-Taylor phase is the time in which this energy is conserved. The expansion is self-similar and only depends on the time t_3 since the explosion (in units of kyr), the energy of the explosion E_{51} (in units of foe[2]) and the ambient nucleon number density n (in units of cm^{-3}). The size of the remnant is

$$R_{\mathrm{SD}} = 5\,\mathrm{pc} E_{51}^{1/5} n^{-1/5} t_3^{2/5}. \tag{1.9}$$

The self-similarity of this solution is a great advantage for numerical simulations of SNe: if the appropriate amount of thermal energy is injected into a sufficiently small region, the long-term behaviour will automatically converge towards the correct solution (e.g. Gatto et al., 2015). For most applications, there is no need to model the SNe ab initio or to include the free expansion phase.

The Sedov-Taylor phase ends once radiative energy losses in the high-density shock become significant. The time at which this occurs for solar metallicity gas is

$$t_{\mathrm{rad}} = 49.3\,\mathrm{kyr}\, E_{51}^{0.22} n^{-0.55}, \tag{1.10}$$

and about twice as long for metal-free gas (see Section 4.4)

Pressure driven snowplough: The radiative loss of energy is only effective in the dense shock-front, not in the diffuse interior of the SN remnant. Therefore, the interior of the SN remnant is still over-pressured. This pressure leads to the expansion as a pressure-driven snowplough:

$$R = R_{\mathrm{SD}}(t_{\mathrm{rad}}) \left(\frac{t}{t_{\mathrm{rad}}}\right)^{2/7}. \tag{1.11}$$

Thus the expansion slows down.

Fade-away: When the speed of the shock-front reaches the speed of sound in the ambient material there can no longer be a shock-wave at the edge of the SN remnant. This occurs at

$$R_{\mathrm{fade}} \approx 2.07 \times 10^{20}\,\mathrm{cm}\; E_{51}^{0.32} n^{-0.37} \left(\frac{c_{\mathrm{s}}}{10\,\mathrm{km\,s^{-1}}}\right)^{-2/5}, \tag{1.12}$$

where c_{s} is the ambient medium speed of sound. At this point, the expansion stalls, the shock turns into a soundwave and disperses.

[2] 1 foe is 10^{51} erg; the abbreviation stands for (ten to the) Fifty-One Erg

1.4.9 Critical metallicity

When the first SN explode they enrich their surroundings with metals and the ability of the gas to cool increases. This increased cooling will eventually lead to a transition in the mode of star formation, i.e., the mass distribution of stars arising from the cooling-induced fragmentation of molecular clouds into distinct cores rather than from the fragmentation of the protostellar accretion disc. This change is thought to lead to the transition to the present-day IMF. At which metallicity this occurs is still under debate. Early studies found a relatively large critical metallicity of $Z_{\rm crit} = 5 \times 10^{-4}\,Z_\odot$ (Bromm et al., 2001). However, this is contradicted by the discovery of stars below this metallicity (Caffau et al., 2012, Keller et al., 2014, Nordlander et al., 2019). More recent studies focus on the role of dust and find that fragmentation can occur at metallicities as low as $Z = 10^{-6}\,Z_\odot$ (Clark et al., 2008, Dopcke et al., 2011, 2013, Schneider et al., 2012, Smith et al., 2015). This research indicates that the fragmentation behaviour depends not only on the dust abundance but also on its composition and grain-size distribution (Chiaki et al., 2017).

1.5 Observational methods of constraining the pristine initial mass function

In the absence of dependable predictions of the pristine IMF, I will now turn to the limited observational constraints. As stellar archaeology is the most common method, I discuss it separately in Section 1.6 and discuss the remaining methods in this section.

1.5.1 Direct detections at high redshifts

There are thus far no direct detections of Pop III stars. There have been reported candidates for Pop III galaxies at high redshift (Sobral et al., 2015, the so-called CR-7 object), but there are no theoretical models that allow for such a massive and bright Pop III galaxy (Hartwig et al., 2016b, Xu et al., 2016b, Visbal et al., 2017). Later observations found different spectral energy distributions and metal lines (Bowler et al., 2017), indicating that CR-7 is indeed not a Pop III galaxy. Generally, to our best knowledge of Pop III stars no telescopes that are available currently or in the near future will be able to detect Pop III stars at their high-redshift formation sites (Jeon & Bromm, 2019, Schauer et al., 2020).

1.5.2 Pristine survivors

Direct detection of Pop III stars could also be made if long-lived low mass Pop III stars exist, survive until the present-day and can be found within the Milky Way (or its close proximity). Such stars have also not been detected yet. It was proposed that some of the most metal-poor known stars are Pop III stars that have been polluted with metals from the ISM (Komiya et al., 2015, Johnson, 2015, Shen et al., 2017). However, it is notable that the typical abundance patterns of these stars do not reflect the chemical abundance of the ISM they would have been accreting from. Additionally, Tanaka et al. (2017) find that the accretion might be inhibited by magnetically driven stellar winds and Suzuki (2018) find that the hot coronae of these stars may block such accretion entirely.

While finding a pristine surviving star would be an exciting prospect, not finding such stars enables us to constrain the nature of Pop III stars too. As we uncover the chemical composition of more and more stars, we can place tighter and tighter limits on how many long-lived metal-free stars can be in the Milky Way. Assuming inefficient pollution, these limits allow us to infer upper limits on the low-mass end of the pristine IMF (Oey, 2003, Tumlinson, 2006, Salvadori et al., 2007, Hartwig et al., 2015, Ishiyama et al., 2016). It should be noted that these studies use widely differing methods to quantify what exactly a non-detection means. Oey (2003), Tumlinson (2006) and Salvadori et al. (2007) use a simple estimate based on the reported number of detections of stars below a certain metallicity threshold. Hartwig et al. (2015) relies on selected large-scale surveys and assume that these surveys essentially observe random stars. Ishiyama et al. (2016) rely on the same surveys but compute expectation values of detection numbers based on limited magnitudes and survey footprint. The constraints are also based on various model assumptions with regards to the formation sites and star formation efficiencies of Pop III stars. Still, these limits are probably the most robust observational constraints of the Pop III IMF. Modifying most model assumptions usually changes the predicted number of Pop III survivors only by a factor of a few, whereas changing, e.g. the Pop III IMF to a present-day IMF yields more survivors by orders of magnitude (Salvadori et al., 2007). However, this method can only be used to constrain a very small range of stellar masses, approximately 0.6–0.8 $M_\odot$. The reason for this narrow mass range is that more massive stars would not survive until today (Marigo et al., 2001), while less massive stars would typically be too faint to obtain the high-resolution spectra required to constrain their chemical abundances (Anna Frebel,

personal communication).

1.5.3 Supernova detections

Direct detections of Pop III SNe would serve as direct evidence for the existence of the progenitor stars. However, thus far there are no such detections. Several issues make such detections challenging.

Firstly, most SNe occur at the end of the life of the short-lived stars and therefore the SNe are at high redshift, which causes them to be very faint. As the Universe is largely neutral these redshifts the Gunn-Peterson trough (Gunn & Peterson, 1965), i.e., the combination of Lyman-α absorption and the continuous redshifting of the spectrum removes a considerable fraction of the luminosity. This effect makes it increasingly difficult to observe SNe at redshifts above $z = 6$ (Rydberg et al., 2020), especially with ground-based telescopes.

Secondly, it may be non-trivial to confirm tentative detections and to verify their Pop III nature. Whalen et al. (2013b) find that CCSNe of metal-free and metal-enriched stars may be hard to distinguish. They suggest identifying a Pop III CCSN by observing it at sufficiently large redshifts to exclude a metal-enriched SN. Whether and up to what metallicity PISNe occur is still an open question (Eggenberger et al., 2021). Meanwhile, there have been detections of so-called superluminous SNe which have been argued to be PISNe, but this is still an open question (Gilmer et al., 2017). Only detections will show how clearly a Pop III PISNe can be identified as such.

Thirdly, Pop III SNe are rare. While the James Webb Space Telescope (JWST) will be able to detect PISNe to very high redshifts (Whalen et al., 2013a) the SNe are exceedingly rare (Magg et al., 2016). This makes it unlikely that JWST will find these SNe (Hummel et al., 2012, Hartwig et al., 2018a). Therefore, instruments with a larger field of view such as the Nancy Grace Roman Space Telescope[3] (formerly wide-field infrared survey telescope (WFIRST)) may be better suited for such detections.

1.5.4 The hydrogen 21-cm signal

A key method for observing the high-redshift Universe lies in the absorption and emission of the 21 cm line, i.e., the spin-flip hyperfine transition of neutral hydrogen in its ground-state. I will follow the descriptions in Pritchard & Loeb (2012) for the

[3] `https://roman.gsfc.nasa.gov/`

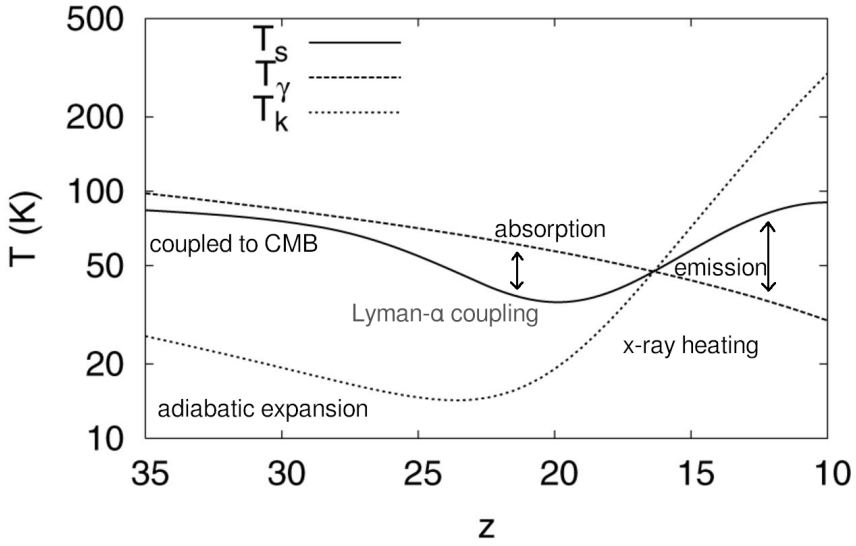

Figure 1.4: Spin (solid line), gas (dotted line) and CMB temperature as function of redshift, from Hirata (2006, annotations added). The coupling of the spin temperature to the kinetic gas temperature causes it to first fall below the CMB temperature. When the IGM is heated above by X-rays the spin temperature rises accordingly. This causes first absorption and then emission in the 21 cm line.

general physical processes and the specific high-redshift application. To understand whether we can see this line in emission or absorption it is useful to define the excitation temperature $T_{\rm ex}$. In local thermal equilibrium (LTE) the fraction of atoms in the excited state is determined by the energy separation ΔE of the two levels and the temperature T, and it follows the Boltzmann distribution,

$$\frac{n_{\rm u}}{n_{\rm l}} = \frac{g_{\rm u}}{g_{\rm l}} \exp\left(-\frac{\Delta E}{k_{\rm B} T}\right), \tag{1.13}$$

where $n_{\rm u}$ is the number of atoms in the upper, $n_{\rm l}$ is the number of atoms in the lower state, $g_{\rm u}$ and $g_{\rm l}$ are the respective statistical weights and $k_{\rm B}$ is the Boltzmann constant. If the atoms are not in LTE we can define the excitation temperature as the temperature equivalent to the occupation fraction, i.e.,

$$T_{\rm ex} = \frac{E}{kb} \frac{1}{\ln\left(\frac{g_{\rm u} n_{\rm l}}{g_{\rm l} n_{\rm u}}\right)}. \tag{1.14}$$

This definition allows us to reconstruct whether radiation from the CMB is absorbed or emitted in the 21 cm band by comparing the spin temperature, i.e., the excitation temperature of the 21 cm transition, to the CMB temperature at the respective

redshift. Before recombination, gas and radiation are fully coupled. Therefore their temperatures are the same. After recombination, the radiation temperature of the CMB evolves as $T_{\rm CMB} \propto (z+1)^{-1}$. Until $z \sim 200$ Compton scattering is of CMB photons is very common, thus the gas temperature and the CMB temperature are approximately equal. At later times, in absence of heating and cooling processes, the gas expands adiabatically, i.e., its temperature evolves as $(1+z)^{-2}$. The spin temperature evolves as follows:

- At very high redshifts ($z \gtrsim 200$) the atoms of the gas collide frequently and therefore the spin temperature is equal to the gas temperature.
- At $z \lesssim 100$ collisions with CMB photons are more common than collisions with other gas atoms, which drives the spin temperature towards the CMB temperature, and therefore there is no net emission or absorption.
- When the first stars form, scattering of Lyman-α photons in the IGM re-couple the spin temperature to the IGM gas temperature via the Wouthuysen-Field-effect (Wouthuysen, 1952, Field, 1958). As the gas temperature is lower than the CMB temperature at this time, the 21 cm transition absorbs CMB photons.
- X-ray emission from astrophysical sources (e.g., X-ray binaries) start heating the IGM above the CMB temperature and the 21 cm line goes into emission.
- Due to reionization, there is less and less neutral hydrogen in the IGM and thus the line gradually vanishes.

In total, these effects are expected to lead to a dip in the 21 cm intensity at around $z \sim 20$, caused by the large-scale onset of star formation. Bowman et al. (2018) reported the observation of such a signal. However, this detection is still controversial and has not yet been confirmed by other experiments. One of the controversies around this detection revolves around the depth of the signal: the absorption trough is deeper than the expectation, in the limiting case of the spin temperature being equal to the gas temperature. If this feature is confirmed, there must be either an additional source of gas cooling (Barkana, 2018a) or additional radio background sources (Reis et al., 2020b). The redshift at which this dip occurs also has implications for the formation sites, the IMF and star formation efficiency of the first stars (Schauer et al., 2019b). Future observations of the 21 cm power-spectrum by the square kilometre array (SKA)[4] will provide more detailed insights into this epoch

[4] `https://www.skatelescope.org`

and allow much better constraints on the processes that govern it.

1.5.5 Reionization

As the first stars start the process of reionization, we can potentially learn something about them from observations of the Thompson scattering optical depth τ_e. This parameter is an integrated measurement of the free electron density across cosmic time and is obtained from the polarization of the CMB. Initial measurements ($\tau_e = 0.17 \pm 0.04$, Spergel et al., 2003) caused assumptions of large Pop III star formation efficiencies and ionizing radiation outputs. Later, measurements by the *Planck* satellite found a much lower value of $\tau_e = 0.058 \pm 0.012$ (Planck Collaboration et al., 2016b). This favours much later reionization and therefore a much smaller contribution from Pop III stars (Visbal et al., 2015). This type of analysis is very sensitive to the speed of reionization, ionizing photon escape fraction and the contributions of metal-enriched stars. Thus, the reionization history can be used to constrain Pop III formation, albeit for now only to derive upper limits on their effective ionizing photon output.

1.5.6 Gravitational waves

The first detection of a merger of two black holes with the Laser Interferometer Gravitational-Wave Observatory (LIGO) experiment (Abbott et al., 2016), opened the door to gravitational wave astronomy. It is not directly possible to infer the composition of the progenitor star of these black holes. However, if the first stars are indeed significantly more massive than Pop II stars, there might be an imprint in the occurrence rates of mergers as a function of masses and redshifts. A key feature of the mass-distribution of merging black holes is a mass gap in the range $60\,\mathrm{M}_\odot \lesssim M \lesssim 200\,\mathrm{M}_\odot$, predicted because PISNe do not leave compact remnants behind. Of particular interest in this context are mergers by black holes above the PISN mass gap (Hartwig et al., 2016a), which can be identified with the most metal-poor populations. While there are thus far no detections of mergers of black holes above this mass-gap, there is one detection of a merger within it (Abbott et al., 2020). Woosley & Heger (2021) point out that several poorly understood factors influence where the mass-gap starts (magnetic fields, hyper-Eddington accretion, nuclear reaction rates) and that the detected merger is not necessarily within the mass-gap. All in all, as the number of detections grows, gravitational wave astronomy promises new insights into the first stars.

1.6 Stellar archaeology

Stellar archaeology refers to the study of the early Universe by investigating old, long-lived stars. These stars are ancient relics of a time long past. Their properties, especially the chemical abundances inferred from absorption lines in their spectra, can give insights into the time and environment of their formation. In this context, it is especially interesting not to look at the oldest stars but at the metal-poor stars. Stars forming in chemically evolved systems at high redshifts are unlikely to contain a lot of information about the first stars. However, small, chemically primitive systems, even at somewhat lower redshift have more in common with the first building blocks of galaxies and may still form Pop III stars well within the era of reionization (Xu et al., 2016b, Jaacks et al., 2018). Additionally, determining the age of stars precisely is extremely difficult, even with astroseismological observations. Valentini et al. (2019) find that the relative error of the ages of their old metal-poor stars is around 35 per cent. If we hoped to determine whether a star formed at the beginning ($z \approx 20$) or the end ($z \approx 6$) of the epoch of reionization, we would need to determine its age with a precision of $\Delta t \approx 500\,\mathrm{Myr}$, i.e., a relative error of merely 4 per cent. Therefore, it is common practice to understand the gradual build-up of heavy elements in the Universe as a measure of time (see e.g. Frebel & Norris, 2015). It is assumed that the most metal-poor stars are the oldest stars, which usefully coincides with our interest in chemically primitive systems rather than the oldest stars.

1.6.1 Where are the oldest stars?

Determining the chemical abundances of long-lived stars is usually only feasible for stars within the Milky Way and its satellite galaxies. The main components of the Milky Way are the thin disk, the thick disk, the bulge and the (stellar) halo. The oldest stars are generally believed to be in the bulge and the halo (e.g., Starkenburg et al., 2017a). Stars with metallicities[5] [Fe/H] $= -3$ are called extremely metal-poor (EMP) stars and are considered to be valuable targets for stellar archaeology. There are thus far several hundreds of known EMP stars (Suda et al., 2008) and the vast majority of them are in the stellar halo of the Milky Way. Efforts to investigate

[5] For denoting abundances of element X relative to element Y, we use the standard notation $[\mathrm{X/Y}] = \log_{10}(m_\mathrm{X}/m_\mathrm{Y}) - \log_{10}(m_{\mathrm{X},\odot}/m_{\mathrm{Y},\odot})$
where m_X and m_Y are the mass abundances of these elements, and $m_{\mathrm{X},\odot}$ and $m_{\mathrm{Y},\odot}$ are the respective solar abundances. [Fe/H] is referred to as metallicity.

the metal-poor stellar population in the bulge prove difficult due to the large stellar density and due to dust absorption (Arentsen et al., 2020).

1.6.2 Properties of the most metal-poor stars

During the last ∼30 years, there have been many observational programs targeted at discovering and investigating the most metal-poor stars (McWilliam et al., 1995, Christlieb et al., 2008, Starkenburg et al., 2017b, François et al., 2018). A review of these stars and their properties can be found in Frebel & Norris (2015), which I will here follow for the main observational results and interpretations. As the number of observations of stars in the EMP regime grew, it became increasingly clear that many of them are substantially carbon enhanced (Yoon et al., 2016), i.e., they have a significantly super-solar carbon to iron ratio ([C/Fe] > 1.0). These stars are referred to as carbon enhanced metal-poor (CEMP) stars. There are several sub-classes of CEMP stars:

CEMP-no stars have no detectable enhancement in neutron-capture elements. These stars are commonly thought to be genuine second-generation stars.

CEMP-s stars are s-process enhanced. As we discussed before, s-process elements are synthesized by stars in the asymptotic giant branch. These stars are therefore thought to be enriched via binary mass transfer from companion stars (Lucatello et al., 2005). Thus, their photospheric abundances are not representative of the chemical composition in their formation environments, which limits their usefulness for stellar archaeology.

CEMP-r stars are enriched in r-process elements and are mostly found at metallicities of [Fe/H] $\gtrsim -3$ (Frebel & Norris, 2015). The presence of r-process elements and the relatively high metallicities at which they are found indicates a more complex combination of contributing nucleosynthetic sources compared to CEMP-no stars.

CEMP-r/s stars are enhanced both in r- and in s-process elements. Similar to CEMP-r stars, these are usually found at relatively high metallicities.

The most iron-poor known stars are typically CEMP-no stars (Keller et al., 2014, Nordlander et al., 2019, Frebel et al., 2019). For our purposes, this is the most interesting sub-class of CEMP stars. Yoon et al. (2016) further group CEMP-no stars into two groups, depending on their position in the [Fe/H]-[C/Fe]-plane.

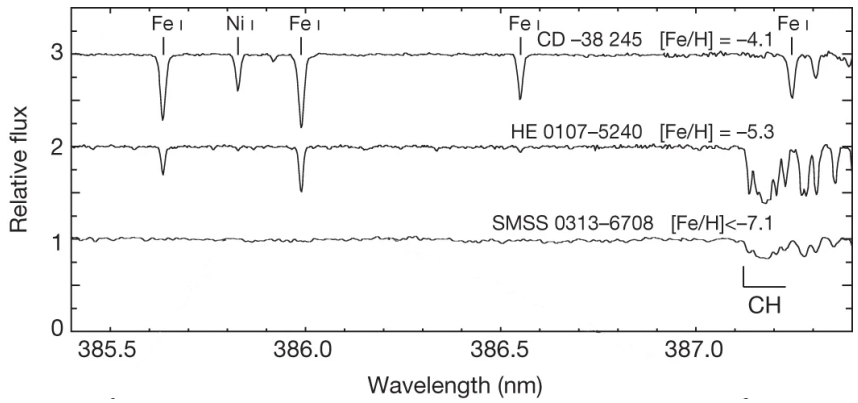

Figure 1.5: Part of the normalized spectrum of the so-called Keller star, SMSS 0313-6708, from (Keller et al., 2014), compared to other extremely metal-poor stars. Strikingly, while the star exhibits visible absorption by CH-bands, there are no significant detections of iron lines. This feature indicates that the star has an extremely large carbon-to-iron ratio.

However, other classifications based on additional abundances have been proposed (Hartwig et al., 2018b, Hansen et al., 2019). The most iron-poor star known to date is SMSS 0313-6708 (Keller et al., 2014, see Fig. 1.5). Despite substantial effort, iron has not been detected in this star ([Fe/H] < -7.1), which implies a [C/Fe]>4.5, i.e., at least 30000 more carbon atoms per iron atom than it is found in the sun. Understanding the source of this carbon enhancement has been one of the major challenges of nucleosynthetic models in the last decade. Caffau et al. (2011) report the most metal-poor star known to date, with a metallicity of $Z < 4.5 \times 10^{-5}\,\mathrm{Z}_\odot$ and no discernible carbon enhancement.

A key feature of the known CEMP-no stars is their uniqueness. The chemical abundances of metal-rich stars are characterised by only a few quantities (such as the metallicity and the [α/Fe] ratio). The most metal-poor stars on the other hand all have individual and unique abundance patterns. This is seen as an indication that only one or very few SNe contributed to the enrichment of these stars.

1.6.3 The satellites

The satellite galaxies of the Milky Way offer additional insights into early star formation. A summary of the known satellites of the Milky Way can be found in McConnachie (2012). These galaxies have stellar masses as low as $1000\,\mathrm{M}_\odot$ and are often extremely dark matter dominated. In particular, these low-mass, faint and low-metallicity systems are very useful here, as they formed stars only for a short time and have a more monolithic evolution. In contrast to the Milky Way, there

can only be a small number of distinct star-forming progenitor systems and thus it is easier to assess whether individual stars have a common origin and to investigate the conditions under which the stars in these systems formed (Revaz & Jablonka, 2012).

The chemical abundances of stars in various of these satellites have received special attention (Frebel & Norris, 2015). Skúladóttir et al. (2019) show the elemental abundances observed in Sculptor can be used as chemical clocks, which allows investigating how quickly various enrichment processes occur (see also Jablonka et al., 2015). Among the most notable satellites is Reticulum II, which shows several highly r-process enhanced stars (Ji et al., 2016a,b). This result together with the observation that most satellites do not show r-process enhancement can be used to confirm that the r-process enrichment must be a rare and prolific event (Brauer et al., 2019). Observations from the Magellanic Cloud satellites Carina II and III shows signatures of inhomogeneous enrichment in neutron-capture elements (Ji et al., 2020). Chiti et al. (2021) find evidence for a stellar halo in the extremely small Tucana II dwarf galaxy. These findings highlight that analysing and understanding dwarf galaxies offers a wealth of insights and is fundamental to stellar archaeology.

1.6.4 Abundance fitting

To be able to understand the abundance patterns in metal-poor stars, they are commonly compared to theoretical models of SN yields of Pop III stars. A key challenge in this area has been the relatively large carbon abundances. Umeda & Nomoto (2003) proposed that, if a large fraction of the heavy elements fall back onto the compact remnant while the lighter elements escape, the large carbon to iron ratios can be obtained. Such SNe are commonly referred to as faint[6] SNe. One scenario for such faint SNe are jet SNe, in which all the energy is deposited along one axis and thus much of the remaining material can collapse onto the compact remnant (Tominaga et al., 2007).

To obtain quantitative information on the possible progenitors of a certain star, typically, the abundance pattern is compared against a library of SNe yields. Examples of such libraries can be found in Heger & Woosley (2010), Limongi & Chieffi (2012), Ishigaki et al. (2018), Grimmett et al. (2018). Observed abundances are compared to these libraries both for individual stars (e.g. Keller et al., 2014, Ishi-

[6]Notably, while these SNe are sometimes associated with low explosion energies, their faintness arises from the radioactive ^{56}Ni falling back onto the remnant, not from the low kinetic or thermal energy of the ejected material.

gaki et al., 2014, Nordlander et al., 2017, Ezzeddine et al., 2019, Ji et al., 2020) and for large samples (Ishigaki et al., 2018, Fraser et al., 2017). These studies indicate that the most metal-poor stars are primarily enriched by intermediate-mass (several tens of solar masses), faint CCSNe. This result is expected, as such models perform best in producing the large carbon-to-iron ratios seen in these stars.

Despite large variations in the observed abundance patterns, EMP stars do not seem to exhibit the characteristic abundance patterns of PISNe. This is a somewhat surprising result, as PISNe have been a stable prediction of models of early star formation and stellar evolution. There are two prevailing hypotheses that could reconcile this lack of evidence with the existence of PISNe. Firstly, based on a semi-analytical model, Karlsson et al. (2008) argue that since PISNe yield very large amounts of metals, the descendants of PISNe should be relatively metal-rich. Therefore, the surveys aimed at finding and analysing metal-poor stars would not be able to find them. Additionally, since more metal-rich stars are much more common (see e.g. Bonifacio et al., 2021), this also implies that the chances of finding such a star by pure luck are greatly diminished. Secondly, Whalen et al. (2008) find in one-dimensional simulations that the combination of the large ionizing radiation output of a massive Pop III star and the extremely energetic PISN can fully destroy the host halo of the SNe. Thus future episodes of star formation may be prevented altogether, and second-generation stars carrying the fingerprint of PISNe may never form. At the current state, it should be emphasized that both of these ideas are merely hypotheses, and the problem of PISNe is far from solved.

While the SN models provide ratios of abundances (such as [C/Fe]) the models do not directly imply the metallicities of the stars. The reason for this is that it is fundamentally uncertain how much the ejecta are diluted with material from the pristine ISM before the second generation of stars forms. Most works that fit abundance patterns simply scale the ejecta to match the metallicity of the fitted abundance patterns. The dilution is kept as a free parameter. Effectively only the ratios of abundances are fitted, not the absolute abundances. In most cases, whether the required dilution is physically possible is not discussed. Notable exceptions to this are e.g. Tominaga et al. (2007) and Ji et al. (2020).

1.7 Outline

In this thesis, I will investigate the observable imprint of the earliest epoch of star formation. I give additional background, on some of the methods used in this thesis

in Chapter 2. In Chapter 3 (published as Magg et al., 2019) I discuss implications of the fact that there are thus far no observations of metal-free stars in the Milky Way. I develop and explore a simple analytical limit for the dilution of SN ejecta with cosmological hydrodynamical simulation in Chapter 4 (published as Magg et al., 2020). The question of the dilution of SN ejecta is further explored in the context of PISNe in Chapter 5 (published as Magg et al., 2021a). In Chapter 6, I explore implications of the duration of the transition for metal-free to metal-enriched star formation for the cosmological 21-cm transition (published as Magg et al., 2021b). Finally, I summarize the findings, conclude and give further outlooks in Chapter 7.

2

Methodological background

In this thesis, I use the semi-analytical model Ancient Stars and Local Observables by Tracing Haloes (A-SLOTH), as well as the hydrodynamical simulation code Arepo (Springel, 2010). A-SLOTH was partially developed in this thesis (Chapter 6) and Arepo was modified for the particular purpose of the simulation presented in Chapter 5. While the details are presented in the respective chapters, here I will give an introduction to the principles underlying both methods.

2.1 A-SLOTH

2.1.1 The need for semi-analytical models

Simulating the high redshift Universe poses very large numerical challenges. Hydrodynamical simulations of this epoch fall short when exploring several key questions. There are two major groups of reasons for this, namely, issues of scale and the reliability of sub-grid models.

The high-redshift Universe is notorious for the multi-scaled nature of its governing processes: to fully resolve the formation of the first stars, resolutions below a solar radius are necessary, while at the same time one needs to include at least several $100\,\mathrm{kpc}\,h^{-1}$ to self-consistently model the formation of their host haloes (Greif et al., 2012)[1]. Resolving the interaction between a Pop III star on its host halo requires at least sub-parsec resolution (see Chapter 5). Accurate modelling of LW radiation requires extremely large spatial and spectral resolution (to resolve the ionization front Schauer et al. (2017b) employ resolutions of $\sim 0.0001\,\mathrm{pc}$). At the same time, the mean free path of LW photons in the high redshift IGM is more than $100\,\mathrm{Mpc}\,h^{-1}$, leading to an almost uniform LW background (Dijkstra et al., 2008). Due to these long mean free paths, the local strength of this background and therefore the local conditions for star formation are determined by the large-scale density fluctuations (Fialkov et al., 2013).

Because of the extremely large range of relevant spatial scales, any particular numerical simulation must focus on only a few selected scales and use approximate models for all processes that happen on larger or smaller scales. These approximations are usually made based on previously published models. This can lead to rather large uncertainties in these sub-grid models and environment parameters. For example, recent numerical experiments on the collapse of the first minihaloes under LW feedback (Schauer et al., 2021, Kulkarni et al., 2021) vary the strength of the LW background by four orders of magnitude since the strength of the background is not well understood. Due to their large cost, it is usually not possible to run sufficiently large suites of simulations to fully explore the impact of the parametrized sub-grid models and environments. Large simulations like the *Renaissance* simulations (Xu et al., 2016b) or the First Billion Years project (Johnson et al., 2013) use only one

[1] The simulations by Greif et al. (2012) span 25 orders of magnitude in size scales. The resolution is so extreme that particle positions can not be reliably distinguished with a triple of 64-bit variables and higher precision coordinates had to be implemented for the simulations to become possible (Thomas Greif, personal communication)

IMF and model for star formation. In this regard, the results have to be taken at face value, since exploring and fully understanding the impact of the choices made in constructing the sub-grid star formation model would be far too costly.

To alleviate the problems many authors rely on semi-analytical models instead (Salvadori et al., 2007, Magg et al., 2016, Graziani et al., 2017, de Bennassuti et al., 2017, Bremer et al., 2018, Côté et al., 2018, Visbal et al., 2018, Behroozi et al., 2019). These models can be described as a sub-grid model without a simulation. They trace macroscopic properties of galaxies (such as their stellar mass, SFR or mean metallicity) without modelling the microscopic details, i.e., without attempting to solve the hydrodynamical equations or modelling the exact 3-dimensional distribution of gas. It should be noted that the line I draw here for this distinction is somewhat arbitrary and some models could reasonably be considered to be either a numerical simulation or a semi-analytical model. For example, Fialkov & Barkana (2014) employ a simulation method that solves radiative transfer equations and creates spatially resolved 21 cm maps while employing a star-formation model that is based on analytical HMFs. The defining advantage of these models is that they are usually computationally very cheap. This allows one to run multiple or even hundreds of models under varying assumptions and to investigate the effect of the parameter choices. This feature is particularly relevant because it is often not possible to directly infer poorly understood quantities from observations. By running semi-analytical models many times, one can generate a broad range of observables and thus infer the conditions that gave rise to the observations by comparison. For this reason, because of the low computational cost and the relative ease with which they can be modified, semi-analytical models have found broad use in studying the high-redshift Universe.

2.1.2 Basic principles

The A-SLOTH code works by walking so-called merger trees. A merger tree is a representation of the evolution of a galaxy on a set of time-steps. For each time-step, the tree contains all haloes that will end up in the halo of the main galaxy later on, as well as the connections to where these haloes are found in the previous and the subsequent time-step (see Fig. 2.1). One entry in the tree, i.e., one halo at a specific time-step, is usually referred to as a node of the tree. A node has at least one progenitor and exactly one descendant node, i.e., it is identified with at least

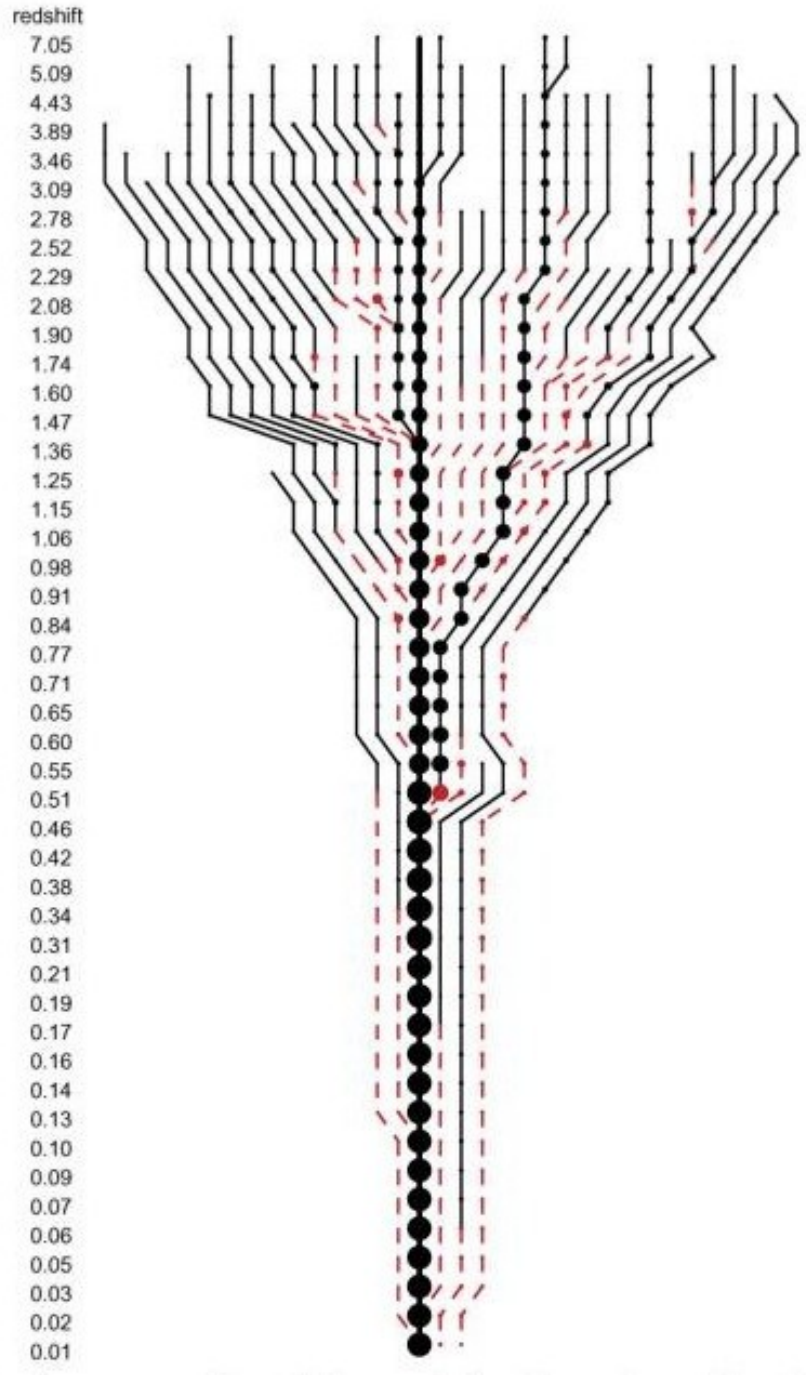

Figure 2.1: A merger tree of a Milky Way-like galaxy from Stewart et al. (2008) and Bullock et al. (2009). The y-direction corresponds to the redshift- or equivalently time-step. The size of the circles shows the mass of the haloes, and the connecting lines show how they are associated over time. Dashed lines indicate sub-haloes and solid lines indicate independent haloes.

one node at the previous time-step and with exactly one node at the next time[2]. If one merger or several mergers occur between the previous and the current time-step the node can have more than one progenitor.

Merger trees can either be generated with a statistical algorithm, the extended Press-Schechter algorithm (Bond et al., 1991, Lacey & Cole, 1993) or they can be extracted from simulations (e.g. as in Griffen et al., 2016). The former approach has the advantage that it is much faster to generate merger trees this way. However, in contrast to simulations, these merger trees lack spatial information and there are no sub-structures within the haloes. Extracting merger trees from simulations requires one to first identify the haloes with a so-called halo finder (Springel et al., 2001, Behroozi et al., 2013a) and then to find the relationships between the haloes at different times (Behroozi et al., 2013b, Smith & Lang, 2018). This is often done for large cosmological N-body dark matter only simulations (Griffen et al., 2016, Ishiyama et al., 2016, 2021).

A-SLOTH processes these merger trees, starting at the highest redshifts and progressing until the present day. The exact physical model has been progressively improved over the years, starting with a very simple model in Hartwig et al. (2015) to far more complex implementations (Magg et al., 2018, Tarumi et al., 2020, Chen et al., 2022). Here I will only outline the basic principle of the model, rather than going into detail on the exact physical model and its implementation.

The model starts at high redshifts when there are thus far no stars in the simulated domain. This makes the initial state of all haloes very simple: they contain no stars and are free of metals. As the model progresses haloes grow in mass until they reach the critical mass for star formation (see Section 1.1.3). At this point, the halos start containing a significant amount of baryonic matter and the first stars start forming. The baryonic matter is divided into four components, namely hot gas, cold gas, stars and outflows. We enforce that the ratio of the total mass of these four components to the virial mass of the halo is equal to the cosmic baryon fraction $\Omega_\mathrm{b}/\Omega_\mathrm{m}$. Initially, the gas is accreted into the hot component. The cooling of the gas leads to this gas slowly transiting into the cold phase, which in turn forms stars. These stars then affect their environment via radiative heating and SNe feedback. The heating reduces the amount of gas that is immediately available for further star formation and transfers it back to the hot component. The

[2]The nodes are, in analogy to family trees, often called child and parent nodes. Several nodes are called siblings if they share the same parent. Note that the *previous*, i.e., the older and thus typically smaller nodes are the children.

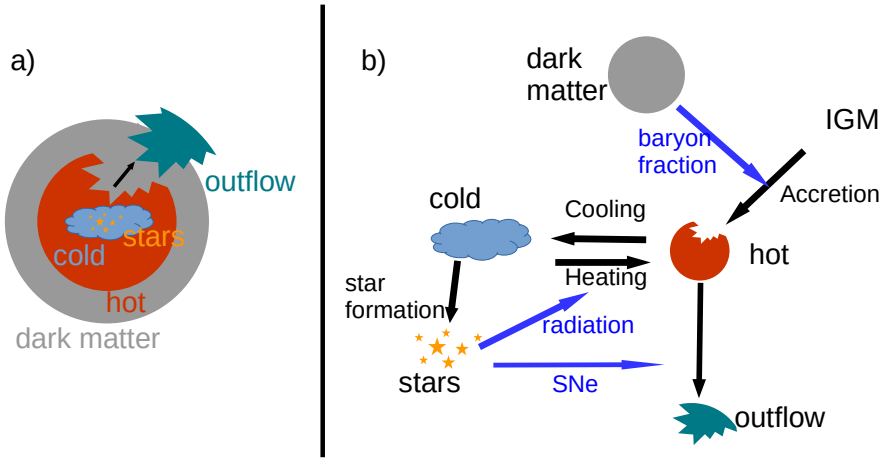

Figure 2.2: Illustration of the different gas phases in A-SLOTH. Panel a) shows how the halo is represented as a four-phase gas model and a dark matter component. Panel b) shows the gas flow between the different components. The blue arrows indicate controlling influence, e.g., the accretion from the IGM is controlled by the size of the dark matter halo via the cosmic baryon fraction. Gas is initially accreted from the IGM into the hot phase and then cools into the phase. Stars form from the cold gas phase and heat part of the remaining cold gas via ionizing radiation.

enrichment by the SNe causes the transition from Pop III to Pop II star formation. These processes are illustrated in Fig. 2.2. Similar effects also occur externally. The ionizing and LW radiation can prevent neighbouring haloes from forming stars while the metals ejected into the IGM can lead to haloes forming Pop II stars right away, without ever having formed metal-free stars. The effects on other haloes are generally referred to as external (i.e., external radiation feedback, external enrichment), as haloes are affected from the outside. These feedback effects underline the importance of having the spatial information to determine how close haloes are to each other, which is why we prefer using merger trees from N-body simulations. A complete mathematical description of the star formation and feedback model can be found in Chen et al. (2022).

This model has found numerous uses over the past years and allows to efficiently connect high-redshift star formation to local and cosmological observations. The applications range from predictions for detection rates of high-redshift SNe (Magg et al., 2016, Hartwig et al., 2018a, Rydberg et al., 2020), to providing a better understanding of the metal-poor and hypothetical metal-free stellar populations in the Milky Way (Hartwig et al., 2015, 2018b, Magg et al., 2018, Tarumi et al., 2020)

2.2 Arepo

2.2.1 Eulerian and Lagrangian hydrodynamics

When modelling hydrodynamical systems one is faced with the choice of a reference frame, in which the hydrodynamical equations are written. While in principle arbitrary frames of reference are possible, there are only two common choices: Eulerian and Lagrangian hydrodynamics, i.e., a fixed and a comoving frame of reference. In the Eulerian (fixed) frame of reference, the hydrodynamical equations take the form of hyperbolic conservations laws, namely

- the conservation of mass

$$\frac{\partial \rho}{\partial t} - \nabla \cdot (\rho \vec{v}) = 0, \tag{2.1}$$

  where ρ is the density and $\vec{v}$ is the velocity of the gas,

- the conservation of momentum

$$\rho \left(\frac{\partial \vec{v}}{\partial t} - (\vec{v} \cdot \nabla)\vec{v} \right) = \rho \vec{F} - \nabla p, \tag{2.2}$$

  where $\vec{F}$ is the external force and p is the pressure, and

- the conservation of energy

$$\frac{\partial \epsilon}{\partial t} + \vec{v} \cdot \nabla \epsilon = -p \nabla \cdot \vec{v} - \nabla \vec{F}_c + \Gamma - \Lambda, \tag{2.3}$$

  where ϵ is the energy density, $\vec{F}_c$ is the conductive heat flow, Γ is the radiative heating rate per unit volume and Λ is the radiative cooling rate per unit volume.

These are the most simplified equations, only valid in an ideal (i.e., inviscid) non-magnetized fluid. By introducing the comoving derivative

$$\frac{\mathrm{D}}{\mathrm{D}t} = \frac{\partial}{\partial t} + (\vec{v} \cdot \nabla), \tag{2.4}$$

we can rewrite the equations into their Lagrangian form, i.e., in a frame moving along with the flow. Then the equations take the form

$$\frac{\mathrm{D}\rho}{\mathrm{D}t} = -\rho \nabla \vec{v}, \tag{2.5}$$

$$\rho \frac{\mathrm{D}\vec{v}}{\mathrm{D}t} = \rho\vec{F} - \nabla p, \tag{2.6}$$

and

$$\frac{\mathrm{D}\epsilon}{\mathrm{D}t} = -p\nabla \cdot \vec{v} - \nabla\vec{F}_c + \Gamma - \Lambda. \tag{2.7}$$

It is worth noting that these differential equations are only valid in the absence of discontinuities, in particular contact discontinuities and shocks. If such discontinuities are present in the fluid, the integral form of the equations needs to be used instead.

While both sets of equations are in principle identical, for any given problem one might be easier to solve than the other. This distinction also translates to hydrodynamical simulation methods: in most cases, numerical solutions are either computed in the comoving or a fixed frame. Examples of Eulerian simulation codes are FLASH (Fryxell et al., 2000) and RAMSES (Teyssier, 2002). Typically these codes use a fixed grid (or mesh) of cells and additionally nested refined grids in the regions of high interest. Gas flows between the cells and the flow rates through any individual cell interface can be computed with a so-called Riemann-solver. The fixed-grid nature of these methods makes it very easy to navigate the grid and find neighbouring cells, which is why they are typically very well parallelizable. Because of this great performance, FLASH has been used for the biggest simulation of turbulence thus far (Federrath et al., 2021). The biggest downside of these codes is the introduction of grid artefacts. For example, in Cartesian grids, this leads to accretion discs aligning with the grid axes (see tests in Hopkins, 2015).

The most common Lagrangian simulation method is smoothed particle hydrodynamics (SPH), as presented for example in GADGET (Springel, 2005). In this approach, the continuous fluid is approximated as an ensemble of "fluffy" particles with a pre-defined shape (or Kernel). The properties of the fluid at any given point can be reconstructed by overlapping all particles in the vicinity. Fluid flows are described by the equations of motion of these particles, which can be derived from an appropriately discretized Lagrangian (Springel & Hernquist, 2002). Because of this underlying nature of the SPH equations of motion, the resulting algorithm is invariant under Galilean transformations and preserves momentum, angular momentum, energy and entropy very well. While this feature makes SPH excellently suited for some astrophysical problems, it is not a desirable property in some situations. Specifically, SPH performs notoriously poorly when modelling shock-fronts, which should generate entropy. This issue is commonly alleviated by allowing en-

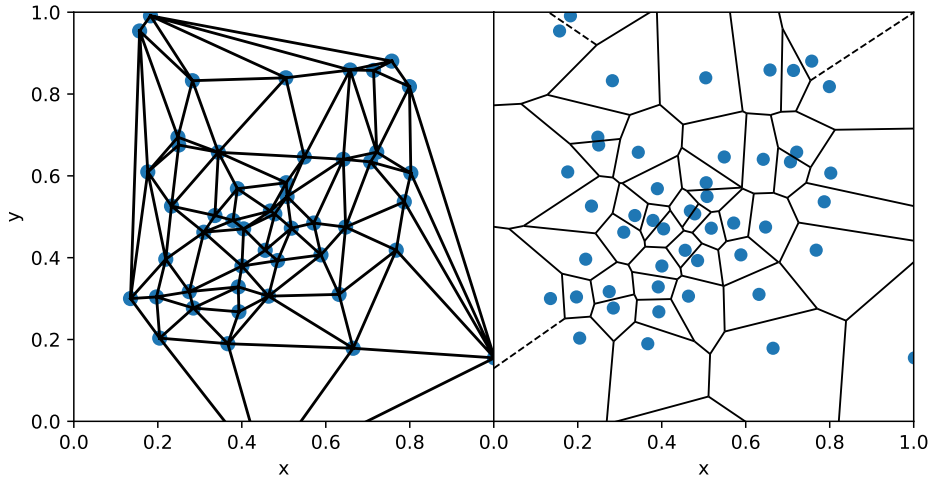

Figure 2.3: Visualization of a Delaunay triangulation (left panel) and a Voronoi tesselation (right panel), here simplified in two dimensions. The Delaunay triangulation is a set of triangles in which each mesh-generating point is connected to its neighbours in such a way that any triangles between the points never intersect each other. The cell of a mesh-generating point encompasses all points that are closer to this mesh-generating point than to any other. The Voronoi tesselation can be obtained by drawing a perpendicular line through the middle of each line of the Delaunay triangulation.

tropy generation via an artificial viscosity. Such a solution is fine for shocks but it makes the remainder of the simulation overly diffusive. Thus, the key to modelling shocks accurately is the challenging problem of introducing the artificial viscosity in such a way that it only affects shock-fronts.

2.2.2 The moving mesh code Arepo

An innovative solution to the trade-off between Lagrangian and Eulerian methods presented above is a combination of the two, such as in the moving mesh code Arepo (Springel, 2010) or mesh-free finite mass and mesh-free finite volume methods of Gizmo (Hopkins, 2015). The Arepo code, which is used in Chapter 5, is based on an unstructured moving mesh of gas cells. This mesh is created via a Delaunay triangulation and a Voronoi tesselation from a set of mesh-generating points (see Fig. 2.3). The cells defined by this method can move essentially arbitrarily and the gas can flow between the cells. The code can be made to behave like an Eulerian code by fixing the mesh-generating points, or like a fully Lagrangian code by forcing them to move along exactly with the flow. However, in most applications, a mixture of these two behaviours is desired. The cells are moving along with large scale flows, while

smaller-scale flows and in particular shocks are modelled by passing gas between the cells. Thus, the code is Galilean invariant but is also able to model shocks and turbulence without introducing artificial viscosity terms. As the CFL criterion only demands the shortest time-steps for the smallest cells, Arepo employs an adaptive time-stepping scheme where larger cells evolve on larger time-steps. Additionally, we make use of the improved integration (Pakmor et al., 2016) and mesh regularization schemes (Mocz et al., 2015). Arepo is one of the most advanced simulation codes for astrophysical applications. It has been used for a wide range of applications, including the large scale cosmological simulations *Illustris* (Vogelsberger et al., 2014) and *Illustris TNG* (Springel et al., 2018, Pillepich et al., 2019), simulations of first star formation (Greif et al., 2012, Wollenberg et al., 2020), simulations of Type Ia (Gronow et al., 2021) and CCSNe (Chan et al., 2018) and simulations of alternative dark matter models (Mocz et al., 2017).

2.2.3 Chemistry, cooling, sink particles and Supernovae

In addition to gravity and hydrodynamics, the simulation presented in 5 requires the ability to model a larger set of physical processes. The key to simulating the formation of the first stars lies in accurately modelling the non-equilibrium chemistry and cooling processes. Computing the chemical composition is important, as the atoms and molecules in the primordial gas can, under the right circumstances, be lifted into excited states by collisions and decay into the ground states by emission of photons. If these photons escape from the gas clouds they originate in, they carry away some of the thermal energy, reducing the internal pressure until the cloud becomes gravitationally unstable, collapses and forms stars. Thus, chemistry and cooling are intimately linked to star formation in general. For our purposes, primordial gas consists only of three nuclei, namely, hydrogen, deuterium (D) and helium. While the trace amount of lithium present in primordial gas is relevant for modelling non-ideal magnetohydrodynamics in primordial gas clouds (Schober et al., 2012), its effect on the gas-cooling is considered to be negligible (Glover & Savin, 2009). Thus, in the absence of heavy elements, the chemical species that need to be considered are H, D, H_2, HD, H^+, D^+, He, He^+, He^{++} as well as free electrons e^-. To solve the accurate abundances of these species as well as the cooling rates, we use the non-equilibrium primordial chemistry network by Glover & Abel (2008), including updates introduced by Glover (2015). The chemical species that are not included here are very rare and do not have any significant effects (e.g. D_2)

or the time-scales for their formation and destruction are so small that they can be considered to be in equilibrium (e.g. H^-).

As described in the introduction (1.4.7), there are several schemes for modelling the collapse of gas clouds without continuously increasing the resolution until the simulations stall. The simulation presented here makes use of so-called sink particles. These are collisionless particles that absorb material that collapses onto them. A detailed description of these particles can be found in Tress et al. (2020). The formation of sink particles is controlled by two parameters, a nucleon number density threshold $n_{\mathrm{th}} = 10^4\,\mathrm{cm}^{-3}$ and an accretion radius R_{acc}, which is chosen to be the Jeans-length at the formation threshold for a characteristic density (in our case $R_{\mathrm{acc}} \approx 3\,\mathrm{pc}$). Cells are considered to be sink-candidates if they have a nucleon number density of more than n_{th}, are located at a local gravitational potential minimum, and do not already contain sink particles within R_{acc}. Such a cell is then converted into a sink particle if the region within the R_{acc} fulfils the following criteria:

1. the region around the sink is converging, i.e., $\nabla \cdot \vec{v} < 0$,
2. the region is collapsing, i.e., $\nabla \cdot \vec{a} < 0$, and
3. the region is gravitationally unstable, i.e., the binding energy E_{grav}, the kinetic energy E_{kin} and the thermal energy E_{th} fulfil

$$E_{\mathrm{grav}} > 2(E_{\mathrm{kin}} + E_{\mathrm{th}}). \tag{2.8}$$

Additionally, the sink particles can remove mass exceeding n_{th} from cells within R_{acc}, if those cells are bound to and falling onto the sink. This means that sink particles keep growing in mass until the accretion is stopped by feedback processes or until the supply of material to be accreted runs out. By default, our sink particles use a Poisson sampling technique (Sormani et al., 2017) to convert part of the accreted mass into stars. This technique statistically preserves the number of stars created when a fixed mass is accreted, irrespectively of how many time-steps this accretion occurs over. However, in order to focus on PISNe, all sink particles are assigned exactly one $200\,\mathrm{M}_\odot$ star independently of how massive they are and of how much mass they accrete in this thesis.

Once the first stars form, they affect their environments with stellar feedback. The two types of feedback we consider are radiative feedback, discussed below, and SN feedback, discussed here. In the simulation presented in this thesis, all stars

explode as PISN with an explosion energy of $E_{\rm SN} = 10^{53}$ erg. The SNe are modelled by injecting their explosion energy as thermal energy into the surrounding cells. For this purpose, we select the 10000 closest cells to the sink-particle and increase their temperature and modify their chemical state accordingly. The energy is distributed such that all cells in this region have the same temperature. Due to the self-similarity of the Sedov-Taylor phase, the SN remnant loses the "memory" of its prior state and converges towards the correct solution, provided that the injection region is so small that radiative energy loss is initially negligible (see Section 1.4.8). In our simulation, this is always the case. Similarly to the sink particles, the SNe were implemented by Tress et al. (2020) and merely adapted to the cosmological unit system for this application.

2.2.4 Radiative transfer: Sprai

Radiative transfer schemes can be categorised into several groups. The first group of schemes treats radiation as a fluid, e.g. as done in flux-limited diffusion (Krumholz et al., 2007) or the M1 scheme (Kannan et al., 2019). While such approximations are usually computationally efficient, they introduce unphysical behaviour to the radiation fields. Examples of these issues are radiation diffusing into areas that should be shadowed or radiation fields originating from different directions bouncing off of each other. The second group are ray-tracing schemes, such as Moray (Wise & Abel, 2011) or the Monte Carlo raytracing schemes radmc-3d (Dullemond et al., 2012) or polaris (Reissl et al., 2016). For a sufficiently large number of rays, these schemes can be highly accurate, and they are particularly common in post-processing and for the generation of synthetic observations. However, these methods can be extremely computationally expensive and the cost rapidly increases with the required resolution of the ray-tracing and the number of radiation sources.

In the simulation presented here, I use the radiative transfer code Simplex Photon Radiation in the Arepo Implementation (Sprai) (Jaura et al., 2018, 2020). This is a radiative transfer scheme from the short-characteristic class, based on Kruip et al. (2010) and Paardekooper et al. (2010). In this method, photon packages are assigned to the individual gas cells and are transported between the cells until all photons are absorbed or escape the simulated region (see Fig. 2.4). This method is not as diffusive as typical fluid-based schemes, although still more diffusive than ray-tracing. A big advantage in comparison to ray-tracing is that the photon packages can all be injected and processed simultaneously, and thus increasing the number of

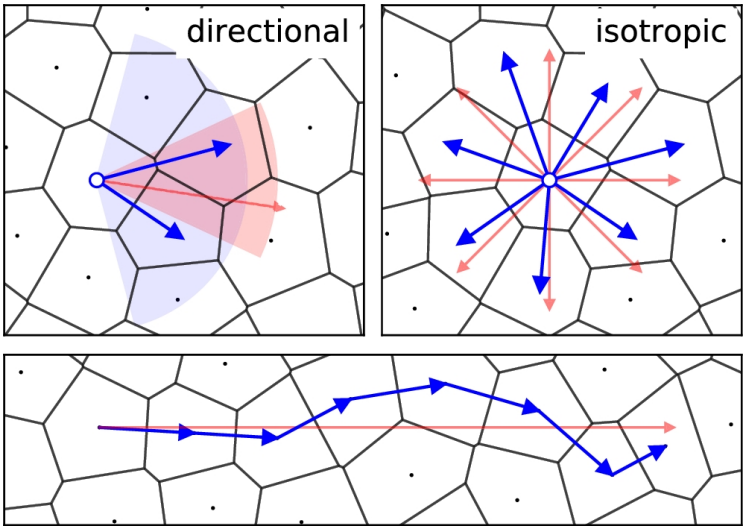

Figure 2.4: Visualization of the SPRAI radiative transfer scheme from Jaura et al. (2018). Photons packages are initially inserted isotropically into the source cells (top right panel). When a photon package leaves a cell, it is transferred to the neighbouring cells according to its direction (top left panel). This process is repeated iteratively, such that the net movement of the photon package corresponds to its assigned directory (bottom panel).

sources only leads to mild increases in computational cost. As the method requires knowledge of the complete mesh of cells, the radiative transfer is only performed on the largest time-steps, the so-called full-hydro step.

3

Observational constraints on the survival of pristine stars

Published as Magg et al. (2019)

There is a longstanding discussion about whether low mass stars can form from pristine gas in the early Universe. A particular point of interest is whether we can find surviving pristine stars from the first generation in our local neighbourhood. We present here a simple analytical estimate that puts tighter constraints on the existence of such stars. In the conventional picture, should these stars have formed in significant numbers and have preserved their pristine chemical composition until today, we should have found them already. With the presented method most current predictions for survivor counts larger than zero can be ruled out.

Disclaimer

This chapter was published by the Monthly Notices of the Royal Astronomical Society as Magg et al. (2019). The text has been primarily written by me but in collaboration with all listed coauthors. The methods, ideas and figures in this chapter are my work and have been developed with feedback from all collaborators.

3.1 Computing detection probabilities

3.1.1 Basic idea

The idea to constrain the existence of surviving pristine stars by statistically analysing non-detections is not new. There are two common methods: Hartwig et al. (2015) and Ishiyama et al. (2016) have estimated the probability to find Pop III survivors in a blind survey and have stated required sample sizes to falsify the predicted numbers at various confidence levels. However, this approach only looks at blind surveys and does not take into account that observers are actually more efficient in finding metal-poor stars than a blind survey. Oey (2003), Tumlinson (2006) and Salvadori et al. (2007) have considered implications of non-detections based on detected numbers of stars, but do not discuss the statistical significance of their statements.

Our goal is to understand the implications of the non-detection of metal-free stars by the community until today. A key problem in this is the large non-uniformity in selection criteria employed by the observations. Our approach is based on the following idea: the formation sites of extremely and ultra metal-poor stars are thought to be similar to those of metal-free stars. They both are expected to form in high-redshift mini- and atomic cooling haloes. Therefore, we are not aware of any reason why their spatial distribution, ages, luminosity or magnitudes in broad band filters should be significantly different. This idea is confirmed by the simulations of Starkenburg et al. (2017a), where metal-poor and metal-free stars show very similar spatial distributions. Consequently, we assume that on average extremely metal-poor stars are equally likely to be detected as Pop III survivors. The detection of each EMP star known to the community can be seen as randomly drawing a star from a sample that contains all EMP stars as well as the hypothetical metal-free stars. Therefore, the probability of metal-free stars randomly escaping detection

thus far can be computed as

$$P_0 = \left(1 - \frac{N_{\rm surv}}{N_{\rm EMP,tot}}\right)^{N_{\rm EMP,obs}}, \tag{3.1}$$

where $N_{\rm EMP,tot}$ is the total number of EMP stars in the galactic halo, $N_{\rm EMP,obs}$ is the number of such stars that are observed and $N_{\rm surv}$ is the total number of surviving metal-free stars in the halo. We note that $N_{\rm EMP,tot}$ includes all stars with a metallicity below [Fe/H] $= -3$ and therefore in particular ultra metal-poor (UMP) stars and potential metal-free stars. A similar estimate is made for UMP stars.

As stated before, Oey (2003), Tumlinson (2006) and Salvadori et al. (2007) have performed similar investigations and concluded that low-mass Pop III stars must form rarely and that the pristine IMF must be very different from the one observed in the present day Universe. Tumlinson (2006) introduced the parameter F_0 which is the fraction of Pop III stars among all stars with a metallicty below [Fe/H]<-2.5. They compute the upper limit from the total number of observed stars in this metallicity range $N_{-2.5,\rm obs}$ to be

$$F_0 < \frac{1}{N_{-2.5,\rm obs}}. \tag{3.2}$$

This method does not allow one to draw any conclusions about the statistical significance of their approach. For example, if we assume a detection rate that is twice the "upper limit" derived with this method and use that number in Equation (3.1), we find for $N_{-2.5,\rm obs}$ a probability of non-detection of

$$P_0 = \left(1 - \frac{2}{N_{-2.5,\rm obs}}\right)^{N_{-2.5,\rm obs}} \approx \frac{1}{e^2} = 13.5\,\%. \tag{3.3}$$

Thus the "upper limit" of F_0 could be violated by a large margin while still being consistent with the observations it has been derived from. Oey (2003) and Salvadori et al. (2007) use a similar method.

Our approach goes beyond simply looking at the fraction of stars and instead considers the full probability distribution, thus allowing us to determine the full significance intervall. It also enables us to easily include different metallicity ranges, as we will demonstrate below.

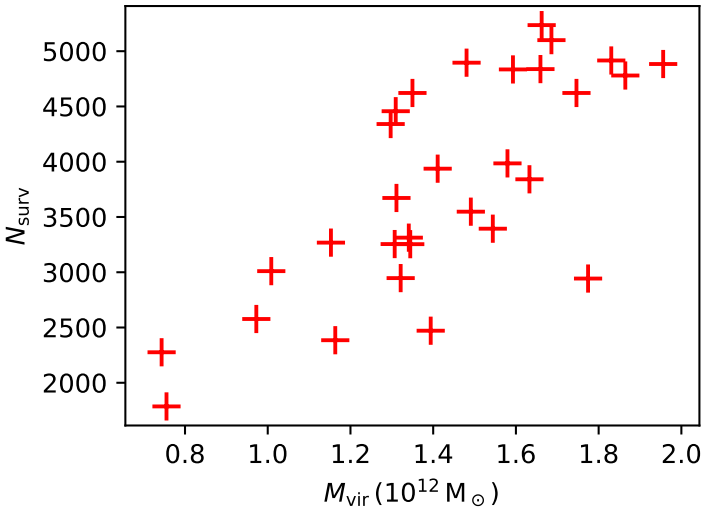

Figure 3.1: Number of surviving pristine stars in the Milky-Way for the 30 Milky-Way-like haloes as function of their virial mass. The numbers of these stars were computed by Magg et al. (2018) on the basis of merger trees from Griffen et al. (2016).

3.1.2 Number of Pop III survivors

We use 30 different numbers of pristine survivors in the Milky Way presented in Fig. 3.1. Magg et al. (2018) computed these numbers with a semi-analytical model, which simulates early star formation in merger trees of Milky-Way-like haloes. The merger trees used for this purpose are from the high-resolution cosmological N-body simulations from the Caterpillar project (Griffen et al., 2016). The assumed IMF in this model is a logarithmically flat IMF in the mass range 0.6-150 $M_\odot$. This IMF is very top-heavy and it gives many fewer surviving stars than, for example, a Salpeter-like IMF in the same mass range. The number-count of surviving pristine stars spans a range between 1800 and 5200 stars. It is extremely difficult to estimate the error for the survivor count in each individual of the 30 modelled haloes. We assume that the main source of errors is encompassed in the different merger histories of the 30 haloes, i.e., that the 30 survivor counts represent the probability distribution of expected survivor counts in the Milky-Way. Even the largest number of surviving pristine stars we adopt is by a factor of two smaller than the one found in Hartwig et al. (2015, 10000 survivors) on which the Magg et al. (2018) study is built. This difference is primarily caused by the significantly improved modelling of feedback and in particular by taking into account the positions of the haloes and the effects of ionizing radiation. The adopted numbers of Pop III survivors are also by more

than order of magnitude smaller than the one in Ishiyama et al. (2016, around 100000 survivors). This discrepancy is mostly caused by assuming around an order of magnitude more survivors per Pop III forming minihalo. Komiya et al. (2016) predicted around 3000 Pop III survivors in the Milky-Way, similarly to our estimate. Therefore, our estimate of the number of surviving pristine stars is among the more conservative predictions that still allow for surviving Pop III stars. Salvadori et al. (2007) and de Bennassuti et al. (2017) also investigate the possiblity of surviving Pop III stars in the Milky-Way and make predictions for how common they are. As they only derive the fraction of a certain group of stars that should be metal-free and do not give absolute numbers, direct comparisons to the survivor counts are difficult. We will investigate the consistency of their predictions with the current state of observations below.

3.1.3 Total number of EMP stars in the halo

To compute with which probability a number of metal-free stars could have escaped detection until now, we have to determine the size of the "haystack", i.e., the total number of EMP/UMP stars among which we have to look for pristine survivors. In order to do this we assume that all EMP, UMP and hypothetical pristine stars are located in the stellar halo of the Milky-Way. Simulations and semi-analytical modelling confirm that most of surviving metal-free stars should be found in the stellar halo (Hartwig et al., 2015, Starkenburg et al., 2017a). Sestito et al. (2019) recently found that the majority of known UMP stars indeed are observed in the stellar halo. Therefore, our estimates of the total amount should be appropriate. Furthermore this assumption only enters in our estimate of the size of the "haystack", i.e., our model is independent of it as long as it does not lead to us significantly underestimating the total number of EMP/UMP stars in the Milky-Way.

We assume a stellar halo mass of $M_{*,\mathrm{halo}} = 10^9\,\mathrm{M}_\odot$ (Bell et al., 2008). We convert this to a number of stars by assuming an average stellar mass of a typical old metal-poor main sequence turn-off star, i.e. $M_* = 0.6\,\mathrm{M}_\odot$. This is again a conservative estimate, which probably significantly overestimates the number of EMP and UMP stars. Thus it gives a relatively large "haystack", assuming that all stars are at the smallest mass where they can still be detected and the metallicities constrained reasonably well. For the same reason the lower limit of the pristine IMF was selected to be $0.6\,\mathrm{M}_\odot$ in Magg et al. (2018). Recently, Youakim et al. (2017) estimated that 1/800 of halo stars are EMP stars and 1/80000 of halo stars are UMP stars. Thus,

we estimate the total number of EMP and UMP stars to be

$$N_{\mathrm{EMP,tot}} = \frac{M_{*,\mathrm{halo}}}{800 M_*} = 2.08 \times 10^6 \tag{3.4}$$

and

$$N_{\mathrm{UMP,tot}} = \frac{M_{*,\mathrm{halo}}}{80000 M_*} = 20800. \tag{3.5}$$

While these numbers are subject to large uncertainties they are the best estimates available to us. To be conservative, we also use a very pessimistic conversion factor between stellar mass and the number count of stars. One source of uncertainty is that Youakim et al. (2017) derived those numbers for stars in the magnitude range $14 < V < 18$ and that EMP and UMP stars could be more common in the more metal-poor outer stellar halo. Therefore, we will discuss below how our results would change, if we underestimated the number of EMP and UMP stars by a factor of two.

3.1.4 Number of detected stars

For the number of observed UMP stars we use the $N_{\mathrm{UMP,obs}} = 42$ stars from Sestito et al. (2019). We determine the number of detected EMP stars to be $N_{\mathrm{EMP,obs}} = 532$ by a query of the SAGA[1] database (Suda et al., 2008). Of these stars, 507 are in the metallicity range $-4 < [\mathrm{Fe/H}] < -3$. With this method, we are underestimating the number of detected EMP stars as we do not include e.g. the recent detections from TOPoS (François et al., 2018) or LAMOST (Li et al. 2018, Li et al. in prep.).

3.2 Results and discussion

By using the estimated numbers of survivors, EMP and UMP stars and their detections, we can compute the probability of the non-detection of these metal-free stars until today with Eq. (3.1). The probabilities for individual haloes are presented in Fig. 3.2. The non-detection probabilities derived from EMP stars are typically around 50 per cent, while the values derived from the UMP star sample are orders of magnitude smaller. If we remove the UMP stars from the detected EMP sample, i.e., using $N_{\mathrm{EMP,obs}} = 507$, the two non-detection probabilities become independent. We can combine them by multiplication. These combined probabilities offer a slight improvement over the estimate derived from detections of UMP stars. As the 30 simulated merger trees represent our a priori distribution of survivor counts,

[1] `http://sagadatabase.jp`, accessed on 22.01.2019

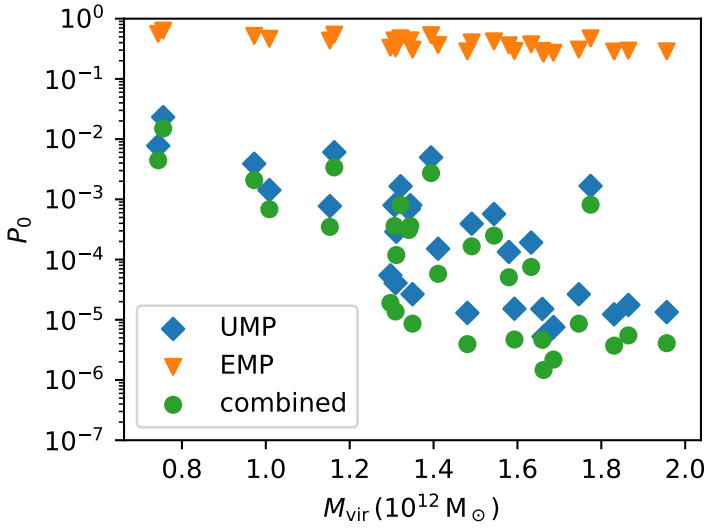

Figure 3.2: Probability of not detecting metal-free stars until today, as function of halo mass. We show the probabilities derived from UMP (blue diamonds) and EMP (orange triangles) star detections separately and combined (green circles). The UMP stars give much tighter constraints than the EMP stars.

we compute final non-detection probabilities in the Milky-Way by averaging the 30 probabilities. We find

- $P_{0,\rm EMP} = 0.39$ for EMP stars,
- $P_{0,\rm UMP} = 0.0019$ for UMP stars and
- $P_{0,\rm comb} = 0.0011$ combined.

Thus the estimate of the number of metal-free survivors can excluded at a 99.9 per cent confidence level. At 98 per cent confidence level, this model allows for no more than 1650 metal-free stars. This also rules out the predicted number of survivors from Hartwig et al. (2015) and Ishiyama et al. (2016). The non-detection probabilities derived from EMP stars are typically around 50 per cent, while the values derived from the UMP star sample are orders of magnitude smaller. Even if we underestimate the number of EMP and UMP stars by a factor of two, the predictions from Magg et al. (2018) are still incompatible with our estimate at a confidence level of 97 per cent.

While the study by de Bennassuti et al. (2017) does not include an absolute number of surviving stars, they state that for one of their IMFs, they find that

0.15 per cent of EMP stars should be metal-free. For this prediction they use a Larson-type IMF with the shape

$$\frac{\mathrm{d}N}{\mathrm{d}m} \propto m^{-2.35} \exp\left(\frac{-0.35\,\mathrm{M}_\odot}{m}\right), \tag{3.6}$$

between mass limits of $0.1\,\mathrm{M}_\odot$ and $300\,\mathrm{M}_\odot$. If we continue to assume that one per cent of EMP stars are UMP stars, we can use our formalism to determine the probability of non-detection to be

$$P_0 = (1 - 0.0015)^{507}(1 - 0.15)^{42} = 0.05\,\%, \tag{3.7}$$

ruling out their assumed IMF with 99.95 per cent confidence. However, it is not clear whether our assumption of the ratio between UMP and EMP stars is consistent with their metallicity distribution function.

Salvadori et al. (2007) investigate three cases of different critical metallicities, at which the transition from the primordial to the present day IMF occurs. They result in $F_0 = 7.5 \times 10^{-3}$ for a critical metallicity of $Z_{\mathrm{cr}} = 0$ and $F_0 \approx 7.5 \times 10^{-9}$ for $Z_{\mathrm{cr}} = 10^{-4}\,\mathrm{Z}_\odot$ and $Z_{\mathrm{cr}} = 10^{-6}\,\mathrm{Z}_\odot$, where $\mathrm{Z}_\odot$ is the solar metallicity. As the former value was already ruled out by the observations at the time of publication and the latter two are extremely low values, no further conclusions can be drawn from applying more recent observations to their predictions.

In addition to upper limits, we can compute our best estimate of the number of surviving metal-free stars. At merely $N_{\mathrm{surv}} = 300$ the non-detection of metal-free stars until today becomes equally likely to their detection (i.e. $P_{0,\mathrm{comb}} = 0.5$).

These findings imply either that low mass Pop III stars must be rarer than suggested by Magg et al. (2018) or a significant number of them must accrete metals from their surroundings during their life. We will briefly discuss both possibilities here.

A possible explanation for the non-detection of metal-free stars is that they could have been enriched with accreted metals from the interstellar or intergalactic medium during their lifetime, and are now detected among the metal-poor stars. Whether such accretion can occur at a sufficient level to explain the non-detection of metal-free stars is still under debate. Frebel et al. (2009) found that metal-poor stars can only very inefficiently accrete metals, while Johnson & Khochfar (2011) find accretion can be efficient, if it is not prevented by stellar winds. If enrichment is efficient, Komiya et al. (2016) predicted that around 100 – 170 stars may escape their

formation sites before being enriched and be accreted onto the Milky-Way stellar halo at later times. However, such stars may have a different distribution of orbits and can therefore not be investigated with the model presented in this chapter. More recently Tanaka et al. (2017) and Suzuki (2018) pointed out that magnetic winds and hot coronae of Pop III survivors may prevent accretion of metals from the insterstellar medium altogether. Accretion of compact interstellar comets has been investigated as source of metal pollution by Tanikawa et al. (2018), and the contribution was found to be negligible in most cases.

A second possible pathway that leads to the pollution of surviving Pop III stars is mass overflow in binaries. For example, Suda et al. (2004) and Lau et al. (2007) have shown that under the right conditions significant pollution with carbon can occur in Pop III binaries. Observationally, Arentsen et al. (2019) suggest a connection between carbon enhancement and binarity in EMP stars. Such mass transfer would be sensitive to the binarity and the separation of Pop III stars, which is so far not well constrained. However, in most cases binary mass transfer is insufficient as source of enrichment, as it cannot explain the presence of iron in these stars. Therefore, in order to explain the lack of observed surviving metal-free stars by pollution, the need for accretion from the interstellar medium remains.

The most obvious explanation for the non-detections of Pop III survivors, would be that metal-free stars with masses below $0.8\,\mathrm{M}_\odot$ do not form at all or are much rarer than predicted. This would mean that the pristine IMF must either be more top heavy or truncated towards lower masses. We perform a simplistic estimate here of how much we would need to change the IMF form the one assumed in Magg et al. (2018) in order to arrive at survivor numbers consistent with observations. Magg et al. (2018) used a logarithmically flat IMF in the mass range 0.6-150 $\mathrm{M}_\odot$. Such an IMF produces on average one surviving star per $520\,\mathrm{M}_\odot$ of forming Pop III stars, where we assumed that these stars survive in the range of 0.6-0.8 $\mathrm{M}_\odot$. For comparison, the present day IMF from Kroupa (2001) predicts around one star in this mass range per $10\,\mathrm{M}_\odot$ of stars formed. The assumed pristine IMF leads to the prediction of an average of 3750 surviving Pop III stars. At fixed star formation efficiency and feedback efficacy, to scale this number down to the above given upper limit of 1650 survivors, we would need to reduce the number of survivors to one per $1200\,\mathrm{M}_\odot$ of Pop III stars. This could either be achieved by raising the lower limit of the IMF to $0.7\,\mathrm{M}_\odot$ or by changing its slope from $\alpha = -1.0$ (i.e., logarithmically flat) to $\alpha = -0.8$. In particular, these constraints are strongly inconsistent with Pop III stars forming with an IMF similar to the one observed in the present day.

Without pollution of almost every low-mass Pop III star, an IMF that, compared to the present day IMF, is either very top-heavy or truncated towards sub-solar masses is required.

The largest uncertainty in our method lies in our estimate of the total size of the "haystack", i.e. the total number of EMP and UMP stars in the Milky Way and in particular in the outer stellar halo. While the numbers used in this paper are uncertain we chose a conservative estimate. Future surveys that allow to more completely and deeply explore the outer stellar halo will reduce these uncertainties. Additionally, the number of UMP and in particular EMP stars cited in this chapter are lower limits, as the SAGA catalogue is not entirely up-to-date and because there are more processed, but not yet published detections of EMP stars (Li et al. in prep).

In summary, we derived new upper limits on the number of surviving metal-free stars in the Milky-Way. We conclude that such stars must form very rarely or else have been polluted by metals during their lifetime. We demonstrate the ability of our approach to constrain the primordial IMF by non-detections and highlight the need for a lower mass cut-off of the IMF or an even more top-heavy functional form than adopted here, should pollution of these stars not be significant. Future surveys and individual detections of EMP and UMP stars will further strengthen constraints on the survival of metal-free stars.

4

A minimum dilution scenario for SNe and consequences for EMP stars

Published as Magg et al. (2020)

To date no metal-free stars have been identified by direct observations. The most common method of constraining their properties is searching the spectra of the most metal-poor stars for the chemical elements created in the first stars and their SNe. In this approach, modelled SN yields are compared to the observed abundance patterns in extremely metal-poor stars. The method typically only uses the abundance ratios, i.e., the yields are diluted to the observed level. Following the assumption of spherical symmetry we compute a lower limit of the mass a SN can mix with and find that it is consistent with all published simulations of early chemical enrichment in the interstellar medium. For three different cases, we demonstrate that this dilution limit can change the conclusions from the abundance fitting. There is a large discrepancy between the dilution found in simulations of SN explosions in minihaloes and the dilution assumed in many abundance fits. Limiting the dilution can significantly alter the likelihood of which SNe are possible progenitors of observed CEMP-no stars. In particular, some of the faint, very low-yield SNe, which have been suggested as models for the abundance pattern of SMSS0313-6708, cannot explain the measured metal abundances, as their predicted metal yields are far too small.

Disclaimer

This chapter was published by the Monthly Notices of the Royal Astronomical Society as Magg et al. (2020). The text has been primarily written by me but in collaboration with all listed coauthors. The methods, ideas and figures in this chapter are my work and have been developed with feedback from all collaborators.

4.1 The minimum mixing mass

4.1.1 Analytic estimate

As outlined before, abundance fitting usually employs the observed ratios of abundances of certain metals and compares those to the ratios found in theoretical SN models. Of particular importance is, e.g., the [C/Fe] ratio. This method, however, typically neglects the actual abundance value (i.e., [Fe/H] or [C/H]) and treats them as an arbitrary normalization factor. Conceptually, this normalization can be achieved by diluting the SN yields with the correct amount of metal-free gas. As in published works usually only single SNe are fitted to observed abundance patterns, we only consider single, isolated SNe in this work.

We consider SN explosions as well as their subsequent expansion into the ambient medium and the corresponding mixing processes in spherical symmetry. Simulations carried out in two (Tominaga, 2009) and three (Chan et al., 2020) dimensions, however, show that Pop III SNe can be strongly aspherical. In this context, we note that even when considering anisotropic SNe, the observed abundances in most published studies are compared to angle-integrated yields. This means that the problem considered is effectively spherically symmetric, as the angular average implies that different elements ejected in different directions become well mixed before the second generation stars form. An exception to this may be, if the abundances are distributed more spherically than the energy input, such as seen in some of the models in Tominaga (2009). A critical analysis of the validity of this approximation is one of the primary motives for the work presented here. We argue that properly accounting for the asymmetries expected in Pop III SNe requires both detailed three dimensional explosion models as well as high-resolution simulations of the expansion of the resulting anisotropic shock wave into an inhomogeneous ambient medium that are able to adequately follow the chemical mixing process.

Since there is no analytic model for such a small-scale inhomogeneous mixing, however, we follow the bulk of the existing literature and approximate the SN as

a spherical explosion inside a homogeneous ambient medium. As SNe are very energetic events, a large amount of gas is required to confine the metals and thus not all dilution masses are physically plausible. The lowest limit for this mass is the mass enclosed in the final radius of the SN remnant. Analytical solutions to spherical blast waves of SNe can be derived under a variety of assumptions (e.g., Ostriker & McKee, 1988), with the expansion of the remnant stalling at the end of the momentum-driven snowplough phase. In this phase, the expansion velocity reaches the speed of sound in the ambient medium. As shocks cannot be subsonic, the shock wave transforms into a sound wave and dissipates. This occurs at the fade-away radius $R_{\rm fade}$ (see Section 1.4.8) which is

$$R_{\rm fade} \approx 2.07 \times 10^{20}\,{\rm cm}\; E_{51}^{0.32} n_0^{-0.37} \left(\frac{c_{\rm s}}{10\,{\rm km\,s^{-1}}}\right)^{-2/5}, \tag{4.1}$$

where n_0 is the nucleon number density of the ambient medium in units of ${\rm cm}^{-3}$, E_{51} is the explosion energy in units of $10^{51}\,{\rm erg}$ and $c_{\rm s}$ is the ambient medium speed of sound (e.g., Draine, 2011). We assume the ambient medium is ionized, i.e., that it has a speed of sound of $c_{\rm s} = 18\,{\rm km\,s^{-1}}$, for a metal-free HII region (see e.g., Abel et al., 2007). In case the medium is actually neutral, the speed of sound would be lower and the stalling radius larger. Thus, this is a conservative assumption. In the homogeneous mixing case, the minimum mass with which the ejecta are mixed is the mass that is enclosed in the stalling radius, i.e.,

$$M_{\rm dil,min} = \frac{4}{3}\pi n_0 \mu m_{\rm H} R_{\rm fade}^3 = 1.9 \times 10^4\,{\rm M}_\odot\, E_{51}^{0.96}\, n_0^{-0.11}, \tag{4.2}$$

where $m_{\rm H}$ is the mass of a hydrogen nucleus and where we assumed a mean molecular weight of $\mu = 1.22$. The fade-away radius used here is for gas cooling rates of solar metallicity gas. We discuss the assumption of solar metallicity and dependence of the dilution mass on the metallicity in Appendix 4.4. As we aim at computing a lower limit for the mixing mass, the reduced cooling can be neglected. By definition the SN remnant expands faster than the speed of sound in the ionized medium. As we consider haloes below the atomic cooling limit the escape velocity from the haloes is much smaller than this speed of sound. Therefore, SN remnants expand much faster than the escape velocity and the effect of gravity can be neglected.

This result is very similar to the one obtained through numerical simulations by Thornton et al. (1998). While it has been widely used in the discussion of stellar feedback, it is often neglected when fitting abundance patterns of individual

stars. For example, Tominaga et al. (2014) note that the minimum dilution mass obtained by Thornton et al. (1998) is not a binding limit, as metal mixing is highly inhomogeneous (Ritter et al., 2012). We will later see that our derived limit holds even in cases of inhomogeneous mixing.

We assume an ambient density of $n_0 = 1\,\mathrm{cm}^{-3}$, which should be the typical case for the ionized regions around massive Pop III stars (Whalen et al., 2004). We note that the density dependence of the minimum mixing mass (Eq. 4.2) is very weak, so it would need to be higher by several orders of magnitude to affect our conclusions. If the density is this much higher than the assumed value, the free-fall time of the ambient gas is smaller than the life-time of the star, and thus it should form stars already before the SN explodes or while the remnant expands. Furthermore, simulations show that it is difficult to mix metals into gas that is already very dense when the SN explodes (Ritter et al., 2016, Chiaki et al., 2018).

Under the assumptions outlined above, the dilution mass is a lower limit for two main reasons:

1. We assume a homogeneous medium. If the medium is not homogeneous the denser gas will be less enriched but form stars first. This effect is discussed further below.

2. We assume no further mixing. Realistically further mixing with additional pristine gas should occur during recollapse, rather than the stalled SN remnant monolithically collapsing back on itself. This effect would further increase the dilution mass.

We note that we assume all SNe are able to produce second generation stars. Very energetic explosions may actually disrupt their host haloes, which suppresses or delays second generation star formation (Whalen et al., 2008). This effect is difficult to quantify without hydrodynamical simulations in cosmological context, and is therefore neglected here.

4.1.2 Consistency with simulations

To see whether sub-galactic-scale inhomogeneous mixing can lead to higher metallicities than predicted by the minimum dilution we will compare it to the dilution found in all suitable published simulations of inhomogeneous mixing and the formation of second generation stars which we are aware of. For comparison with our limit, we use an ambient density of $n_0 = 1\,\mathrm{cm}^{-3}$ in all cases but take the explosion

energies used in the simulations to compute the minimum mixing. Simulations are included if they

- are three dimensional hydrodynamical simulations of the expansion of Pop III SN remnants into their ambient medium,
- model individual, isolated, Pop III SNe, and not groups or clusters of stars,
- follow the enriched gas until it re-collapses, and
- provides the output needed for our comparison.

We cannot compare our model to the simulations of Greif et al. (2007) and Chen et al. (2015) because they simulate only the initial expansion of the enriched material, but not its re-collapse. Larger-scale simulations, such as the ones from Wise et al. (2012), Johnson et al. (2013), or Tarumi et al. (2020b), are not considered, because they do not follow individual isolated SNe. The simulations of Whalen et al. (2008) are not included here because they are one-dimensional. Nevertheless, we note that their metal-enriched gas masses are consistent with our upper limit in most cases. Only in one of their models is the enriched gas mass they find smaller than our prediction in Eq. (4.2). In this case, the star completely fails to create an ionized region, and the ability to model an off-centre re-collapse would be crucial to make accurate predictions for the metallicity of the second generations star.

We begin with the dilution found in Ritter et al. (2012, 2015, 2016).[1] In all three simulations the SNe considered are core collapse (CC) SNe with $E_{51} = 1$. They eject $M_{\rm met} = 4\,\mathrm{M}_\odot$ of metals in Ritter et al. (2012, 2015) and $M_{\rm met} = 6\,\mathrm{M}_\odot$ in Ritter et al. (2016). Thus, according to Eq. (4.2) the maximum final metallicity we should expect is

$$Z_{\rm max} = \frac{M_{\rm met}}{M_{\rm dil,min}} \approx 10^{-3.6} \approx 10^{-1.7}\,\mathrm{Z}_\odot \tag{4.3}$$

where $\mathrm{Z}_\odot = 0.0142$ is the solar metallicity (Asplund et al., 2009). While the mixing is highly inhomogeneous, and orders of magnitude of spread in metallicity can be seen, the newly collapsing cores always show metallicities[2] below this value. All simulations also contain gas at higher metallicities than predicted by the minimum dilution. While from Ritter et al. (2012) it is unclear in which phase this gas

[1] We only consider the 1SN model from Ritter et al. (2015) as the 7SN model deals with enrichment by multiple SNe, which is not the topic of our analysis.

[2] For comparison with simulations we generally use the central metallicities of the metal-enriched gravitationally unstable regions, either as reported by the authors of the respective studies or as read from their figures.

is contained, in Ritter et al. (2015, 2016) only some of the very diffuse gas has metallicites above the dilution limit.

Chiaki et al. (2018), Chiaki & Wise (2019) and Chiaki et al. (2020) model the inhomogeneous mixing occurring after the SNe of 9 different stars with masses between $13\,\mathrm{M}_\odot$ and $200\,\mathrm{M}_\odot$. As of today, is by far the largest set of such mixing simulations. Some of these SNe are simulated in several different halos. The simulations cover a wide range of different environments in which SNe can explode. For massive stars, halos are often completely photo-evaporated, whereas, for the lowest-mass stars that they investigate, with $M = 13\,\mathrm{M}_\odot$, the gas in the stellar birth-cloud remains dense throughout the lifetime of the star. The results show large variations between the mixing behavior and the metallicities of the second-generation stars. Chiaki et al. (2018) distinguish between three separate enrichment channels:

1. Internal enrichment: in this case, the SN expands efficiently and the metals mix well with the surrounding gas before the halo collapses back on itself.

2. External enrichment: the metals escape from the halo in which the SN explodes and mix with the gas in a different halo that has not formed stars yet. This type of enrichment is also found in Smith et al. (2015).

3. Inefficient internal enrichment: dense structures remain in the halo. When the SN explodes these structures are only enriched to very low metallicities and proceed to form stars with metallicities much lower than the average gas metallicity in the halo.

None of these simulations, however, show the formation of second generation stars that violate our dilution limit. According to Eq. (4.2) the predicted maximum metallicity ranges between $10^{-2.6}\,\mathrm{Z}_\odot < Z_{\mathrm{max}} < 10^{-1.6}\,\mathrm{Z}_\odot$. All second generation stars from Chiaki et al. (2018) and Chiaki & Wise (2019) have metallicities in the range $10^{-6.3}\,\mathrm{Z}_\odot < Z < 10^{-2.2}\,\mathrm{Z}_\odot$. The second-generation stars in Chiaki et al. (2020) have much lower metallicities, even reaching iron abundances of [Fe/H] < -9. Despite such low metallicities, the dilution mass in these simulations is only one to two orders of magnitude above our lower limit. Compared to other simulations (Fig. 4.1) it is apparent that this dilution behaviour is similar to the other simulations included in our summary. The reason for the extremely low metallicities seen here is not an unusually efficient dilution, but rather that the modelled SNe are faint, low-yield SNe. None of the stars violate our derived limit. The simulated second generation star that is closest to our computed upper limit is enriched by a $25\,\mathrm{M}_\odot$

CCSN that explodes in their halo "MH1", which is their smallest halo with a mass $M_{\rm vir} = 3 \times 10^5\,{\rm M}_\odot$. The re-collapsing region has a metallicity of 40 per cent of our computed upper limit. In these simulations, there are several cases of stars with much lower metallicities than predicted by the minimum dilution model. These are the cases in which the surroundings of the SNe are the most dense and the mixing seen in the simulations is very inhomogeneous. The second generation stars form in clumps that already exist when the SNe explode and only the outer layers of these clumps are enriched with metals. Thus, the enrichment proceeds in what Chiaki et al. (2018) label the "inefficient internal enrichment" channel.

Greif et al. (2010) simulate the explosion of a single PISN with $E_{51} = 10$ and $100\,{\rm M}_\odot$ of metal ejecta. According to our model the maximum metallicity in this extreme case should be below $Z = 10^{-1.4}\,{\rm Z}_\odot$. They find metallicities in the recollapsing galaxy that are around $Z = 10^{-3}\,{\rm Z}_\odot$. As Greif et al. (2010) note, the average metallicities are initially much higher but they decrease to this low value during the recollapse of the halo, which takes around 300 Myr.

The simulations by Jeon et al. (2014) include several SNe exploding in three different haloes. The authors provide information on the metallicity of recollapsing regions in three cases: a 15, 25 and $40\,{\rm M}_\odot$ star exploding in their "halo1". They all explode as $E_{51} = 1$ CCSNe and eject 5 per cent of their stellar mass as metals. According to our model, this should lead to metallicites of $Z < 10^{-2.1}\,{\rm Z}_\odot$. Their reported metallicities are all below $Z = 10^{-3.5}\,{\rm Z}_\odot$.

Smith et al. (2015) highlight the external enrichment channel. Their SN is a $E_{51} = 1$ CCSN which ejects $11.19\,{\rm M}_\odot$ of metals, leading us to predict a maximum metallicity of $Z_{\rm max} = 10^{-1.4}\,{\rm Z}_\odot$. Only a very small fraction of gas is found at such high metllicities, and none of it is in the re-collapsing region. The metal-enriched star forming gas in this case has a metallicity of $Z = 10^{-4.7}\,{\rm Z}_\odot$.

We convert the metallicities found in the simulations back to an "effective dilution mass" with eq. (4.3) and summarize the simulations in Fig. 4.1. None of the simulations of inhomogeneous mixing show inconsistencies with the minimum dilution mass derived from the spherically symmetric case. In some of the simulations, there is gas above the derived upper limit for the metallicity, but it tends to be diffuse and hot. This can be understood intuitively: as thermal energy and metals are ejected together, more metal-rich gas tends to be hotter. It is important to note that there is significant scatter in the simulation results: even for similar exploding stars the effective dilution mass can vary by many orders of magnitude. The cases with the largest effective dilution masses are usually external or inefficient internal

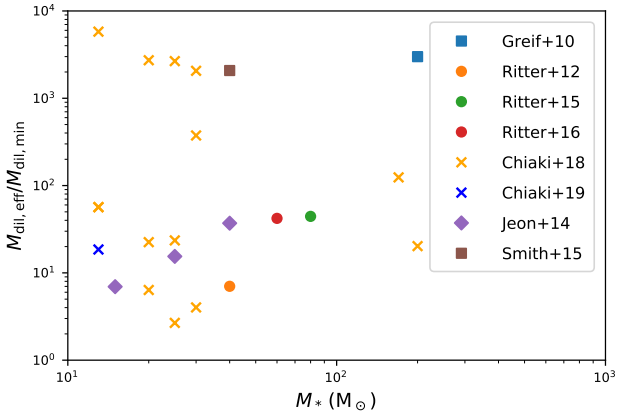

Figure 4.1: Comparison of the minimum dilution model to simulations of inhomogeneous metal mixing. We show the ratio of the effective dilution mass of the simulations and our estimate of the minimum dilution mass as a function of the stellar mass of the exploding star. The effective dilution mass is derived from the metallicity in the second generation stars or the likely sites of second generation star formation in the simulations. All simulations show a ratio above one, i.e. they are consistent with our predicted minimum.

enrichment. We conclude that, to the best of our knowledge and the current state of modelling, our estimate provides a useful limit on the mixing and dilution of metals even in the presence of inhomogeneous mixing.

4.1.3 Bayesian fitting

We will here briefly discuss how the derived limit on mixing can be implemented in abundance fitting codes. For this purpose we create an algorithm that fits observed abundances by comparing to them to the modelled SN yields from Heger & Woosley (2010). The yields of the SNe generally depend on the progenitor mass ($M_{\rm prog}$), the explosion energy (E_{51} in units of 10^{51} erg) as well as a mixing factor ($f_{\rm mix}$). This mixing factor is the mass scale over which abundances in the SN yields are averaged before part of the SN ejecta fall back, expressed as fraction of the mass of the He core of the star. For matching observed and modelled abundances, we use the SN yields and analysis tools provided with STARFIT and supplement them with a generic Bayesian fitting approach. A general description of Bayesian parameter estimation can be found in Bailer-Jones (2017). We first compute the likelihoods $L_i(x_i|M)$ that a model M, which predicts the abundances y_i, results in the observed abundances x_i,

$$L_i(x_i|M) = \exp\left(-\frac{(x_i - y_i)^2}{2\sigma_i^2}\right), \tag{4.4}$$

where i is any of the observed elements and σ_i is the error of the observations. The normalization is left arbitrary for now. This likelihood calculation implicitly assumes that the errors follow a Gaussian distribution. While it is not clear whether this assumption is valid, it is commonly made when fitting SN models to observed abundances (e.g. Heger & Woosley, 2010, Ishigaki et al., 2018, Ezzeddine et al., 2019). Computing the modelled abundances y_i requires, as discussed above, a usually arbitrary dilution mass $M_{\rm dil}$. If M_i is the mass of element i, which has a mass-number of μ_i, that is ejected by a SN, the model abundance is

$$y_i = \log_{10}\left(\frac{M_i}{\mu_i\, X_{\rm H} M_{\rm dil}}\right) - \log_{10}\left(\frac{N_{i,\odot}}{N_{\rm H,\odot}}\right), \tag{4.5}$$

where $X_{\rm H} = 0.754$ is the hydrogen abundance of primordial gas (Planck Collaboration et al., 2016a). The respective solar fractions of the element i and of hydrogen are $N_{i,\odot}$ and $N_{\rm H,\odot}$. We iteratively adjust the dilution mass for each model until we find the dilution that gives the maximum final likelihood according to Eq. (4.7). The dilution mass is picked individually for each model, but within each model the same dilution mass is used for every element. This choice comes from our assumption that each element mixes in the same way. This assumption is commonly made for SN fitting, as without it the SN yields would not be representative of the elements found in the second generation stars.

However, in many cases elements are not detected and only upper limits on their abundance can be derived. These upper limits need to be treated simultaneously with the detections. For this we assume that the upper limits are strict (i.e. the likelihoods are Heaviside step-functions Θ) combined with a Gaussian error on where exactly this limit is. These assumptions lead to a likelihood $L_i(x_i|M)$ for an upper limit of x_i in element i of:

$$\begin{aligned} L_i(x_i|M) &= \int_{-\infty}^{\infty} \Theta(x_i - z_i) \exp\left(-\frac{(z_i - y_i)^2}{2\sigma_i^2}\right) {\rm d}z_i \\ &= \int_{-\infty}^{x_i} \exp\left(-\frac{(z_i - y_i)^2}{2\sigma_i^2}\right) {\rm d}z_i \\ &= \sqrt{\frac{\pi}{2}}\sigma_i \,{\rm erf}\left(\frac{x_i - y_i}{\sqrt{2}\sigma_i}\right), \end{aligned} \tag{4.6}$$

where erf is the Gaussian error function. The theoretical models are understood to predict yields of Sc that are systematically too low and should therefore be treated as lower limits (Heger & Woosley, 2010). We implement this in practice by treating

the measurements as upper limits, since this is equivalent to treating the model predictions as lower limits. The likelihoods of the individual elements can then be combined by multiplication:

$$L(x|M) = \prod_i L_i(x_i|M). \tag{4.7}$$

The same approach to compute fit likelihoods was also used in, e.g., Fraser et al. (2017). In cases where there are only detections and no upper limits, maximizing this likelihood is equivalent to minimizing χ^2. This way of combining likelihoods implicitly assumes that the errors of all abundance determinations are uncorrelated. Especially for errors from uncertainties in the determination of stellar parameters, this may not be true (McWilliam et al., 1995). This is because all low-excitation lines arising from neutral minority species tend to have similar sensitivity to the effective temperature, which typically dominates the error budget. However, we only aim at showing the importance of constraining the dilution of SN ejecta, and a complete treatment of the error distributions and dependencies of abundance determinations exceeds the scope of the current investigation.

If we assign each model in the SN library the same prior probability, we can further compute the probability of each model M given the observations x by

$$P(M|x) = N\, L(x|M), \tag{4.8}$$

where N is a normalization constant chosen such that

$$\sum_M P(M|x) = 1. \tag{4.9}$$

4.2 Application to observations

In this section we demonstrate in three cases why it is important to consider the dilution when fitting abundances of metal-poor stars. Firstly, we will show that it can help to break degeneracies in a fit; secondly, that it may systematically change properties of large fitted samples of stars; and thirdly, that for some stars there may not be a viable single-progenitor scenario to explain the observed abundance patterns.

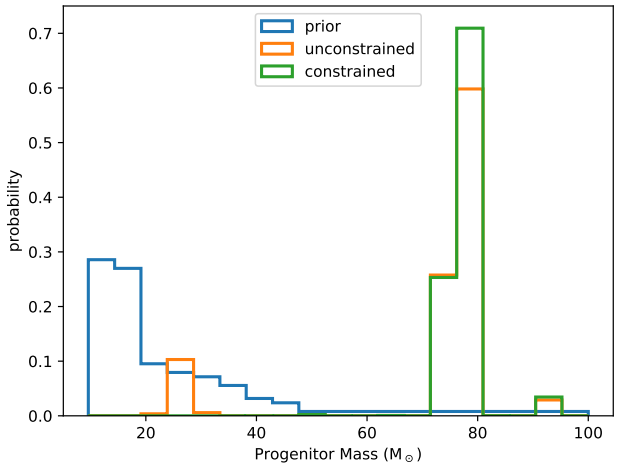

Figure 4.2: Prior (blue) and posterior distribution of the progenitor mass of HE 0020-1741. We show the posterior for unconstrained (orange) and constrained (green) dilution. In the unconstrained dilution there is a bimodal distribution of progenitor masses, whereas with the constrained dilution only high-mass stars match the observed abundances.

4.2.1 Example 1: The progenitor of HE 0020-1741

To investigate the impact of the minimum dilution mass on abundance fitting, we firstly fit the CEMP-no star HE 0020-1741 ([Fe/H] = -3.6). Hansen et al. (2019) have determined abundances for 13 elements (C, N, O, Mg, Ca, Sc, Ti, Cr, Mn, Ni, Fe, Sr, Ba). We chose this star as it is an extremely metal-poor CEMP-no star and therefore thought to carry the chemical signature of a Pop III SN and being unaffected by binary interactions. As the yields from Heger & Woosley (2010) do not include r- and $s-$process elements, Sr and Ba are excluded from the fits.

We show the prior and the posterior distribution of stellar masses in Fig. 4.2. The prior is bottom heavy, as there are many more models of low-mass SNe in the libraries than there are models of high-mass SNe. This could potentially bias fitting results towards lower masses. We perform the fits with unconstrained and with constrained dilution factors. In the former case, we chose the dilution factors to maximize the combined likelihoods as defined in Eq. (4.7). In the latter case, we only allow dilution factors above our analytical limit. For the unconstrained dilution we find a bimodal posterior: there are solutions with progenitor masses either around $M_* \approx 25\,\mathrm{M}_\odot$ or at $M_* \approx 80\,\mathrm{M}_\odot$, which we will refer to as "low-mass" and "high-mass" here. In Fig. 4.3 we show the abundance pattern produced by the best-fitting model from each of these branches. Both models seem to fit

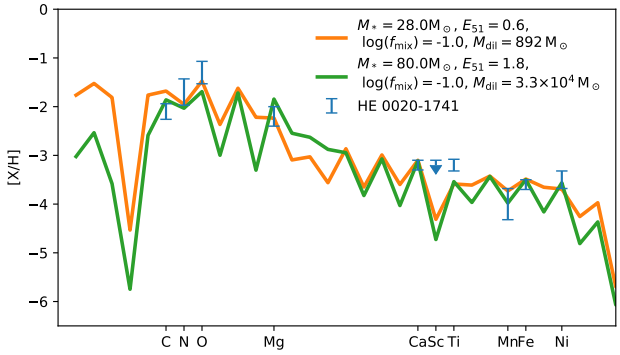

Figure 4.3: Best-fitting abundance patterns for HE 0020-1741. We show the observed pattern and the patterns of the best-fitting models with low-mass and high-mass progenitors. If only the abundance ratios are considered, both give an equally plausible fit, yet constraining the dilution rules out a single low-mass star as a progenitor. Sc is shown in grey to indicate that it is treated as an upper limit in the fits in order to account for the fact that theoretical models are known to under-predict Sc (Section 4.1.3). The fits shown are therefore not expected to match the observed value for Sc.

approximately equally well. However, if we consider only the constrained dilution case, only the high-mass progenitors still fit. The low-mass progenitors do not produce enough metals to explain the metal abundances of HE 0020-1741 with only a single SN. Thus, if HE 0020-1741 is to be explained with a single progenitor SN, it should be a massive star with $70\,M_\odot < M_* < 80\,M_\odot$ for the Heger & Woosley (2010) yields. Note, however, that it may be possible to find additional or better fits with different yield sets (e.g. Limongi & Chieffi, 2012, Ishigaki et al., 2018, Grimmett et al., 2018). However, as the aim here is to show the usefulness of the dilution limit to constrain fits, a comparison of these different yield set exceeds the scope of this thesis.

4.2.2 Example 2: Large sample fitting

Ishigaki et al. (2018) fitted the abundances of 201 EMP stars by picking the best-fitting SN model for each of these stars. The compiled sample of stars has been selected to consist only of stars with determined abundances for the elements C, N, O, Na, Mg, Al, Si, Ca, Sc, Ti, Cr, Mn, Fe, Co, Ni, and Zn based on spectroscopic data with a resolution of at least $R = 28000$. These observed abundances were compared to SN models which were computed over a grid of stellar masses, explosion energies as well as three parameters that quantify the properties of the mixing-and-fallback process. Details on the sample selection and the SN modelling can be found in

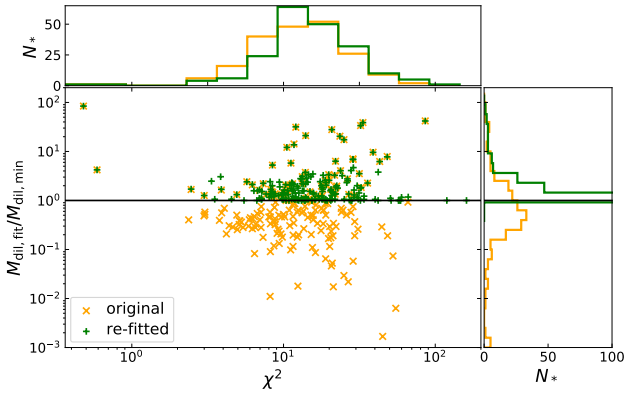

Figure 4.4: Ratio of the minimum dilution mass and the dilution mass derived in Ishigaki et al. (2018) as function of the reduced χ^2, as well as histograms of both values. We show the original fits from Ishigaki et al. (2018) (orange) as well as re-fits in which the minimum dilution limit is enforced (green). In some of the original fits, the dilution ratio is very low (down to $\sim 10^{-7}$) and therefore outside of the boundaries of this figure. These stars are included in the lowest bin of the histogram.

Ishigaki et al. (2018). For each star, they selected a best-fitting SN model through a χ^2 minimization, where the predicted abundance yields of each model in the grid was compared to the observed abundances. Using the explosion energy of these best-fitting models, we compute the corresponding dilution mass for each fitted star in their sample. In Fig. 4.4 we show the ratio between these minimum dilution masses and the dilution masses from the fits for all 201 stars. Of these 201 best-fitting models, 128 violate our derived limit and 43 do so by more than a factor of four. Notably there is no apparent correlation between χ^2 and the dilution mass. Thus, whether the dilution factor found by fitting is consistent with our limit is unrelated to the goodness of fit.

We have replicated the fitting procedure from Ishigaki et al. (2018), and added a criterion based on the dilution mass. In this approach, we reject all fits in which the dilution is inconsistent with the minimum dilution mass described in Eq. (4.2). This leads to a significant increase in the mean (median) χ^2 from 16 (13) in the unconstrained case to 24 (15) in the constrained case. For many stars, the best fit with the dilution constraint becomes worse than that without it. In Fig. 4.5 we show that this re-fitting leads to significant changes in the distribution of best-fitting progenitors masses. The most notable difference is that progenitors with a stellar mass of 25 and 40 $\mathrm{M}_\odot$ are now much rarer and progenitors with 15 $\mathrm{M}_\odot$ more common. The reason for this is that many of the previously common 25 and 40 $\mathrm{M}_\odot$ models

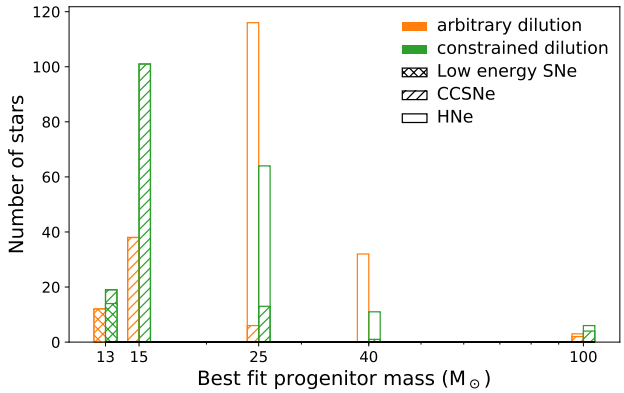

Figure 4.5: Distribution of progenitor masses from Ishigaki et al. (2018) as well as our repetition of the fits which take the minimum dilution criterion into account. There are only bins at 13, 15, 25, 40 and 100 $\mathrm{M}_\odot$ as these are the only progenitor masses of the SN models. We separate SNe by explosion energy into low-energy SNe ($E_{51} < 1$), CCSNe ($E_{51} = 1$) and hypernovae (HNe, $E_{51} \geq 10$).

were hypernovae (HNe) with a high explosion energy and a large fallback fraction. These stars have relatively low absolute yields, but due to their large explosion energies, we predict large dilution masses in spherical symmetry. Therefore, such models are not able to reproduce the relatively large carbon abundances of many CEMP-no stars, when taking the dilution constraint into account.

We note that the prescription of faint SNe used in Ishigaki et al. (2018) is chosen to reproduce the angle-averaged yields of aspherical jet SNe (Tominaga, 2009). Our dilution model, however, does not apply to such SNe if their asphericity is preserved. In the used prescription only the total yields are considered. Even if the abundance distribution in the ejecta is strongly aspherical, this approximation assumes that the SN yields are mixed and the angular variations are washed out during later phases of the expansion of the SN. In principle, the mixing behaviour in aspherical SNe can be very different from our approximation if the metal yield per unit energy shows strong angular variations. Additionally, aspherical SNe from Ishigaki et al. (2018) have systematically larger (and in some cases much larger) explosion energies, which are used in Equation (4.2), than their 2D counterparts with similar yields (Tominaga, 2009). This further limits the applicability of our model to these SNe. Our results here suggest that developing realistic models for the dilution of heavy elements produced in aspherical SNe is of vital importance for fitting large samples of stars, not just individual cases.

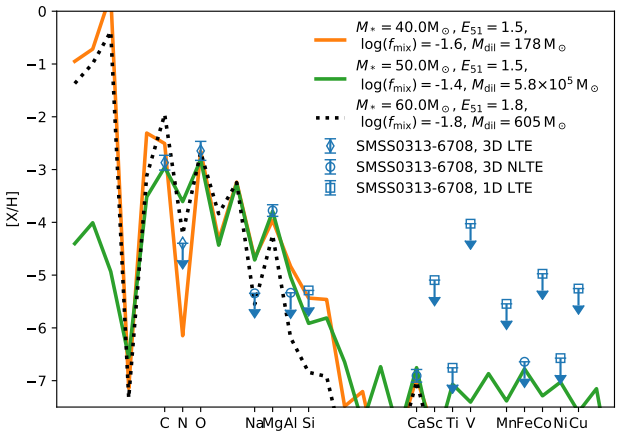

Figure 4.6: Best-fitting models for SMSS0313-6708. We show the unconstrained (orange) and the constrained (green) best-fitting model. We find the same best-fitting model as Bessell et al. (2015). For reference we also show the best-fitting model from Keller et al. (2014). We mark with different symbols whether abundances have been derived in 1D LTE (diamonds), 3D LTE (squares), or in 3D NLTE (circles). The upper limits shown here are at a 84 per cent confidence level, i.e., if the modelled value is at that the upper end of the error bar there is a discrepancy at a 84 per cent significance.

4.2.3 Example 3: No spherical progenitor for SMSS0313-6708

As we realized previously that stars with high carbon and low iron abundances are particularly strongly affected by applying the dilution criterion, we will look in more detail at a pathological example of such a star, i.e., SMSS0313-6708 (Keller et al., 2014). The star is known for having no detected iron abundance with an upper limit of $[\mathrm{Fe/H}] < -7.1$. We here use abundances that are based on 3D atmospheric models that do not assume local thermodynamical equilibrium (3D, NLTE) for Na, Mg, Al, Ca, and Fe from Nordlander et al. (2017). For these elements statistical and systematic errors are provided which we add with a quadratic sum. The systematic errors are typically on a level of 0.1 dex. The remaining abundances are taken from Bessell et al. (2015) and are based on 3D LTE models for C, N, and O and on 1D LTE models for Si, Sc, Ti, V, Cr, Mn, Co, Ni, and Cu. Notably, most of these elements are not detected and only upper limits on their abundance have been derived. Bessell et al. (2015) only give statistical but no systematical errors for their abundance determinations. Because we want to avoid biasing our results towards abundances with an unaccounted source of error, we add a systematical error of 0.1 dex to the abundance determinations from Bessell et al. (2015).

We fit the abundances with the same procedure as described in Sect. 4.2.1.

The best constrained and unconstrained models are shown in Fig. 4.6. The upper limits shown here are at a 84 per cent confidence level. This implies that a value 1σ above the upper limit corresponds to a 98 per cent significant discrepancy. Even with unconstrained dilution, we find no model that produces a convincing fit of the abundance patterns. The best-fitting model overproduces Na, C and Si. There are three features in the abundances that are difficult to fit simultaneously:

1. the CNO pattern with high C and O but very low N,
2. the low upper limit on Na with the detection of a large amount of Mg, and
3. the detection of Ca in conjunction with the low upper limits on Al and Si

The difficulty involved in reproducing all three of these features may partially be related to the grid of models not containing a sufficiently large variety of SN explosion energies. We note that none of the elemental abundances that have been derived in 1D LTE play a critical role in constraining the models. All 1D LTE abundances are only upper limits that lie well above the best-fitting models. It is still unclear how different the C and O abundances would be in a 3D NLTE analysis, but they would need to differ by approximately 1 dex from 3D LTE in order for us to be able to find SNe with matching abundances. Nordlander et al. (2017) were able to fit the abundance patterns by interpolating the abundance patterns as function of the explosion energy. However, the result of such a procedure is potentially sensitive to the way the interpolation is done. We therefore decided against interpolating to a finer grid here.

Both the unconstrained best-fitting model and the best-fitting model from Keller et al. (2014) violate the dilution limit by around two orders of magnitude. They would require the SN ejecta to be diluted with less than $500\,\mathrm{M}_\odot$ of pristine material. The best-fitting model that fulfils the dilution limit is clearly inconsistent with the observed upper limits of N and Na. In Ishigaki et al. (2014) this star was best-fitted with $25M_\odot$ and $40M_\odot$ SN or HNe (jet-induced, aspherical, and energetic SN), where Ca is produce by static/explosive O burning and incomplete Si burning in contrast to the explanation in Keller et al. (2014). Of these models, the SNe are consistent with our dilution limit and the HNe are neither compatible with the dilution criterion nor with the updated upper limit on Si that we use. The fits presented in Ishigaki et al. (2018) are compatible both with the abundance pattern we use and with our dilution limit. Chen et al. (2017a) model potential progenitor SNe for SMSS0313-6708 in one and two dimensions. Assuming our dilution limit equally applies to 2D

SNe, we find that only the two dimensional model of the SN of a $60\,M_\odot$ Pop III star is consistent with our dilution limit. As these elements are not modelled, however, it is unclear whether this model is able to reproduce the observed upper limits of the Na and Al abundances. Chan et al. (2020) performed full 3D SNe simulations of the progenitor of SMSS0313-6708 using a $40\,M_\odot$ star, as suggested by Bessell et al. (2015), with asymmetric explosion of low and high energy. Their nucleosynthesis has the same constraints as those by Chen et al. (2017a), and the explosion was not followed beyond shock breakout. The low-energy model does not produce any significant metals, the high-energy model too much iron – if spherically averaged.

4.3 Discussion and summary

It is common practice to fit observed stellar abundance by comparing them to modelled SN yields that have been diluted with a freely chosen dilution mass. We argue that this factor cannot be chosen freely, however, as SNe generally inject large amounts of energy into their surroundings and dilution mass must be large enough to contain the SN remnant until it recollapses. Therefore, we have introduced an analytical limit for the dilution of metals produced by a single SN with the following three assumptions:

- the SN being alone and isolated,
- the explosions being spherical and well-mixed, and
- the surrounding medium being homogeneous.

The first two assumptions are commonly made when comparing observed abundance patterns to SN yields in previous works, because if these are not fulfilled the total elemental yields from a single SN cannot be representative stellar abundance pattern. For the last assumption we compared this limit to all hydrodynamical simulations of metal enrichment in high-redshift minihaloes which we are aware of and which included the needed details and resolution for a comparison. We found that, despite assuming homogeneity, the limit is consistent with all of these simulations.

We demonstrate that previous fits were often inconsistent with our understanding of metal dilution and mixing on the scale of minihaloes. Including our dilution criterion into fitting procedures for abundance patterns can have important consequences for the conclusions drawn:

1. Considering the dilution can help to break degeneracies in progenitor models of individual stars.

2. The limit does not just affect individual stars but it can also change the properties of large samples of progenitor models. In particular, low-yield SNe are disfavoured if constraints on the dilution are taken into account.

3. It may be difficult to explain certain stars, such as SMSS0313-6708 by enrichment from a single, spherical SN if the dilution is taken into account. The best-fitting models that have been put forward by Keller et al. (2014) and Bessell et al. (2015) explain the rough shape of the observed abundance ratios, but with an implicit dilution mass that is too small by approximately two orders of magnitude, the yield from the SNe are too small to explain the absolute metal abundances. Ishigaki et al. (2014, 2018) find fits to the abundance pattern that are consistent with our dilution criterion.

During the preparation of this manuscript, Komiya et al. (2020) derived a similar estimate for the minimal dilution and implemented it into a semi-analytical model of the formation of the Milky Way. While we apply this estimate to the exploration of progenitor scenarios of individual stars, Komiya et al. (2020) focus on the chemical evolution of the Milky Way and in particular on whether the overall population of CEMP-no stars can be reproduced. They find it difficult to reproduce the prevalence of large carbon abundances in the lowest metallicity stars with faint SNe. This tension between the mixing-and-fallback SN model and the large observed carbon abundances is consistent with our findings.

A recent study by Ji et al. (2020) adds a dilution limit into their fitting procedure in a very similar way as we do here. This is done in the context of the observation of metal-poor stars in the ultra-faint dwarf galaxies Carina II and III. They find that applying the dilution limit moves their fit systematically to higher explosion energies and stellar masses. Ji et al. (2020) further point out that the dilution mass can be a helpful criterion in deciding whether the metals originate from the galaxy itself or from external enrichment.

The minimum dilution estimate can serve for evaluating whether a single, spherical SN is a viable progenitor scenario for a certain star. This test may be less reliable, if applicable at all, for asymmetric SNe or cases with several SNe in one halo. In asymmetric SNe, a large fraction of the metals can be ejected along jets (Tominaga, 2009). Evidence for such SNe has recently been found by Ezzeddine

et al. (2019). The dilution and recollapse occurring after such SNe are yet to be explored by numerical simulations.

Altogether, we conclude that for the adequate astrophysical interpretation of the observed elemental abundances in extremely metal-poor stars, both the relative abundance patterns as well as the absolute abundance values need to be taken into account. Only then reliable and well founded constraints on the properties of the preceding generation of stars can be derived. Given the fact that simple spherically symmetric models often fail to match the dilutions mass constraint introduced here, we furthermore conclude that the effects of aspherical SNe, the impact of inhomogeneous mixing in a highly structured interstellar medium, and the combined yields of multiple SNe requires further investigation.

4.4 Metallicity dependence of the minimum dilution mass

In our derivation of the minimum dilution mass we used the common description for the expansion of SN remnants in the solar metallicity case. In nature, however, the situation is more complicated. The metallicity within the SN remnant is expected to be considerably lower than solar metallicity. The exact value will depend on the yields of the SN and will evolve as the remnant expands. Lower metallicities mean less efficient cooling and therefore a longer Sedov-Taylor phase. Consequently, the final mass enclosed within the stalling radius will be larger at sub-solar metallicity than at solar metallicity. Adopting the solar metallicity result therefore gives us a conservative lower limit on the minimum mixing mass. Nevertheless, it is useful to estimate how large the effect of this assumption is by comparing the solar metallicity result with the analogous result in the limit of zero metallicity.

To estimate the time at which the SN remnant leaves the Sedov-Taylor phase, we follow the procedure outlined in Draine (2011, Chapter 39.1.2). We calculate the radiative cooling rate of the remnant by integrating the cooling function Λ over the volume of the remnant:

$$\frac{\mathrm{d}E}{\mathrm{d}t} = -\int_0^{R_\mathrm{s}} 4\pi r^2 \Lambda_0 \,\mathrm{d}r. \tag{4.10}$$

For metal-free gas, we can approximate the cooling rate as

$$\Lambda_0 = C\, n_\mathrm{H}^2 T_6^{-1.2} \tag{4.11}$$

where T_6 is the temperature in units of $10^6\,\mathrm{K}$, n_H is the hydrogen number density and $C = 4.5 \times 10^{-24}\,\mathrm{erg\,s^{-1}\,cm^3}$. This simple power-law fit is a good approximation

of the zero-metallicity cooling rate in the temperature range $0.1 < T_6 < 1.0$ and under-estimates it at higher temperatures (e.g., Figure 34.2 of Draine 2011). The energy loss rate of the remnant therefore becomes

$$\frac{\mathrm{d}E}{\mathrm{d}t} = -1.2\frac{4\pi}{3}\, {R_\mathrm{s}}^3\, C\, n_\mathrm{H0}^2 T_\mathrm{s6}^{-1.2} \left\langle \left(\frac{\rho}{\rho_0}\right)^2 \left(\frac{T}{T_\mathrm{s}}\right)^{-1.2} \right\rangle, \tag{4.12}$$

where R_s is the radius of the SN remnant and ρ is the mass density. Variables subscripted with s refer to values just inside the blast-wave and variables subscribed with 0 refer to quantities in the ambient medium. The $\langle ....\rangle$ brackets denote a volume-weighted average over the blastwave. While the energy loss is small, we can use the density and temperature profiles from the Sedov-Taylor solution for a constant density ambient medium, and $\langle(\rho/\rho_0)^2(T_\mathrm{s}/T)^{1.2}\rangle = 1.674$. The total energy loss can be computed by integrating the energy loss rate:

$$\Delta E = -1.2 \times \frac{4\pi}{3} \times 1.674\, n_\mathrm{H0}^2 C \int {R_\mathrm{s}}^3 T_\mathrm{s6}^{-1.2}\, \mathrm{d}t. \tag{4.13}$$

The values of the blast-wave radius and the temperature just behind the shock front are given as a function of time by the Sedov-Taylor solution:

$$\begin{aligned} R_s &= 1.54 \times 10^{19}\,\mathrm{cm}\, E_{51}^{1/5} n_\mathrm{H0}^{-1/5} t_3^{2/5} \\ T_\mathrm{s6} &= 52.5\, E_{51}^{2/5} n_\mathrm{H0}^{-2/5} t_3^{-6/5}, \end{aligned} \tag{4.14}$$

where t_3 is the time since the explosion in units of 1000 yr. Therefore we can simplify Eq. (4.13) to

$$\begin{aligned} \Delta E &= -\,3.76 \times 10^{43}\,\mathrm{erg\,s^{-1}}\, E_{51}^{0.12} n_\mathrm{H0}^{1.88} \int_0^{t_3} {t'_3}^{2.64}\, \mathrm{d}t'_3 \\ &= -\,1.03 \times 10^{43}\,\mathrm{erg\,s^{-1}}\, E_{51}^{0.12} n_\mathrm{H0}^{1.88} t_3^{3.64} \end{aligned} \tag{4.15}$$

Finally, if we follow Draine (2011) and assume that the remnant leaves the Sedov-Taylor phase when $\Delta E/E = -1/3$, we can compute the time t_rad at which the Sedov-Taylor phase ends.

$$t_\mathrm{rad} = 115 \times 10^3\,\mathrm{yr}\, E_{51}^{0.24} n_\mathrm{H0}^{-0.52}. \tag{4.16}$$

For comparison, the calculation given by Draine (2011) for the solar metallicity case

yields

$$t_{\rm rad} = 49 \times 10^3 \,{\rm yr}\, E_{51}^{0.22} n_{\rm H0}^{-0.55}. \tag{4.17}$$

Therefore, despite the much smaller volumetric cooling rate in the zero metallicity case, the cooling time of the remnant only changes by a factor of about two, thanks to the strong time dependence of the total energy loss rate of the remnant. We can also consider the dependence of the dilution mass on the time at which the Sedov-Taylor phase ends. The fade-away radius is

$$R_{\rm fade} = R_{\rm rad} \left(\frac{t_{\rm fade}}{t_{\rm rad}} \right)^{2/7}, \tag{4.18}$$

where

$$t_{\rm fade} = \left(\frac{2R_{\rm rad}}{7 t_{\rm rad} c_{\rm s}} \right)^{7/5} t_{\rm rad}, \tag{4.19}$$

and where $c_{\rm s}$ is the ambient medium speed of sound. The radius at the end of the Sedov-Taylor phase can be obtained as $R_{\rm rad} = R_{\rm s}(t_{\rm rad}) \propto t_{\rm rad}^{2/5}$. This leads to

$$\begin{aligned} R_{\rm fade} &= R_{\rm rad} \left(\frac{t_{\rm fade}}{t_{\rm rad}} \right)^{2/7} \\ &\propto R_{\rm rad} \left(\frac{R_{\rm rad}}{t_{\rm rad}} \right)^{2/5} \\ &\propto R_{\rm rad}^{7/5} t_{\rm rad}^{-2/5} \propto t_{\rm rad}^{4/25}. \end{aligned} \tag{4.20}$$

Since $M_{\rm dil} \propto R_{\rm fade}^3$, the dilution mass is related to the duration of the Sedov-Taylor phase via

$$M_{\rm dil} \propto t_{\rm rad}^{12/25}. \tag{4.21}$$

Therefore the reduction of the cooling rate in zero metallicity gas would increase the minimum dilution mass by around 50 per-cent. All simulations presented in Section 4.1.2 are consistent with this limit too. As the metallicity of the SN remnant depends on the SN yields, we use the more conservative solar metallicity value for the dilution mass in this chapter.

5

Metal mixing in minihalos: the descendants of pair-instability supernovae

Published as Magg et al. (2021a)

The lack of observations of abundance patterns originating in pair-instability SNe has been a long-standing problem in relation to the first stars. This class of SNe is expected to have an abundance pattern with a strong odd-even effect, making it substantially different from present-day SNe. In this chapter, we use a cosmological radiation hydrodynamics simulation to model such SNe and the subsequent formation of the second generation of stars. We incorporate streaming velocities for the first time. There are 14 star-forming minihalos in our $1\,\mathrm{cMpc}\,h^{-1}$ box, leading to 14 SNe occurring before redshift $z = 19.5$, where we start reducing the complexity of the simulation. Following the explosions, EMP stars form in 10 halos via internal and external enrichment, which makes it the most common outcome. Only one halo does not recollapse during the simulations. This result is at tension with the current (lack of) observations of metal-poor stars with pair instability SN abundance patterns, suggesting that these very massive stars might be rare even in the early Universe. The results from this simulation also give us insights into what drives different modes of recollapse and what determines the mixing behavior of metals after very energetic SNe.

Disclaimer

This chapter was accepted for publication in the Astrophysical Journal as Magg et al. (2021a). The text has been primarily written by me but in collaboration with all listed coauthors. The simulation methods were developed in collaboration with Robin Treß, Anna Schauer, and Ondrej Jaura and are based on the works cited in Section 5.1. The ideas behind this work, figures found in this chapter as well as the code used for analysis are my work and have been developed with feedback from all collaborators.

5.1 Methods

5.1.1 Overview

In order to model PISNe in an appropriate environment, a complex multi-physics simulation setup is necessary. We need to self-consistently treat the formation of the first stars in minihalos in a cosmological context, the radiative feedback which shapes the environment in which the SNe explode, the SNe themselves and then we need to follow the metals until a second generation of stars forms.

Previous simulations of this type have focused on one single or a few selected halos (e.g. Greif et al., 2010, Jeon et al., 2014, Ritter et al., 2015, Smith et al., 2015, Chiaki et al., 2018). They model the formation of one or a few stars of a pre-selected mass in one or up to three (in Chiaki et al., 2018) minihalos, and include the effects of radiative feedback, SNe and the formation of the first enriched stars. As the resulting mixing processes in these studies show large variations, it is necessary to simulate a large region that includes a statistically significant sample of halos to gain a more complete picture of the variations in outcomes. Additionally, in order to observe the recollapse of the halos, the simulation needs to be run for an extended time-period. For example, Latif & Schleicher (2020) simulate PISNe in five different halos and find that only the two most massive halos ($M_{\rm vir} > 10^7\,{\rm M}_\odot$) form stars again within 31 Myr after the SNe, demonstrating that in order to determine the ultimate fate of the gas enriched by PISNe, we need to follow its evolution for tens of Myr.

5.1.2 Setup and initial conditions

In order to have as many star-forming halos as possible for this thesis, we simulate the largest box we can afford at the resolution required to properly resolve gas

cooling and star formation (see Section 5.1.7) in minihalos. We use a periodic cosmological box with an edge-length of $1\,\mathrm{Mpc}\,h^{-1}$. The simulation is initialized at $z = 200$ and the initial conditions are created with MUSIC (Hahn & Abel, 2011). We use cosmological parameters from Planck Collaboration et al. (2016a) which are $\Omega_\mathrm{b} = 0.04864$, $\Omega_\mathrm{m} = 0.3089$, $\Omega_\Lambda = 0.6911$, $\sigma_8 = 0.8159$, $n_\mathrm{s} = 0.961$ and $H_0 = h\,100\mathrm{km\,s^{-1}\,Mpc^{-1}}$ with $h = 0.6774$. We generate 512^3 dark matter particles and equally many gas cells, giving us a resolution of approximately $800\,\mathrm{M}_\odot$ for the dark matter particles and an initial mass of $150\,\mathrm{M}_\odot$ for the gas cells. Arepo ensures that the gas cell masses remain within a factor of two of this initial mass at later times, unless one of the resolution criteria described in Section 5.1.7 applies. Taking the refinement into account, a typical star forming minihalo (of around $10^6\,\mathrm{M}_\odot$) consists of 1300 dark matter particles and 5×10^5 gas cells, reaching a mass resolution down to $0.01\,\mathrm{M}_\odot$ in the highest density gas. The simulation presented first in this chapter used 3 million core-hours on SuperMucNG at the Leibnitz Computing Centre (LRZ) in Garching.

We approximate the effects of supersonic baryonic streaming (Tseliakhovich & Hirata, 2010) by adding a velocity offset of $4.9\,\mathrm{km\,s^{-1}}$ in the positive x-direction to the baryons in our initial conditions. This value corresponds to 0.8 times the root-mean-square streaming velocity and therefore represents the most likely value (Schauer et al., 2019b). Fully accounting for the effects of supersonic baryon streaming would require changing the density distribution in our initial conditions. However, these effects are only of secondary importance for simulations like ours (Park et al., 2020).

In order to speed up the simulation we deactivate the radiative transfer and Pop III SNe at $z = 19.5$, after the first 14 Pop III SNe exploded. This is shortly before the first metal-enriched star forms, and as our simulations do not yet have the capability to appropriately model Pop II stars or identify them at run-time, we would start spending substantial computational resources on modelling these stars as if they were metal-free. The shut-off occurs long before large-scale reionization is expected to affect the simulations notably. Reducing the complexity of the simulation at this point allows us to run the simulation for an extended period and capture more recollapsing halos. Modelling the entire period with full physics would require an implementation of metal-enriched star formation and low-metallicity chemistry, both of which are beyond the scope of this project.

We generate snapshots of the simulation every $\Delta z = 0.5$, starting at $z = 25$. This corresponds to a time difference between snapshots ranging from 4 Myr at $z = 25$ to

15 Myr at $z = 14$. In order to capture the formation of the second generation stars, we additionally take snapshots at the next full-hydro step[1] after each sink particle (see Section 5.1.4) forms and at the last full-hydro step before each SN.

5.1.3 Simulation framework

Our basic setup derives from the cosmological simulations performed by Schauer et al. (2019a, 2021) and is adapted as necessary for our simulation. We model the formation of the first stars, the explosion of the most massive of these stars as SNe and the formation of the second generation of stars with the moving mesh code arepo (Springel, 2010). We include the improved integration schemes from Pakmor et al. (2016) and the improved mesh regularization from Mocz et al. (2015). Chemistry and cooling of the gas are modelled with the same treatment as in Schauer et al. (2019a). We follow the non-equilibrium chemistry of H, D, He, H_2, HD and their corresponding ions by using the primordial chemistry network from Glover & Abel (2008), including updates introduced by Glover (2015). The effects of metal cooling are not included, as it is not relevant at low metallicity at the densities we reach in our simulation (Jappsen et al., 2007, Smith et al., 2015, Chiaki et al., 2016).

5.1.4 Star formation and sink particles

To model the formation of stars, we use an approach based on sink particles that was introduced in Tress et al. (2020). Sink particles are collisionless particles which are able to absorb gas that is gravtationally unstable and collapsing onto the particle. They are used to represent gravitationally collapsing regions as resolving and simulating such regions in numerical simulations is extremely expensive (see e.g. Bate et al., 1995, Federrath et al., 2010, Greif et al., 2011a). The formation of sink particles depends on a density threshold and the radius of the region from which a sink particle can be formed, the so-called sink-formation radius. A cell is turned into a sink particle if all of the following criteria are fulfilled:

- the density in the cell is larger than the density threshold;
- there are no additional sink particles within one sink-formation radius;

[1] To satisfy the Courant-Friedrichs-Levi condition (Courant et al., 1928), smaller cells need to be simulated on smaller time-steps. In order to not waste computational resources, Arepo uses an adaptive time-stepping scheme, in which small cells are simulated on smaller time-steps than larger cells. The largest time-step, i.e., a time-step in which all simulated cells are evolved, is referred to as "full-hydro step"

- the cell is at a local potential minimum;
- the gas within one sink-formation radius around the cell is converging ($\vec{\nabla} \cdot \vec{v} < 0$) and collapsing ($\vec{\nabla} \cdot \vec{a} < 0$);
- the sphere of gas around the cell (again, with a size of one sink-formation radius) is gravitationally bound, i.e., its potential energy is larger than twice the sum of its kinetic and thermal energy.

We note that the latter criterion is especially important. When it is deactivated, we see many sink particles forming in the strong shocks produced by the SNe, which is a numerical artifact, as this shocked gas is not actually gravitationally unstable.

After they have formed, sink particles can accrete gas. In order for gas to be accreted from a grid cell, the density must be above the threshold density and the cell must be located within the sink-formation radius of the sink. In addition, the gas must be gravitationally bound to the sink particle and collapsing onto it. Once a cell is marked as accreting, gas is removed from it until it reaches the threshold density. The gas mass removed from a cell during a single time-step is additionally limited to 90 per-cent of the cells initial mass. The gas removed from the cell is added to the sink particle, and the momentum of both cell and sink particle are updated as appropriate in order to ensure momentum conservation. "Skimming" the mass from the cells in this way helps to avoid grid construction problems and other numerical artifacts that can occur if the entire cell is accreted.

These methods were originally developed for simulations of the present-day Universe and we have adapted them to be compatible with the comoving internal unit-system of AREPO. The density threshold for sink particle formation in the simulations presented here is $10^4\,\mathrm{cm}^{-3}$. We chose this value for two reasons. Firstly, primordial gas is expected to become Jeans-unstable at these densities (Yoshida et al., 2006, Greif et al., 2011a), and therefore we can be confident that it begins to collapse at this density and will end up forming stars. Secondly, we do not model how the metals injected by the first SNe affect the chemistry and cooling. At the metallicities encountered in our simulation, metal-induced fragmentation is expected to only occur at number densities higher than around $10^4\,\mathrm{cm}^{-3}$ (Smith et al., 2015, Chiaki et al., 2015), and so our simulation will not be affected by our neglect of metal cooling and chemistry. Densities higher than this should be considered unresolved in our simulation and further refinement (see Section 5.1.7) is deactivated above this threshold. The sink-formation radius is chosen such that the

mass within a sphere with a mean density equal to the threshold density is exactly one Jeans mass at a temperature of $T = 200\,\mathrm{K}$, which is a typical temperature for the point at which primordial gas becomes Jeans unstable (Yoshida et al., 2006). In practice, this corresponds to a sink-formation radius of 2 pc.

As we are focusing exclusively on PISNe, we assign a single star with a fixed mass of $200\,\mathrm{M}_\odot$ to each newly forming sink particle. We note that stars are only assigned to the sink-particle for the modelling of stellar feedback. The gravitational mass of the sink-particle is not altered by this choice. For future studies, we plan to adapt the star formation recipe based on Poisson sampling introduced in Sormani et al. (2017) to the case of a Pop III IMF, but we do not use this in our present work.

5.1.5 Radiative transfer

We use the SIMPLEX-based (Kruip et al., 2010, Paardekooper et al., 2010) radiative transfer code SPRAI (Jaura et al., 2018, 2020) to model the radiative feedback of the stars. Radiation is modelled in four energy bands ranging from 11.2 eV to 136 eV, which are detailed in Table 5.1. The photon emission rates in these bands are calculated assuming that the Pop III stars radiate as black bodies, with an effective stellar temperature and radius obtained by interpolation of the data in Schaerer (2002). We compute the average cross-section for each modelled photochemical process in each energy band by weighting the frequency-dependent cross-sections by a black-body spectrum of temperature $T = 80000\,\mathrm{K}$, as described in more detail in Baczynski et al. (2015) and Jaura et al. (2018). We model the non-equilibrium radiation-chemistry, the corresponding heating and the radiation pressure exerted by the absorbed photons. Because SPRAI can only run on the largest time-steps within the adaptive time-stepping of AREPO, we limit the maximum time-step to be around 10000 years at redshifts below $z = 25$, i.e., when the first stars form in our simulation. The life-times of the stars are assigned as interpolated values from Schaerer (2002), which results in a life-time of 2.2 Myr for a $200\,\mathrm{M}_\odot$ Pop III star.

5.1.6 Supernovae

At the end of each star's life, the SN explosion energy is injected as thermal energy into the closest 1000 cells, as in Tress et al. (2020). The process is again adapted to the internal cosmological unit system of AREPO. We ensure that the Sedov-Taylor phase of each SNe is accurately captured (see Section 5.1.7), and therefore we do not

Energy (eV)	Processes	$\sigma\,(10^{-18}\,\mathrm{cm}^2)$	$\dot{N}(10^{48}\mathrm{s}^{-1})$
11.2–13.6	H_2 dissociation	2.47	9.15
13.6–15.2	H_2 dissociation	2.47	6.15
	H ionization	5.35	
15.2–24.6	H_2 ionization	6.52	32.4
	H ionization	2.39	
24.6–136	H_2 ionization	1.85	47.5
	H ionization	0.51	
	He ionization	4.65	

Table 5.1: Summary of radiation energy bins. The columns are: (1) Energy bin, (2) Modelled photo-chemical processes, (3) reaction crossection for the processes, and (4) photon emission rate of a single 200 $\mathrm{M}_\odot$ star in the energy bin.

need to make use of a momentum injection scheme (e.g. Gatto et al., 2015). Each SN explodes as a very energetic PISN (Heger & Woosley, 2002) with an explosion energy of $E_{\mathrm{SN}} = 100\,\mathrm{foe}$. In addition to the energy, we also inject 10^7 Monte-Carlo tracer particles (Genel et al., 2013) into each SN. We take these tracer particles to represent the metals injected into the SN. They are used to follow the enrichment and to determine the metallicity of the second generation of stars.

5.1.7 Resolution and refinement

The variety of physical processes modelled in our simulation translates to a set of resolution criteria. Specifically we need to resolve:

1. the formation and substructure of minihalos,
2. the gravitational collapse and fragmentation of molecular clouds,
3. the expansion of ionized regions around massive stars,
4. the expansion of SN remnants.

This translates into the following resolution criteria:

1. The dark matter particle mass needs to be well below the halo mass. Schauer et al. (2019a) demonstrated that at least 1000 dark matter particles are required to consider a halo resolved. We therefore require a dark matter particle

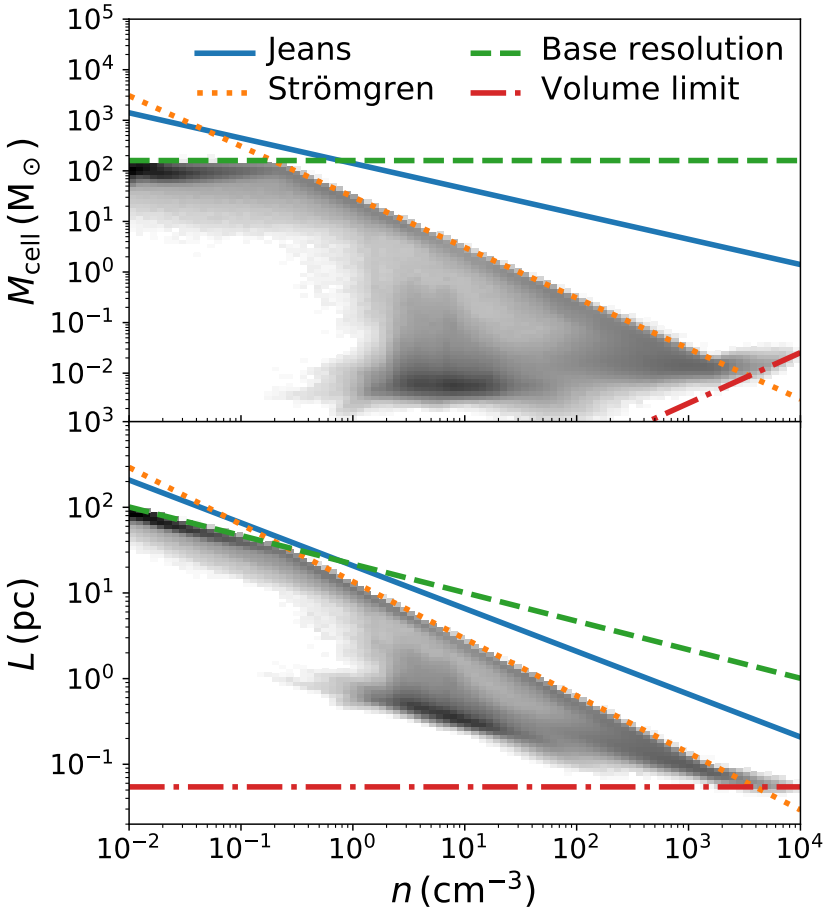

Figure 5.1: Comparison between the resolution criteria to resolve fragmentation (Jeans criterion, blue, solid) and to resolve photoionization (Strömgren criterion, orange, dotted), the initial gas particle mass (dashed, green), and the volume limit (dashed-dotted, red) as function of the nucleon number density. In the background, we show the distribution of cell sizes and masses in our simulation, when the first star forms. The resolution is expressed both as mass (upper panel) and as linear size (lower panel).

mass of no more than $1000\,\mathrm{M}_\odot$ in order to resolve a $10^6\,\mathrm{M}_\odot$ minihalo. We fulfil this criterion with our dark matter particle mass of $800\,\mathrm{M}_\odot$.

2. In order to find numerically converged fragmentation behavior, the Jeans length has to be resolved with several resolution elements (Truelove et al., 1997). We therefore require that the Jeans length is always resolved with at least 8 cells, leading to a maximum cell mass of

$$M_{\mathrm{c,Jeans}} = \frac{1}{8^3}\frac{\pi^{5/2}}{6}\frac{c_\mathrm{s}^3}{G^{3/2}\rho^{1/2}}, \tag{5.1}$$

where c_s is the speed of sound of the gas, ρ is the mass density and G is the gravitational constant. At the sink-formation threshold, for a typical gas temperature of 200 K the Jeans mass is $M_{\mathrm{Jeans}} \approx 2000\,\mathrm{M}_\odot$ leading to a maximum cell mass of $M_{\mathrm{c,Jeans}} \approx 4\,\mathrm{M}_\odot$.

3. In order to accurately capture the expansion of the HII regions around massive stars, it is necessary to resolve the initial Strömgren sphere, which then proceeds to expand as a D-type ionization front. The size of this region is given by the Strömgren radius R_{Str} (Strömgren, 1939). We have chose to resolve the Strömgren sphere with at least 1000 cells, corresponding to approximately six cells per Strömgren radius. This consideration leads to a resolution criterion which we can write as

$$M_{\mathrm{c,Str}} = \frac{1}{1000}\frac{4}{3}\pi\rho R_{\mathrm{Str}}^3, \tag{5.2}$$

which is equivalent to

$$M_{\mathrm{c,Str}} = 4\times10^{-4}\,\mathrm{M}_\odot\left(\frac{n}{10^4\,\mathrm{cm}^{-3}}\right)^{-1}\left(\frac{\dot{N}_{\mathrm{ion}}}{10^{48}\,\mathrm{s}^{-1}}\right), \tag{5.3}$$

where $\dot{N}_{\mathrm{ion}}$ is the ionizing photon emission rate and n is the nucleon number density.

4. Additionally we limit the maximum cell size within 10 pc of the nearest sink particle to be no more than 0.15 pc in diameter. This helps to better capture the behavior of low-density gas around the sink particles and ensures that the injection region for the SN energy is smaller than the Sedov-Taylor radius,

which is

$$R_{\rm SD} = 24\,{\rm pc}\,n^{-0.42}E_{51}^{0.29}, \tag{5.4}$$

where E_{51} is the explosion energy in units of 10^{51} erg. At our star formation threshold, i.e., at number densities of $n = 10^4\,{\rm cm}^{-3}$, the Sedov-Taylor radius is $R_{\rm SD} \approx 2\,{\rm pc}$.

5. The size of the cells is limited at a minimum comoving volume of $0.1\,{\rm pc}^3\,h^{-3}$.

The refinement criteria dictated by the Jeans length and the Strömgren radius as a function of number density are shown in Fig.5.1. For this example we use an ionizing photon emission rate of $\dot{N}_{\rm ion} = 4.0 \times 10^{49}\,{\rm s}^{-1}$, which is appropriate for the $200\,{\rm M}_\odot$ stars that we model, and a gas temperature of $T = 10000\,{\rm K}$ in the HII region. It is worth noting that, despite the large ionizing radiation output, at number densities above $n = 0.1\,{\rm cm}^{-3}$ the Strömgren criterion is more strict that the Jeans criterion. As the Strömgren criterion scales more steeply with density than the Jeans criterion, this will always be the case at sufficiently high densities. An unresolved ionized region leads to an over-cooling problem, similar to the over-cooling problem in unresolved SNe. Because the ionized region is not resolved, instead of a small fully ionized region we find a larger only slightly ionized region. The temperature and the thermal pressure of this region is underestimated. This slows or completely stops the expansion of the HII region.

5.2 Results

5.2.1 Qualitative description

Before the first metal-enriched star appears, we see Pop III stars forming in 14 different halos, distributed throughout the simulation volume starting at $z \approx 24$. We number these halos in order of appearance and summarize their property in Table 5.2. We show projections of the entire simulation box at various stages in Figure 5.2 and the centers of four selected halos in Fig. 5.3, two with long (halos 1 and 2) and two short (halos 8 and 13) recovery times. Images of the remaining halos can be found in Appendix 5.5. The radiation from the massive stars quickly photoevaporates the gas in their environment and drastically reduces the ambient density before they explode, similar to the behavior seen in previous simulations of radiative feedback from Pop III stars (see e.g. Whalen et al., 2004, Wise & Abel, 2008). While we allow multiple sinks, and hence multiple massive stars, to form in

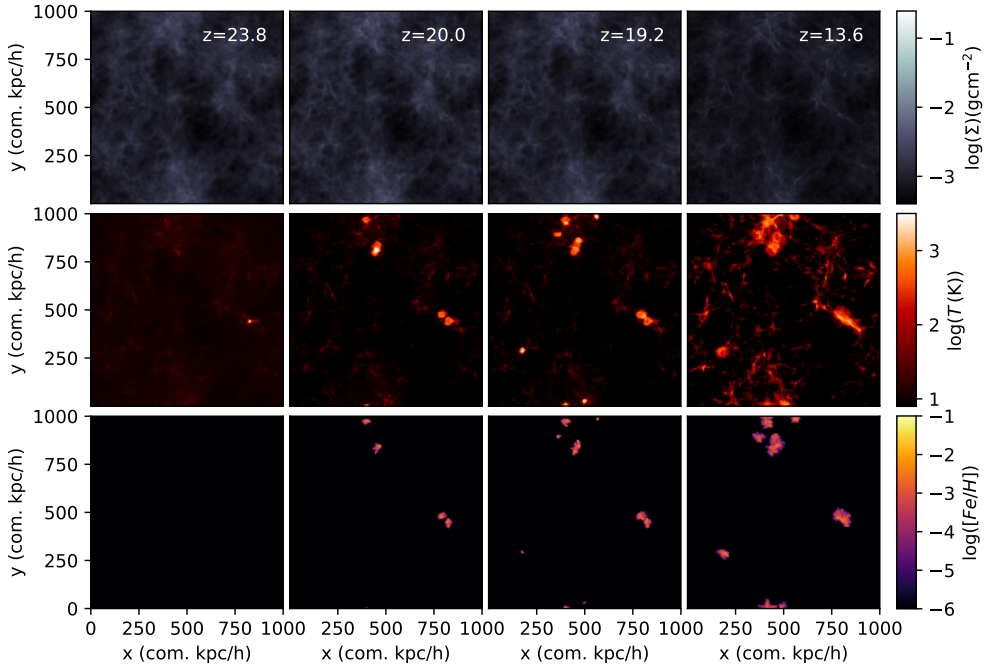

Figure 5.2: Column density (top row), temperature (middle row), and metallicity (bottom row) projections of the entire simulation at four different redshifts. The metallicities and temperatures are mass weighted averages along the column. Note that the third snapshot in this figure is the last time at which the radiative transfer is fully active (see text).

each halo, in practice the radiative feedback is so strong that this does not occur.

After the explosions we observe the formation of second-generation stars in three different modes: fast recollapse, slow recollapse and external enrichment. External enrichment implies that metal-enriched stars form in a halo that has never experienced metal-free star formation, i.e., that the metals come from outside the star-forming halo. Recollapse or internal enrichment refers to metal-enriched stars forming in halos that previously experienced metal-free star formation. Later, we will see that this appears to occur in two distinctly different modes, either relatively quickly after the SNe or after an extended time-period. We refer to these modes as fast and slow recollapse.

Only one of our halos (halo 4, seen in Figures 5.12 and 5.14) does not recollapse during the 135 Myr we simulate after the last SN. We observe 9 cases of internal and 8 cases of external enrichment. There is a discrepancy between the number of recollapses and the number of internal enrichments because four of the simulated halos merge with an externally enriched halo before forming the first internally

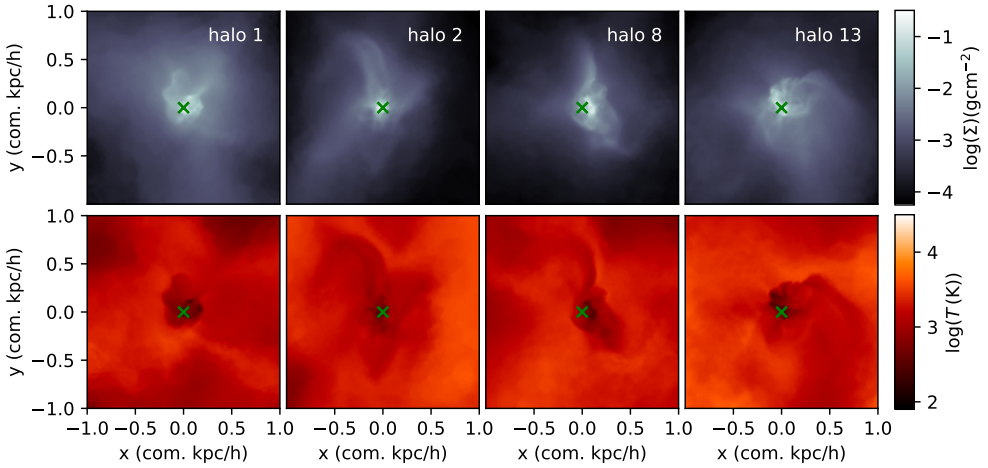

Figure 5.3: Column density (upper row) and mass-weighted average temperature (lower row) at the onset of star formation in 4 selected halos. The individual projections are projections of a 2 kpc h^{-1} cubes, centered on the sink particles, which are indicated with green crosses. Similar images for the remaining halos are found in Figures 5.12 and 5.13. The halos we selected are two halos with short (halos 8 and 13) and two halos with long (halos 1 and 2) recovery times. The properties of all halos are summarized in Table 5.2.

enriched stars. These halos are therefore counted as recollapsed but, as the stars they form would be affected by the accreted second-generation stars, there is no formation of second generation stars in situ in these halos. The median recovery time (frequently also referred to as fall-back time or recollapse time, i.e., the time between the first SN and the formation of second generation stars within the halo) is 50 Myr.

5.2.2 Evolution of halo masses

As halo finders usually struggle with the high resolution of the gas in the centers of our halos, we determine halo masses only on the basis of their dark matter content. We use ROCKSTAR (Behroozi et al., 2013a) to find halos in all snapshots and multiply the resulting halo masses with $\Omega_m/(\Omega_m - \Omega_b)$ to account for the baryons we excluded from the determination of the mass. Results from Schauer et al. (2019b) indicate that, given our streaming velocity, the baryonic gas mass can be lower than our estimate by a factor of two. However, our aim is to trace the underlying growth of the halos to find a connection between that growth history and the progression of early star formation, rather than, e.g., to quantify the effects of feedback on the baryon content of the halos. Therefore, and since baryons are only a secondary

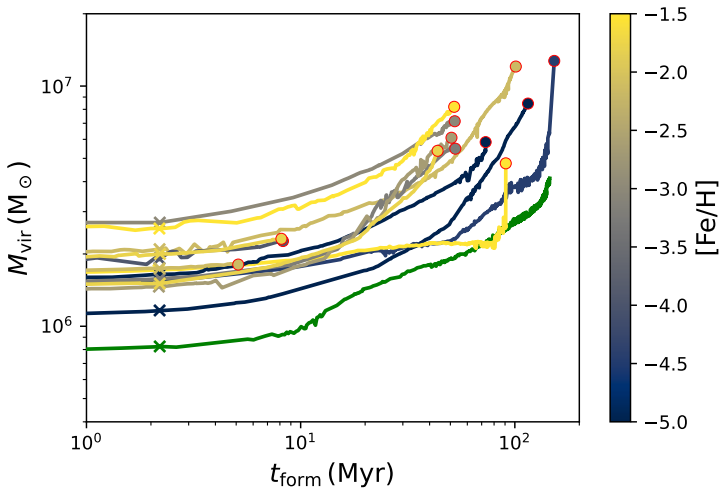

Figure 5.4: Growth history of the 14 halos that host Pop III stars as a function of time since the formation of the sink particle. The halos are color-coded by the metallicity of the second generation stars that form in them. The green line is the halo that does not recollapse (halo 4). The crosses shows the halos shortly before the SNe and the circles show the time at which the first metal-enriched star forms in each halo.

contribution to the overall mass of the halos, our assumption is appropriate for this analysis.

We show the growth history of the 14 host halos until their recollapse in Fig. 5.4. The fitting function for critical halo-mass given by Schauer et al. (2021, their Eq. 9 & 10) indicates that for our setup, i.e., streaming velocities of $v_{\rm bc} = 0.8\,\sigma$ and no global LW background, halos should start forming stars at $M_{\rm crit} \approx 2 \times 10^6\,{\rm M}_\odot$. We find a mean virial mass at star-formation of $M_{\rm mean,vir} = 1.7 \times 10^6\,{\rm M}_\odot$ which is consistent with this previous results. As the fitting formula from Schauer et al. (2021) was obtained with higher resolution, this consistency shows that our resolution is sufficient to capture the collapse of the minihalos without artificial delays caused by low resolution.

There is no simple relationship between halo mass and fallback time or metallicity, indicating that mixing and fallback are stochastic processes. We will discuss the metallicities in more detail in Section 5.2.4. The halo that does not fall back seems to have a relatively low mass, and exhibits slow growth. Three of the halos fall back in less than 10 Myr, yet this behavior does not correspond to the highest halo masses or particularly fast halo growth. The halos that fall back after a longer time usually at least triple in mass before falling back. The least massive halo does not fall back during our simulation. The complexity of this picture demonstrates the need for

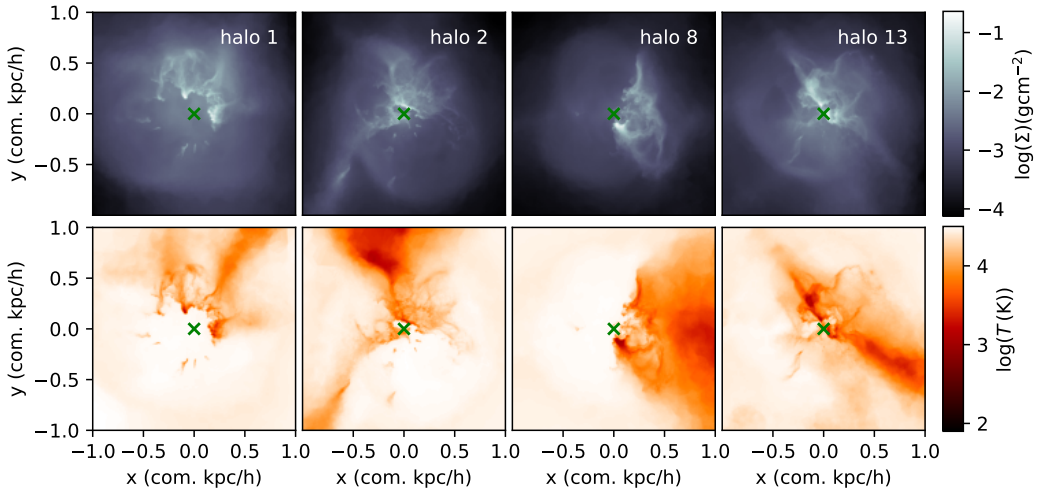

Figure 5.5: Column density (upper row) and mass-weighted average temperature (lower row) shortly before the SNe in 4 selected halos shown in Figure 5.3. The green crosses indicate the position of the Pop III stars that are about to explode. We can see that, while being mostly ionized, the halos retain small, dense clumps and shadowed cool regions behind them. Similar images for the remaining halos can be found in Figures 5.14 and 5.15.

simulating these processes in a statistical sample, rather than only simulating one example of a halo of a certain mass.

5.2.3 Pre-SN environment

We show the four selected halos shortly before their SNe in Fig 5.5. Halo 1 has the least homogeneous mixing among the internally enriched halos. This can be seen in Table 5.2, as this halo has the largest difference between local metallicity in the star forming region and the total metallicity of the halo. We can see that the halos are mostly photoionized, hot and photoevaporated. However, there are localized dense clumps that are relatively cold, and cool, shadowed regions behind these clumps. We note that not all halos exhibit an equal degree of clumpiness. Halo 4, which does not recollapse during our simulation, has only very little dense gas left before the SN (see Fig. 5.14).

In Fig. 5.6, we examine whether there is a correlation between the presence of clumps shortly before the SN and the fall-back time. For this purpose we define dense gas as having a nucleon number densities above $1000\,\mathrm{cm}^{-3}$. Short fall-back times are always associated with large amounts of dense gas. However, the contrary is not necessarily true, not all such with large dense gas masses undergo star formation

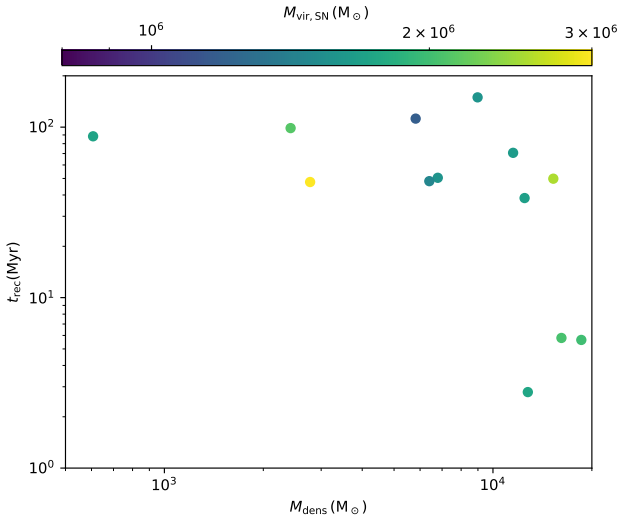

Figure 5.6: Fall-back time as function of the dense mass, i.e., the mass at nucleon number densities above 1000 cm^{-3} within the halo. The dense masses are measured shortly before the SNe. The colors correspond to the virial masses of the host halos.

immediately. Some of them are disrupted by the SNe, leading to long recovery times of the order of 100 Myr. Exploring what properties of the halos or the clumps ultimately determine the recovery time exceeds the scope of this work and will be subject to a future study.

Halos without high-density clumps always have long recovery times. There is no obvious correlation with the mass of the halos, as both very high and very low-mass halos are found among the ones with long recovery times and the halos with short recovery times are in an intermediate mass range. Therefore, the baryonic sub-structure of halos has a stronger influence on recovery time than the mass of the halo.

5.2.4 Metallicities

Metal-enriched stars form in both internally and externally enriched halos. Projections of internally enriched halos at the moment of second-generation star formation are shown in Fig. 5.7, and externally enriched halos in Fig. 5.8. The figures demonstrate that second-generation star formation occurs in a variety of different environments. In some cases (e.g. halo 1) the environment is cold, and the star forms in a clump that is less enriched by metals than the surroundings. Other cases (e.g. halo 8) show star formation in a high-metallicity environment next to an HII

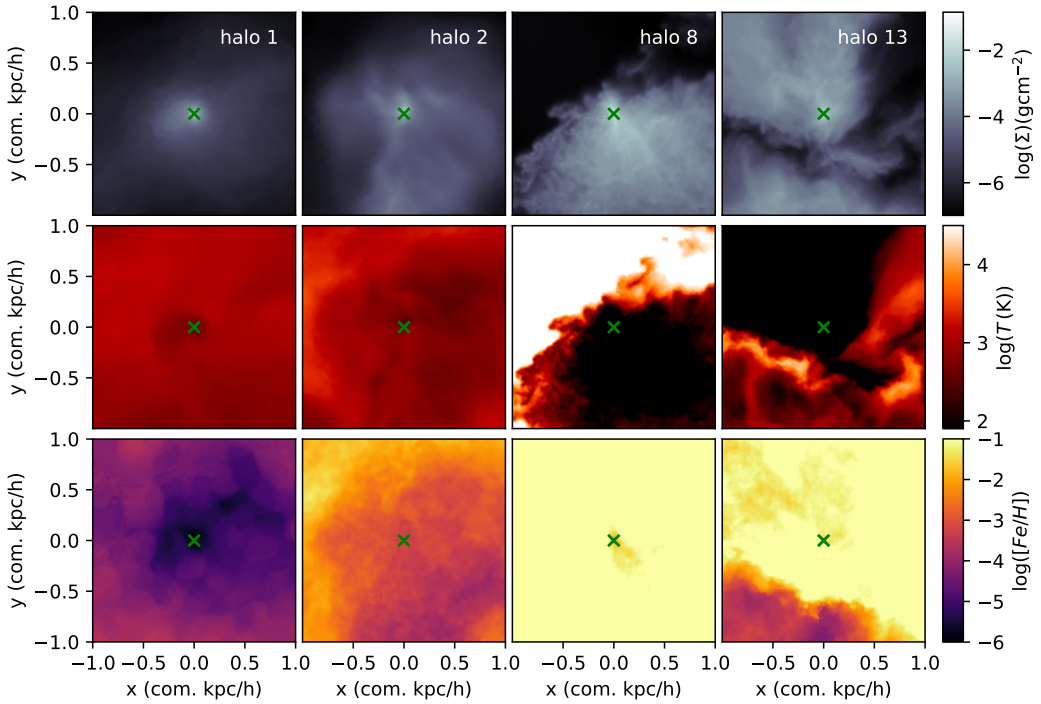

Figure 5.7: Column density (upper row), average temperature (middle row) and metallicity (bottom row) at recollapse for four internally enriched halos. The second generation stars are indicated with green crosses. We can see a variety of different mixing behaviors. Some halos (e.g., halo 8) have a relatively homogenous metallicity, whereas others (e.g., halo 1) show a steep decrease in metallicity towards the center of collapse. Similar images for the remaining halos can be found in Fig. 5.16.

region. The halo-masses of these externally enriched halos can be found in Table 5.3.

We determine the metallicities of the second generation stars that form in the simulation by counting the number of tracer particles ($N_{\rm tr}$) within the sink-formation radius around each newly-formed sink particle and comparing this with the total baryonic mass enclosed within the same volume ($m_{\rm b}$). The metallicity follows from these quantities as

$$[\mathrm{Fe/H}] = \log_{10}\left(\frac{N_{\rm tr} \times m_{\rm Fe,SN}}{N_{\rm tr,SN} \times m_{\rm b}}\right) - \log_{10}(f_{\rm Fe,\odot}), \tag{5.5}$$

where $N_{\rm tr,SN} = 10^7$ is the total number of tracer particles injected into each SN, $m_{\rm Fe,SN} = 56\,{\rm M}_\odot$ is the mass of iron produced by the SN (Heger & Woosley, 2002), and $f_{\rm Fe,\odot} = 0.00134$ is the solar iron abundance (Asplund et al., 2009). This assumes

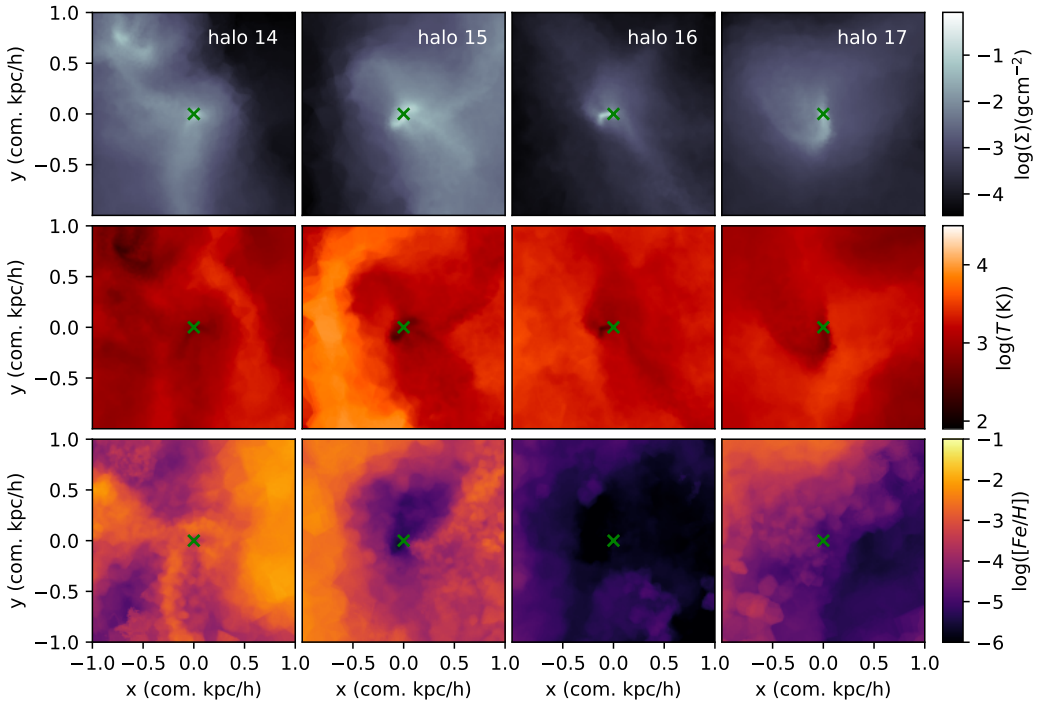

Figure 5.8: . Same as Fig. 5.7 but for four of the externally enriched halos. Images of the remaining halos are shown in Fig. 5.17.

that the initial SN ejecta are well-mixed, i.e., that all elements are distributed evenly throughout the ejecta. It is unclear whether this assumption accurately describes the mixing behavior in real SN ejecta, but given the enormous difficulties involved in modelling the resulting metal distribution in 3D SN explosions, it remains the most conservative assumption.

Our main result is that PISNe can lead to the formation of second-generation stars with a broad range of metallicities. Some indeed exhibit high metallicities in the range $-2 < [\mathrm{Fe/H}] < -1$, as predicted by the models of Karlsson et al. (2008), de Bennassuti et al. (2017) and Salvadori et al. (2019). However, most second generation stars in our simulation would be classified as EMP stars, with metallicities of $[\mathrm{Fe/H}] < -3$.

We find that externally enriched stars always have low metallicities ($[\mathrm{Fe/H}] < -3$) in our simulation, whereas internally enriched stars have the highest metallicities, reaching $[\mathrm{Fe/H}] > -2$. Five out of nine internally enriched stars have metallicities higher than the EMP threshold, three stars exhibit metallicities just below that range with $-4 < [\mathrm{Fe/H}] < -3$, and one star, with the lowest internal enrichment of all, falls in the range of $[\mathrm{Fe/H}] < -6$.

There are two obvious possible reasons for the low metallicities we find: either most of the metals are ejected from the halos or the metals are not fully mixed into the star-forming gas. In the latter case we would expect the metallicity of the second generation stars to be lower than the average metallicity of the halos. This is referred to by Chiaki et al. (2018) as inefficient internal enrichment.

In order to determine which of these two reasons is mainly responsible for the low metallicities, we compare in Fig. 5.9 the average halo metallicities to the metallicities of the second generation stars forming in the center of the halos. We find that in most cases of internal enrichment the halos are well mixed. The ejection of metals therefore is dominant in these halos. There are two cases which show lower central than halo-scale metallicity: one is halo 1 at $[\mathrm{Fe/H}] \approx -6$ and the second one is halo 12 at $[\mathrm{Fe/H}] \approx -3.4$. However, as can be seen in Fig. 5.10 only the $[\mathrm{Fe/H}] \approx -3.4$ case corresponds to a short recovery time and therefore indicates inefficient internal enrichment. The $[\mathrm{Fe/H}] \approx -6$ case has a recovery time of more than 100 Myr. This star cannot have formed from a clump in the host halo which survived the SN, as such a clump would have a much shorter free-fall time. Thus, it is more likely that this is actually a case in which an externally enriched halo merges with the original host shortly before star formation, such as reported by Smith et al. (2015). We will investigate this particular star and what conditions lead to its formation in a future

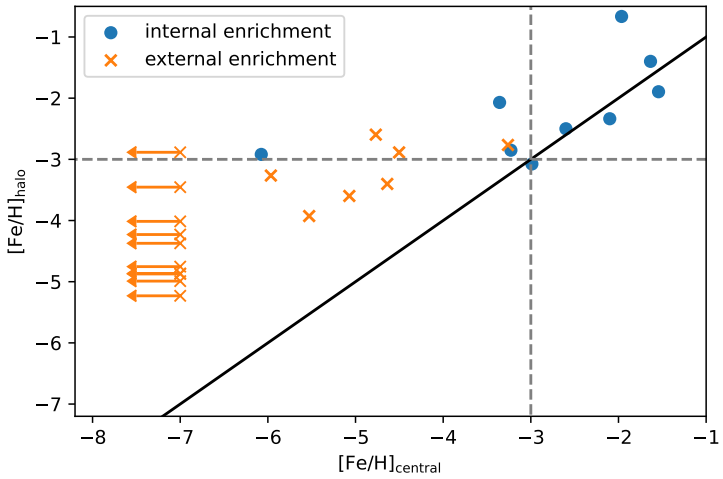

Figure 5.9: Metallicity of second generation stars compared to the metallicity of their host halos. Crosses indicate external enrichment and dots indicate internal enrichment. The upper limits set at $[\mathrm{Fe/H}] = -7$ represent cases in which the halo is only superficially enriched, yet the central star forming region does not contain metals. The grey dashed line indicates the limit for what is considered to be EMP stars, i.e., [Fe/H]$= -3$.

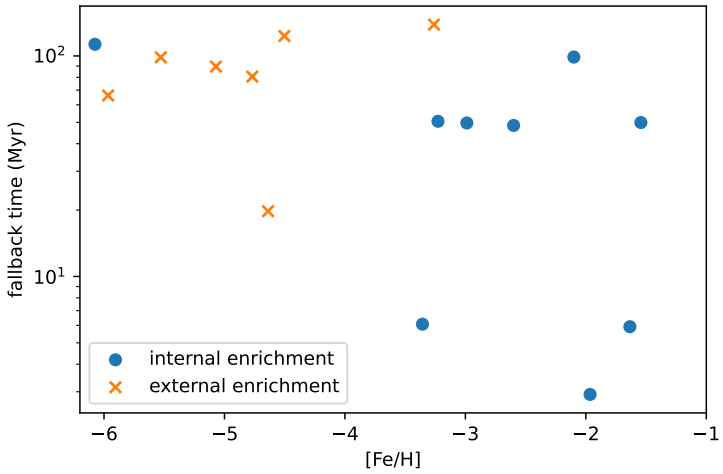

Figure 5.10: Metallicity of second generation stars as function of time since the SN. The crosses indicate external enrichment, the dots indicate internal enrichment and the grey dashed line represents the limit of what constitutes an EMP star.

study.

In the externally enriched halos, the central metallicity is commonly much lower than the average metallicity of the halos. The are many cases in which the halos are only superficially enriched but their star-forming centers remain pristine.

5.3 Discussion

5.3.1 Streaming velocities

In this paper, we include streaming velocities in a simulation that investigates the spread of metals from Pop III stars for the first time. A streaming velocity of $0.8\,\sigma_{\rm rms}$ is the most common value in the Universe; regions without a streaming velocity are very rare. It is known that streaming velocities increase the minimum halo mass for Pop III star formation (Schauer et al., 2021), but decrease the gas content in these halos (Naoz et al., 2013), and it is unclear how much a larger potential well decreases the escape of metals for internal enrichment. On the other hand, the shape of the gas component of minihalos changes: the gas is more oblate and less spherical in streaming velocity regions compared to non-streaming velocity regions (Druschke et al., 2020). In the three-dimensional halo structure, this might lead to more escape paths for ionizing radiation and subsequently the spread of metals into the surrounding. We speculate that external enrichment could be enhanced in streaming velocity regions but testing this is a task for future work.

5.3.2 Mixing, enrichment and dilution

Our simulation shows a variety of different behaviors with regards to metal enrichment, mixing, dilution and the formation of second generation stars. A key question here is how much the SN ejecta are mixed with the pristine ambient medium before second-generation stars can form. There have been numerous studies attempting to investigate this issue with analytical and numerical models. We compare our results to these earlier studies in this section.

In 4 I derived a lower limit for the mass of pristine material that the ejecta from the first SNe are diluted into. To compare our results to this limit, we compute effective dilution masses, i.e., the mass of pristine material the SN ejecta would have to mix with homogeneously in order to arrive at the found metallicity for all of our second generation stars. In Fig. 5.11, the dilution masses are compared to

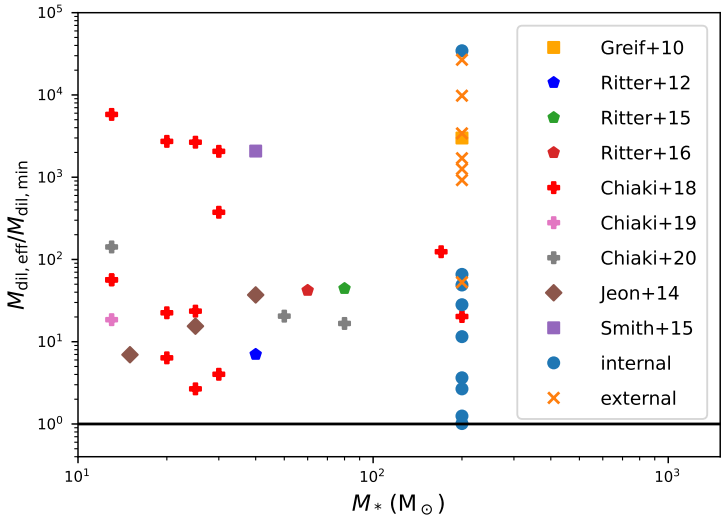

Figure 5.11: Comparison of the metal dilution found in our simulations and in the literature with the analytic lower limit derived in Chapter 4. We show the ratio of the effective dilution mass to the analytic limit, as function of the stellar mass of the SN progenitor. The analytic limit for our PISNe is $M_{\rm dil,min} = 1.6 \times 10^6\,{\rm M}_\odot$. Results from this work are shown as blue circles (internal enrichment) and orange x-symbols (external enrichment). The other symbols show values from a range of previous studies, as indicated in the key. In every case, the ratio is greater than 1, indicating that the results are consistent with the analytic limit.

the analytical lower limit of

$$M_{\rm dil,min} = 1.9 \times 10^4\,{\rm M}_\odot\,E_{51}^{0.96} = 1.6 \times 10^6\,{\rm M}_\odot, \tag{5.6}$$

as derived in Chapter 4. Here, E_{51} is the explosion energy of the SN in units of foe. The Figure is an adaptation of Fig 4.1 and contains values from the simulations by Greif et al. (2010), Ritter et al. (2012, 2015, 2016), Jeon et al. (2014), Chiaki et al. (2018), Chiaki & Wise (2019), Chiaki et al. (2020) and Smith et al. (2015) for comparison. Despite our dilution masses scattering over five orders of magnitude, our lowest value is 2% above the analytical limit, and therefore our simulation is consistent with it.

The model by Chiaki et al. (2016) predicts that our halos are at the border between internal and external enrichment, and thus we would expect to see both in our simulation. This expectation is consistent with our findings. However, according to this model, for a $200\,{\rm M}_\odot$ Pop III star, inefficient internal enrichment and the associated short recovery times should only be possible in halos more massive than $M_{\rm vir} = 2 \times 10^7\,{\rm M}_\odot$. From the fact that we see both, inhomogeneous mixing as well

as short recovery times, in halos around one order of magnitude less massive than this threshold we conclude that inefficient internal enrichment is governed by the presence of complex baryonic sub-structures within the halo rather than by the total halo mass.

That recollapse occurs quite frequently stands in contrast to the picture painted by Whalen et al. (2008) in which halos do not recollapse. Probably, this difference is due to our simulation being multi-dimensional, i.e., our halos being able to accrete new gas along cosmic filaments before all of the SN remnant has cooled.

Semi-analytical and semi-numerical models of metal-mixing after Pop III formation often assume homogeneous mixing or a parametrized mixing model (Karlsson et al., 2008, de Bennassuti et al., 2017, Hartwig et al., 2018a, Salvadori et al., 2019). Due to the large yields of PISNe, second generation stars are often relatively metal-rich ([Fe/H]~ -2) in these models. While we see instances of this behavior, we typically find much lower metallicities. This decrease is due to large inhomogeneities in mixing, especially in externally enriched halos, due to mixing with a large amount of pristine material and due to the ejecta of metals from the halos.

Generally, we find that internally enriched halos have a more homogeneous metallicity distribution than externally enriched halos. Tarumi et al. (2020b) developed a model for this effect and find that also in larger simulations (by Xu et al., 2016b), externally enriched halos have lower metallicities in their star-forming centers. The reason for this is that metals do not easily mix into dense centers of already formed halos from the outside (Chen et al., 2017b).

5.3.3 Where are the stars with PISN patterns?

If massive PISNe with a strongly pronounced odd-even effect are indeed common in the early Universe, our simulations would pose a conflict with the observed abundance patterns of EMP stars. Thus far, there is only one candidate star found that could be enriched by a PISN (Aoki et al., 2014), and it is not in the EMP regime. We have seen that two of the primary hypotheses - those of large metallicities and the destruction of halos - cannot explain this discrepancy. Isolated massive PISN should lead to the formation of EMP stars, which would be commonly recovered in surveys targeting these stars (such as Youakim et al., 2020, François et al., 2018).

There are several remaining explanations. The most obvious one is that sufficiently massive stars do not form or are exceedingly rare. Only a combination of forward modelling the formation of PISN-enriched stars in the progenitors of the

Milky Way and a quantitative analysis of observed abundance patterns can constrain how rare exactly PISNe would have to be to account for the current lack of detections of PISN-enriched stars.

Additionally, if massive Pop III stars do not form in isolation but instead are close to other stars that explode as type II SNe, our predictions may not hold as well. There have so far been only very limited studies that investigate the mixing of ejecta from several Pop III SNe (Ritter et al., 2015) and a set of dedicated detailed simulations with a sufficiently large sample of halos will be neccessary to investigate this scenario. One difficulty to overcome in this scenario is that PISNe have very large yields and therefore, if mixed homogeneously, easily dominate the metal abundances in stars enriched by several SNe (Hartwig et al., 2018b)

For the second generation stars to survive until and be observable at the present day, they need to be low enough in mass. At which metallicity the transition from high-mass Pop III-like star formation to a bottom-heavy more Salpeter-like IMF occurs is still an open question (Greif, 2015). Metal-line cooling starts to be an effective source of cooling around metallicities of $[Fe/H] \approx -3$. However, low-mass star formation must be possible at lower metallicities, since lower-metallicity stars have been observed (see e.g. Nordlander et al., 2019). The additional source of cooling that may facilitate low-mass stars to form at these metallicities is dust cooling. However, at which metallicity dust cooling becomes efficient depends on the amounts, kinds, and grain-size-distribution of dust in the SN ejecta (Schneider et al., 2012, Chiaki et al., 2017). Therefore, modelling dust-grain formation in PISN remnants will be a crucial step in understanding the implications of stellar archaeology for PISNe.

Finally, we note that our conclusions apply only to non-rotating, massive, and energetic PISNe. Stars that are close to the PISN mass-limit, i.e., stars with masses around $150\,\mathrm{M}_\odot$, are expected to have substantially smaller explosion energies and yields (Gilmer et al., 2017). Also stellar rotation can have a crucial impact on the evolution and explosion of metal-free stars (Meynet & Maeder, 2017, Murphy et al., 2021).

5.3.4 Caveats and extensions

Building up on the work presented here, our simulation could be extended to cover the formation of the first galaxies, rather than only considering the first two generations of stars. In order to do this, the simulations will need to determine the metal-

licity of a newly forming star at runtime, rather than in the current post-processing step. Improving this aspect would allow us to investigate mixing of metals from SNe of different populations of stars. We are limiting this simulation to the extreme case of $200\,\mathrm{M}_\odot$ Pop III stars with PISNe. Future simulations will sample stars from a more realistic Pop III IMF, and make predictions of second-generation stars arising from an specific IMF.

While we are modelling local radiative feedback with high physical fidelity in the LW and ionizing bands, our implementation of LW feedback is less advanced. Firtly, we do not include LW self-shielding. Kitayama et al. (2004) and Schauer et al. (2015, 2017b) have shown that extremely high spectral and spatial resolution is required to accurate model the escape of LW radiation from minihalos. It is questionable whether such high resolutions can be achieved in three-dimensional cosmological simulations in the intermediate future. Secondly, we currently do not account for a global LW background. Choosing a global LW background and its evolution with redshift will require careful consideration, as it depends on escape fractions, the large-scale star formation rate and the IMF and the spectra of the forming stars. As LW radiation has a much longer mean free path than our simulated volume, modelling this background self-consistently is currently not possible.

5.4 Summary

In this chapter we use a cosmological simulation to model the formation of the first stars, their feedback, their explosion as PISNe and afterwards the formation of the first metal-enriched stars. Our findings are:

1. In the $1\,\mathrm{Mpc}\,h^{-1}$ simulation box, there are 14 halos forming one Pop III star formation each before $z = 19$. In accordance with previous predictions, our halos form stars at a virial mass of $M_\mathrm{vir} \approx 2 \times 10^6\,\mathrm{M}_\odot$.

2. At $z = 19$ we deactivate stellar feedback and wait for the halos to recollapse. In the following 135 Myr most of our halos recollapse and we see various instances of externally and internally enriched formation of metal-poor stars.

3. Halos either recollapse quickly ($t_\mathrm{rec} < 10\,\mathrm{Myr}$, in three cases), slowly ($t_\mathrm{rec} > 40\,\mathrm{Myr}$, in nine cases) or not at all ($t_\mathrm{rec} > 135\,\mathrm{Myr}$, one case). Which of these paths they take depends on their baryonic substructure at the time of the SN, but it is not yet clear what exact criteria are required to enable the fast recollapse.

4. While the least-massive halo does not recollapse, among those that do recollapse, we find no direct correlation between the halo mass and the recovery-time.

5. Second generation stars in externally-enriched halos start forming 70 Myr after the SNe.

6. We find a wide variety of metallicities of the second generation stars. Out of the sixteen second generation star-forming regions we find three have relatively high metallicities ([Fe/H] ≥ -2) and two have intermediate metallicities ($-2 <$ [Fe/H] < -3). All of these are formed by internal enrichment. Most of our second generation star-forming regions (eleven out of sixteen) are in the EMP ([Fe/H] ≤ -3) regime. Most of the lowest-metallicity stars are formed by external enrichment.

7. The effective dilution mass scatters over 5 orders of magnitude. In all cases, our results are consistent with the analytical minimum of $1.6 \times 10^6\,\mathrm{M}_\odot$ (see Chapter 4).

Since PISNe are expected to produce a very characteristic pattern of elemental abundances, and since this pattern is rarely observed, these results stand in tension with the measured elemental abundances in EMP stars. This may indicate that PISNe of the kind we investigate have been exceedingly rare in the early Universe. Possible alternative scenarios are mixing of several SNe, low mass stars not being able to form in the lower metallicity gas, or less characteristic SN yields. We will investigate the first of these alternatives in a follow-up study.

5.5 Additional Figures & Halo Properties

In this Section we summarize halo properties, and show additional visual representations of the halos that are not included in the projections in them main paper. The properties of the Pop III forming halos are found in Table 5.2. The halos that have a recovery time but no metallicity of the second-generation stars, are halos which form stars after the SNe, but only after merging with other halos that contain stars. As we do not model feedback from second-generation stars, we cannot determine the metallicities of these stars.

Halos 1, 2, 8, and 13 are shown in Figures 5.3, 5.5 and 5.7 at the the time of the formation of the Pop III star, shortly before the SN and at recollapse respectively.

halo	$z_{\rm col}$	$z_{\rm sn}$	$z_{\rm rec}$	$M_{\rm vir,col}$	$M_{\rm vir,rec}$	$t_{\rm rec}$	$M_{\rm dens}$	[Fe/H]	$[{\rm Fe/H}]_{\rm halo}$
—	—	—	—	$10^6\,{\rm M}_\odot$	$10^6\,{\rm M}_\odot$	Myr	$10^3{\rm M}_\odot$	—	—
0	24.0	23.8	19.2	2.7	7.1	47.6	2.7	-3.0	-3.1
1	22.3	22.1	15.1	1.1	8.5	112	5.8	-6.0	-2.9
2	21.8	21.6	17.9	1.6	5.5	50.5	6.8	-3.2	-2.9
3	21.8	21.6	13.6	1.5	12.7	150	9.0	—	—
4	20.4	20.3	—	0.8	—	—	0.15	—	—
5	20.4	20.2	17.5	1.2	5.4	38.4	12.5	—	—
6	20.0	19.8	15.7	1.6	5.8	70.7	11.5	—	—
7	20.0	19.8	15.0	1.7	4.8	88.4	0.61	—	—
8	19.9	19.7	19.5	1.7	1.8	2.8	12.8	-2.0	-0.7
9	19.8	19.6	14.5	2.0	12.1	98.7	2.4	-2.1	-2.3
10	19.8	19.6	16.7	1.3	6.1	48.2	6.4	-2.6	-2.5
11	19.7	19.5	16.5	2.4	8.2	49.8	15.3	-1.5	-1.9
12	19.7	19.5	19.1	1.9	2.3	5.8	16.2	-3.4	-2.1
13	19.6	19.5	19.0	1.9	2.3	5.6	18.6	-1.6	-1.4

Table 5.2: Properties of the halos forming Pop III stars. The columns are: halo number(1), redshift of first star formation (collapse redshift, 2), redshift of the SN (3), redshift of recollapse (4), estimated virial mass at collapse (5), estimated virial mass at recollapse (6), recovery time (7), mass of dense gas in the halo shortly before the SN (8), metallicity of 2nd generation star (9), metallicity of halo at recollapse (10). Note that halo 4 does not recollapse, and that halos 3 and 7 accrete Pop II stars from external halos before recollapsing, and we therefore cannot make reliable metallicity determinations for the star formation during recollapse in these halos.

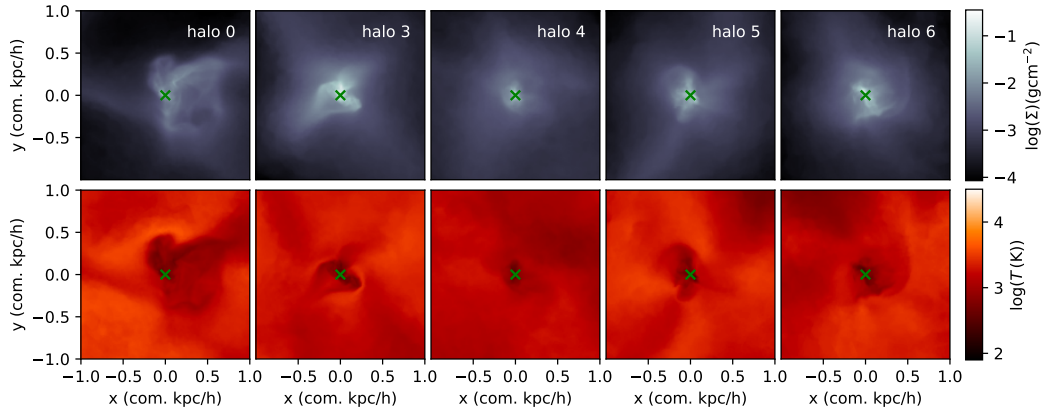

Figure 5.12: As Fig. 5.3, but for halos 0, 3, 4, 5, and 6

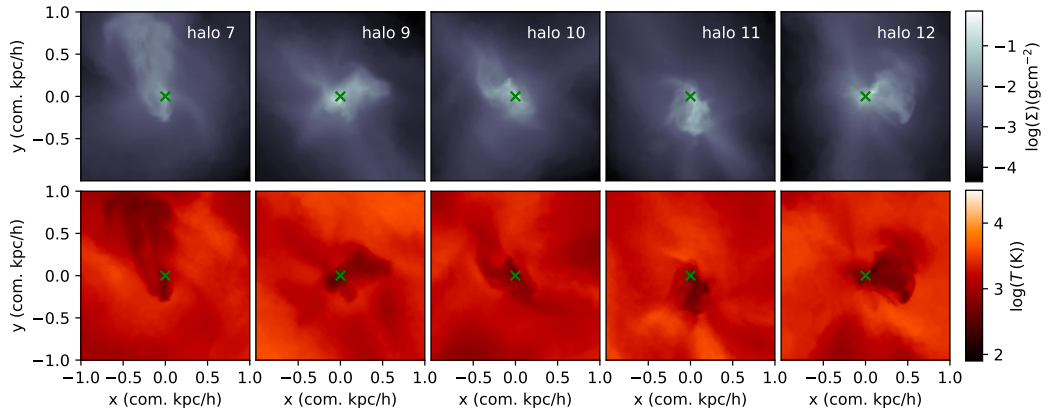

Figure 5.13: As Fig. 5.3, but for halos 7, 9, 10, 11, and 12

Similarily the remaining halos are shown in Figures 5.12 and 5.13 at star formation, in Figures 5.14 and 5.15 shortly before the SNe and in Fig. 5.16 at recollapse. We show these images for completeness and to give readers a visual impression of the halos. A more detailed analysis of the substructures and clumps seen within the figures will be subject to a follow-up study.

The properties of the externally enriched halos which form stars with non-zero metallicity are summarized in Table 5.3. The halos at star formation are show in Fig. 5.17 and the main paper in Fig. 5.8.

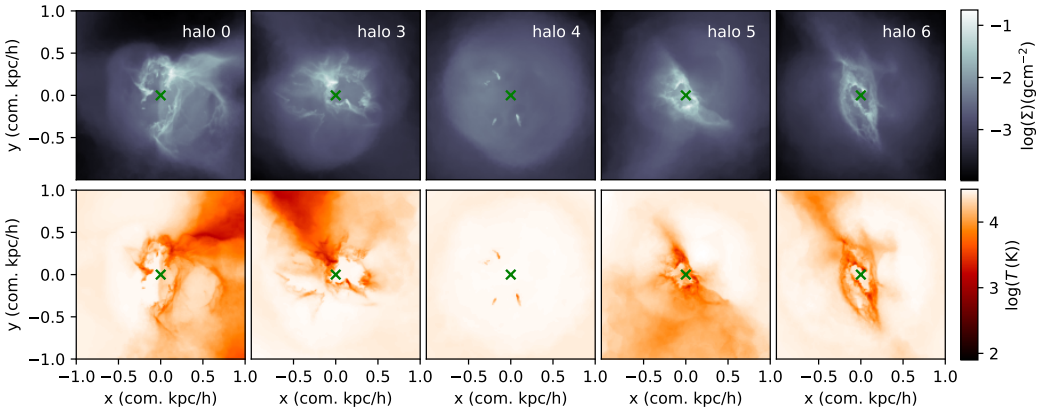

Figure 5.14: As Fig. 5.5, but for halos 0, 3, 4, 5, and 6

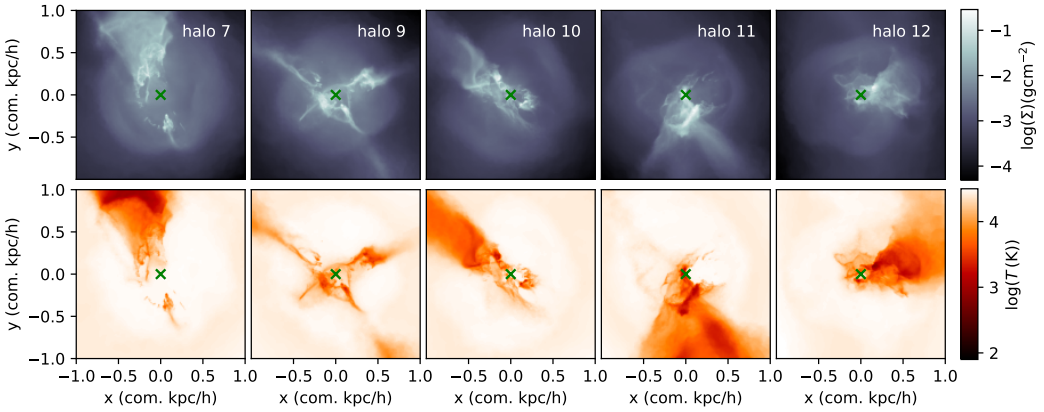

Figure 5.15: As Fig. 5.5, but for halos 7, 9, 10, 11, and 12

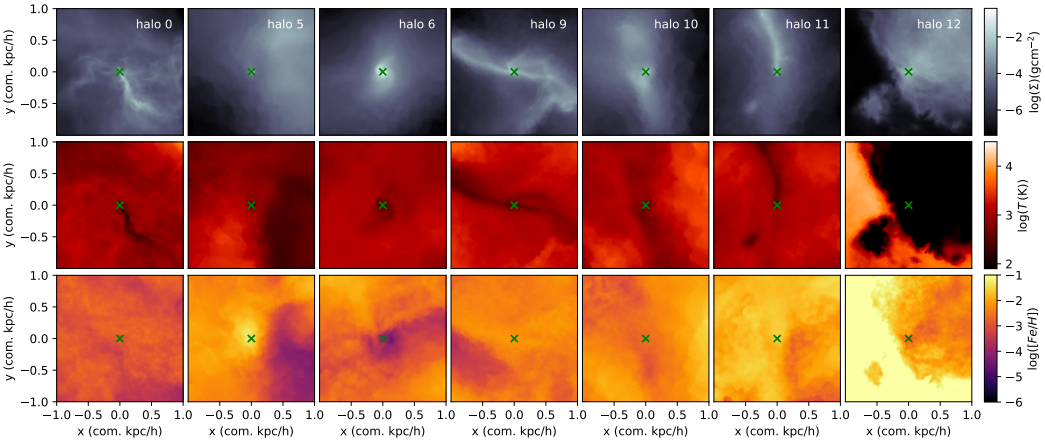

Figure 5.16: As Fig 5.7 but for halos 0 5, 6, 9, 10, 11, and 12

halo	enriching halo	$z_{\rm col}$	$M_{\rm vir,col}$	$t_{\rm sn}$	d	[Fe/H]	$[{\rm Fe/H}]_{\rm halo}$
—	—	—	$10^6\,{\rm M}_\odot$	Myr	kpc/h	—	—
14	18.2	12	0.9	19.8	7.3	-4.6	-3.4
15	16.3	3	3.1	80.6	11.7	-4.8	-2.6
16	15.8	12	2.0	66.2	25.2	-6.0	-3.3
17	15.0	6	1.7	89.5	17.1	-5.1	-3.6
18	14.5	2	0.7	123.1	19.0	-4.5	-2.9
19	14.5	11	2.2	98.6	34.8	-5.5	-3.9
20	14.1	1	0.9	138.8	5.4	-3.3	-2.8

Table 5.3: Externally enriched halos. The columns are: halo number(1), enriching halo (2), collapse redshift (3), estimated virial mass at collapse (4), time since SN (5), distance between star and the enriching SN (6), metallicity of the star (7), metallicity of halo at collapse (8).

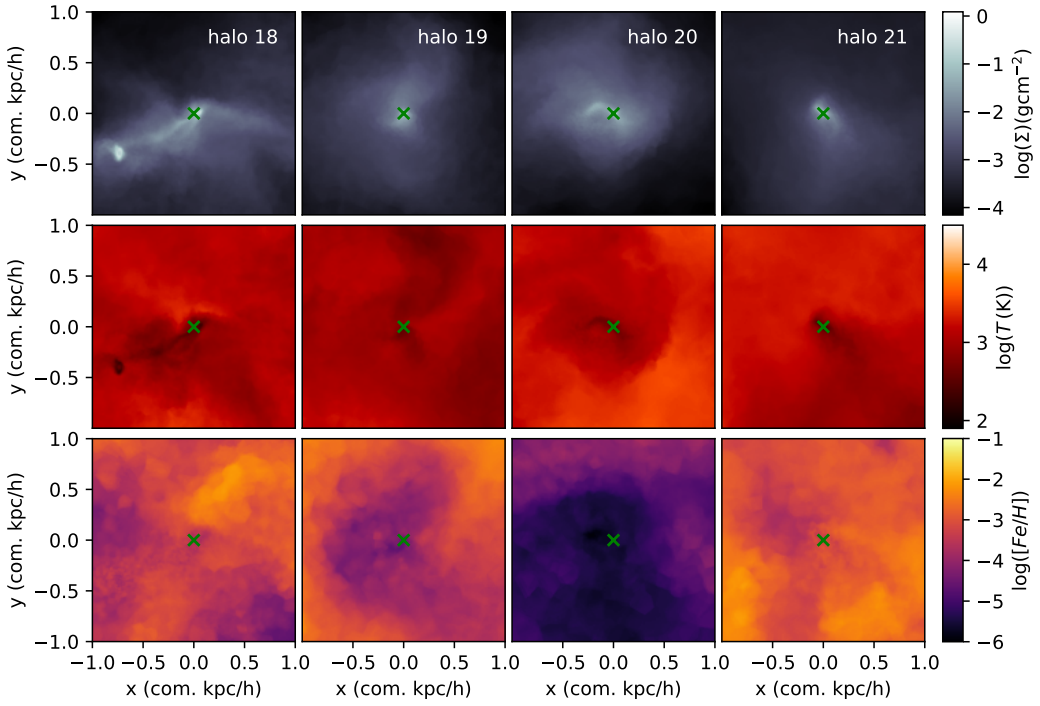

Figure 5.17: As Fig. 5.8, but for halos 18, 19, and 20

6

Effect of the cosmological transition to metal-enriched star-formation on the hydrogen 21-cm signal

Published as Magg et al. (2021b)

Mapping Cosmic Dawn with 21-cm tomography offers an exciting new window into the era of primordial star formation. However, self-consistent implementation of both the process of star formation and the related 21-cm signal is challenging, due to the multi-scale nature of the problem. In this chapter, we develop a flexible semi-analytical model to follow the formation of the first stars and the process of gradual transition from primordial to metal-enriched star formation. For this transition we use different scenarios with varying time-delays (or recovery times) between the first SNe and the formation of the second generation of stars. We use recovery times between 10 and 100 Myr and find that these delays have a strong impact on the redshift at which the transition to metal-enriched star formation occurs. We then explore the effect of this transition on the 21-cm signal and find that the recovery time has a distinctive imprint in the signal. Together with an improved understanding of how this time-delay relates to the properties of Population III stars, future 21-cm observations can give independent constraints on the earliest epoch of star formation.

Disclaimer

This chapter has been submitted for publication to the Monthly Notices of the Royal Astronomical Society as Magg et al. (2021b). The text has been primarily written by me but in collaboration with all listed coauthors. Sections 6.3 and 6.4 and the figures therein are work by Itamar Reis and Anastasia Fialkov, which was planned and developed in close collaboration. The remainder of the figures as well as the presented ideas are my work and have been created with feedback from all coauthors.

6.1 Introduction

Observations of the cosmic 21-cm signal offer a new alternative way to probe the onset of star formation and constrain the properties of Pop III and Pop II stars. The cosmic 21-cm signal is produced by neutral inter-galactic hydrogen in the high redshift Universe (see Barkana, 2018b, Mesinger, 2019, for recent reviews of the topic). It provides a window to the evolution of the Universe between the Dark Ages ($z \sim 100$) through Cosmic Dawn ($z \sim 15-25$) until the Epoch of Reionization (EoR, $z \sim 6-10$). The 21-cm signal is predominantly determined by the occupancy of the hydrogen hyperfine levels (characterized by the spin temperature, which depends on the luminosity of high-redshift sources in ultraviolet, X-ray and radio bands), the ionization state of the gas as well as its density and velocity (e.g. Madau et al., 1997). Owing to its dependence on the properties of sources, the 21-cm signal can be used to characterize high redshift stars, black holes and galaxies at high redshift. Observational effort to detect both the sky-averaged (global) 21-cm signal and its fluctuations across the sky is ongoing. Experiments aiming to measure the global signal include EDGES (Bowman et al., 2013), LEDA (Price et al., 2018), SARAS (Singh et al., 2018), PRIZM (Philip et al., 2019), MIST[1] and REACH[2]; while interferometers including the LOFAR (Gehlot et al., 2019), HERA (DeBoer et al., 2017), LWA (Eastwood et al., 2019), NenuFAR (Zarka et al., 2012), LEDA (Garsden et al., 2021) and MWA (Trott et al., 2020) as well as the future SKA (Koopmans et al., 2015) aim to measure the fluctuations of the 21-cm signal from the EoR and Cosmic Dawn. The first tentative detection of the global signal was reported by the EDGES collaboration (Bowman et al., 2018). Although the true nature of this signal is still debated (e.g. see Hills et al., 2018, Sims & Pober, 2020),

[1] `http://www.physics.mcgill.ca/mist/`
[2] `https://www.kicc.cam.ac.uk/projects/reach`

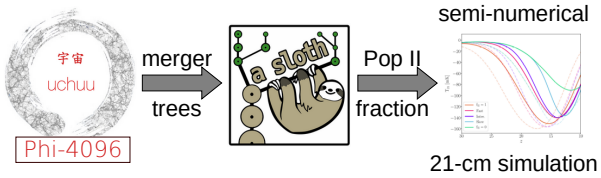

Figure 6.1: Illustration of our workflow. The Uchuu simulations and the generation of merger trees are part of Ishiyama et al. (2021).

if it truly is of cosmological origin it represents a direct evidence of star formation at $z \sim 17$ when the Universe was ~ 230 million years old. Here, we aim at investigating the effect of the transition between the first- and second generation stars (Pop III and Pop II stars) on the global 21-cm signal and the power spectrum of 21-cm fluctuations. This effect is inherently difficult to model, since the minihaloes in which the first stars form have sizes of the order of one comoving kpc, yet due to the large mean free paths of ultraviolet and X-ray radiation, the 21cm signal is shaped on scales of hundreds of comoving Mpc. It is not yet feasible to simulate the effect of first stars on the large-scale 21-cm signal in a self-consistent way. Therefore, we use the following approach: We model the formation of Pop III and Pop II stars with the semi-analytical model A-SLOTH as described in Section 6.2. In Section 6.2.3 we use those results to model the transition from metal-free to metal-enriched star formation under varying sets of assumptions for the recovery time, i.e., the time-delay between the first SNe and the formation of the first Pop II stars, the local large-scale density field and the minimum mass of star forming haloes. This prescription is then used in large-scale semi-numerical cosmological simulations of the 21-cm signal (Section 6.3) with the results discussed in Section 6.4. Since our workflow relies on three different simulation methods, we include a schematic representation in Fig. 6.1. We discuss our results in the context of other existing works in the field in Section 6.5. Finally, we conclude in Section 6.6.

6.2 Semi-analytical prescription for PopIII-PopII transition

6.2.1 N-body simulations

We base our semi-analytical model on merger trees generated from the *Uchuu* cosmological dark-matter-only N-body simulations (Ishiyama et al., 2021), specifically the simulations labelled Phi-4096. We briefly summarize how the N-body simulations are set up and how the merger trees were generated. More details can be

found in (Ishiyama et al., 2021). The Phi-4096 simulation models the formation of structure in a box with a comoving edge-length of $16\,\mathrm{Mpc}\,h^{-1}$ and a resolution of 4096^3 particles, corresponding to a particle mass of $5.13 \times 10^3\,\mathrm{M}_\odot\,h^{-1}$. Having this high resolution is important as it allows us to follow even the smallest haloes in which stars may form. Initial conditions were generated with MUSIC (Hahn & Abel, 2011) and use the cosmological parameters from Planck Collaboration et al. (2014): $\Omega_m = 0.31, \Omega_b = 0.048, \Omega_\Lambda = 0.69, h = 0.68, n_s = 0.96$ and $\sigma_8 = 0.83$. The simulations are initialized at $z_{\mathrm{ini}} = 127$.

Snap-shots are spaced regularly in intervals of $\Delta \log_{10} \frac{1}{z+1} = 0.01$, where the first snapshot is at $z \approx 31$ and the last snapshot for which the merger-trees are available is at $z \approx 10$. This leads to the time between the snapshots being 3.5 Myr at the highest and 16 Myr at the lowest redshifts. The halo properties were computed with ROCKSTAR (Behroozi et al., 2013a) and the merger trees were generated with CONSISTENT-TREES (Behroozi et al., 2013b). At a minimum of 40 particles per halo, the merger trees contain haloes with a minimum mass of $2 \times 10^5\,\mathrm{M}_\odot\,h^{-1}$ and consist of a total of 1.3 billion tree-nodes.

6.2.2 Basic semi-analytical model

In order to quantify the transition from metal-free to metal-enriched star formation we use A-SLOTH[3] (Magg et al. in prep). This semi-analytical model simulates early star formation based on merger trees which in our case are taken from the N-body simulations described in Section 6.2.1. The model is based on the premise that only haloes with masses above a threshold value M_{crit} (minimum cooling mass) will form the first (i.e., Pop III) stars and will subsequently transition to forming Pop II stars after the first SNe that enrich the gas with metals. We here aim at parametrizing the transition from metal-free to metal-enriched star formation, in different cosmic overdensities as a function of the critical mass.

The criterion to decide when haloes form stars for the first time is parametrized by T_{crit}, which is the critical virial temperature of the halo, related to M_{crit} via

$$M_{\mathrm{crit}} = 1.0 \times 10^6\,\mathrm{M}_\odot \left(\frac{T_{\mathrm{crit}}}{10^3\,\mathrm{K}}\right)^{3/2} \left(\frac{1+z}{10}\right)^{-3/2}. \tag{6.1}$$

A typical value for enabling collapse by molecular hydrogen cooling is $T_{\mathrm{crit}} = 2200\,\mathrm{K}$ (Hummel et al., 2012).

[3] Ancient Stars and Local Observables by Tracing Haloes

In contrast to previous models, when using A-SLOTH we do not explicitly account for the effect of LW radiation (Machacek et al., 2001, O'Shea & Norman, 2008, Schauer et al., 2021) or supersonic baryon streaming (a residual velocity difference between dark matter and baryonic matter resulting from recombination, Tseliakhovich & Hirata, 2010) which are expected to affect $T_{\rm crit}$ in a non-uniform manner (e.g. Fialkov et al., 2012, Schauer et al., 2019a). These two effects are taken into account at a later stage (in the cosmological 21-cm simulations described in Section 6.3. In the semi-analytical model described in this Section we consider $T_{\rm crit}$ to be a free parameter.

We test 29 different values for $T_{\rm crit}$, spaced regularly in log-space between $T_{\rm crit} = 1500\,{\rm K}$ and $T_{\rm crit} = 50000\,{\rm K}$, which covers the range relevant for the early star formation (see Section 6.3). The lower limit here roughly corresponds to the smallest haloes that can be resolved with the N-body simulations at $z = 30$. The upper limit is well above the atomic cooling limit ($T_{\rm crit} = 10000\,{\rm K}$), where haloes start to cool efficiently by atomic hydrogen emission. In this regime molecular hydrogen is no longer required to enable cooling, and, therefore, haloes can only be prevented from collapse in relatively extreme conditions (Visbal et al., 2016, Agarwal et al., 2016). Specifically, Visbal et al. (2016) find that haloes as massive as 10 times the atomic cooling limit can be prevented from collapse in the presence of a strong ionizing radiation field, but haloes at even higher masses can not. For this reason we do not consider $T_{\rm crit}$ values above the 50000 K threshold.

When a halo first exceeds the mass threshold, it forms Pop III stars in a single instantaneous burst. In our model, only one generation of metal-free stars can form in each halo, which is what is generally seen in simulations of the first SNe (Jeon et al., 2014, Smith et al., 2015, Chiaki et al., 2016). To determine the Pop III stellar mass we assume that stars form with a fixed star formation efficiency, i.e., when a halo forms Pop III stars, the stars are sampled from an IMF until they reach a total mass of

$$M_{*,\rm III} = 0.01 \frac{\Omega_{\rm b}}{\Omega_{\rm m}} M_{\rm vir}, \tag{6.2}$$

where the 0.01 represents our adopted Pop III star formation efficiency. The stars are sampled from an IMF with the shape

$$\frac{{\rm d}N}{{\rm d}\log(M)} \propto M^{0.5} \tag{6.3}$$

within the limits $M \in [2.0\,{\rm M}_\odot, 180\,{\rm M}_\odot]$. Star formation efficiency and IMF are taken

from Tarumi et al. (2020) and have been calibrated with the metal-poor end of the metallicity distribution function of the Milky Way. In this calibration parameters of Pop III and Pop II formation are chosen to match such that the modelled metallicity distribution of metal-poor stars matches the observed distribution. The lifetimes of the stars are taken from Schaerer (2002) and stars within the mass ranges of 8–40 $M_\odot$ and 140–260 $M_\odot$ are assumed to explode as SN at the end of their lifetime (Heger & Woosley, 2002). In our main model considered here, the treatment of feedback is highly simplified, and therefore the IMF and star formation efficiency have a very small effect. To be precise, they slightly affect the delay between star formation and the first SNe, because they change the distribution of stellar life-times before the SNe explode and how completely this distribution is sampled. Other effects that can depend on the IMF and star formation efficiency, such as a changed radiation output or a differences in outflows caused by SNe, are not taken into account in this simplified model. In order to avoid artifacts due to the time-discretization of the merger trees (see e.g. Magg et al., 2016) we assign the time of star formation of a halo randomly between the current time-step and the next.

After the first stars explode, their host halo is enriched with metals and, thus, in principle is able to form metal-enriched Pop II stars. However, the SNe also eject a very significant amount of energy into the system, heating up the gas and potentially even destroying the halo. The time a halo needs to recover from such a SN is poorly understood and potentially depends on the halo mass and the type and the number of SNe exploding in the halo (Jeon et al., 2014, Chiaki et al., 2018). Such dependencies are not clear yet and especially the statistical scatter between equal mass haloes is poorly understood. Therefore, we assume that the recovery time, $t_{\rm recov}$, i.e., the time between the SNe of the first stars and the time of formation of the first Pop II star in a halo, is a free parameter and is equal for all haloes. We explore the effect of the recovery time by adopting three different values: $t_{\rm recov} = 10\,{\rm Myr}$, $t_{\rm recov} = 30\,{\rm Myr}$ and $t_{\rm recov} = 100\,{\rm Myr}$ to which we refer as *fast*, *intermediate* and *slow* transitions. These values encapsulate the range of values measured in hydrodynamical simulations (Greif et al., 2010, Jeon et al., 2014, Smith et al., 2015, Chiaki et al., 2018). A slower transition does not lead to more Pop III stars forming, it only means that the formation of the first metal-enriched generation of stars is delayed by a longer period of time.

In this picture, the slow transition with the longest recovery time is associated with the dominance of small star-forming haloes populated by massive stars, which explode as very energetic SNe and evacuate most of the gas out of the halo. In such

a scenario, a long time is required for the haloes to re-collapse and start forming stars again, this time out of the metal-enriched gas (Whalen et al., 2008, Jeon et al., 2014, Chiaki et al., 2018). Several SNe going off in the same halo can have a similar effect (Ritter et al., 2015).

The intermediate and the fast transitions correspond to the cases in which the stellar feedback is not strong enough to fully destroy the host haloes, and therefore some baryonic material remains dense and bound to the halo. Chiaki et al. (2018) refer to an extreme case of such scenarios as the 'inefficient internal enrichment' channel. Whether and how much gas remains in the haloes depends not only on the properties of Pop III stars, but also on the baryonic substructure of the star-forming haloes. Therefore, while small recovery times could qualitatively be associated with weak feedback, less massive Pop III stars and a low star formation efficiency, the exact correspondence between $t_{\rm recov}$ and the properties of Pop III stars in this regime is unclear.

We model the transition to metal-enriched star formation in two different ways: with our main simplified model and with an additional complete model. In our main model, we neglect the back-reaction that photoionization feedback and external enrichment would have on the Pop III fractions[4]. These simplifications are well justified for two reasons: Firstly, the external metal enrichment is expected to have only a small effect at the high redshifts of interest (Visbal et al., 2018, 2020). Secondly, the Universe is expected to be largely neutral at these times. We verify that the back-reaction indeed has a negligible effect on the Pop III-Pop II transition by exploring an additional 'full' model in which these types of feedback are taken into account (see Appendix 6.7.1). We find that these types of feedback do not have a significant effect on the resulting Pop II fractions, i.e., that their impact on the Pop III-Pop II transition is small compared to the change introduced by varying the recovery time. Finally, we note that these types of feedback may still be important for sub-haloes of larger objects. However, at the moment sub-haloes are not treated in the large-scale 21-cm simulations described in Section 6.3, which rely on a star formation prescription based on analytical HMFs.

[4]While the impact of reionization at the time of the Pop III-Pop II transition is expected to be small as most of the Universe is neutral at high redshifts, we do account for the ionizing feedback in the large-scale 21-cm simulations described in Section 6.3.

6.2.3 Transition to metal-enriched star formation

In our semi-analytical model haloes are labelled as Pop II forming one recovery time after they experienced their first Pop III SN. To quantify the transition to Pop II star formation we compare the sum of the (virial) masses of all Pop II forming haloes with the total mass of all haloes above the star formation threshold. We define the Pop II fraction, $f_{\rm II}$, as the ratio of these two masses, i.e., as the mass fraction of haloes above the critical mass that form Pop II stars.

This definition is chosen on purpose over, e.g., considering the stellar masses of Pop II or Pop III stars, because, to first order, it is independent of the star formation efficiencies. This feature makes it easy to integrate $f_{\rm II}$ into the large-scale simulations of the 21-cm signal (Section 6.3). The only way the star formation efficiencies affect the Pop II fraction in this definition is via the timing of Pop III SNe (and via the minor effects of external enrichment and radiative feedback, which are not considered in our main model but only in the model in Appendix 6.7.1). There also is an expected dependence of the recovery time on the Pop III star formation efficiency, as more stars in a halo should lead to a larger number of SNe and, thus, more efficiently disrupt the halo. However, Chiaki et al. (2018) have shown that even two very similar haloes with the same stellar mass content can have vastly different recovery times. Therefore, we assume that the recovery time is independent of the star formation efficiency and treat it as a free parameter.

Driven by the requirements of the large-scale 21-cm simulation (Section 6.3), we calculate $f_{\rm II}$ in cubic sub-volumes of 3 Mpc side length, which we will refer to as *pixels* for the remainder of the text. These pixels correspond to the resolution elements of the large-scale 21-cm simulation. As the box has a side length $16\,{\rm Mpc}\,h^{-1} = 23.52\,{\rm Mpc}$, $7^3 = 343$ pixels can be fit into the box. However, there is an arbitrary choice of placement of the origin of this grid. Therefore, we start the grid at 0,1 and 2 Mpc from the (0,0,0) corner of the N-body simulations along each axis, which leads to 27 grids with a total of 9261 pixels. While this results in a larger range of overdensities and reduces the systematic effect of the arbitrary grid-placement, it introduces a degree of correlation between the pixels. This is an acceptable trade-off, as we do not rely on the pixels being statistically independent in our analysis.

We find that, apart from the obvious dependence on redshift that stems from the growth of structure, the Pop II fraction depends on the critical virial temperature

$T_{\rm crit}$ as well as on the local overdensity δ defined as

$$\delta = \frac{\rho - \langle\rho\rangle}{\langle\rho\rangle}, \tag{6.4}$$

where ρ is the matter density (here averaged over the size of the pixel) and $\langle\rho\rangle$ is the mean cosmic density calculated across the whole box. In the hierarchical picture of structure formation, such as we adopt here, star formation in overdense regions will happen earlier than in underdense regions. Consequently, we expect the transition between Pop III and Pop II star formation to happen in overdense regions first. Since on the scale of individual pixels the overdensity evolves linearly for the redshift range considered here, we use the density field at $z = 40$ as a parameter for fitting (see Eq. 6.7). We compute the overdensitiy within each pixel from the initial conditions and rescale them to $z = 40$ using the linear relation

$$\delta_{40} = \delta \left(\frac{z_{\rm ini} + 1}{41} \right). \tag{6.5}$$

In Fig. 6.2 we present the distribution of overdensities of all the 9261 pixels. We also show the best-fitting Gaussian distribution

$$f_{\rm G}(\delta_{40}, A, \sigma) = N \, \exp\left(-\frac{\delta_{40}^2}{2\sigma^2} \right) \tag{6.6}$$

where N is a normalization parameter and $\sigma = 0.065$ is the best-fitting standard deviation. We verified with a Kolmogorov-Smirnov test that despite the visible asymmetry in the distribution of overdensities, the fitted distribution is consistent with the data from the N-body simulation.

Next, we fit the following 7-parameter function to the simulated Pop II fraction:

$$f_{\rm II} = \begin{cases} F(z, \delta_{40}, T_3) & \text{if } 0 \leq F(z, \delta_{40}, T_3) \leq 1, \\ 1 & \text{if } F(z, \delta_{40}, T_3) > 1, \\ 0 & \text{if } F(z, \delta_{40}, T_3) < 0. \end{cases} \tag{6.7}$$

We explicitly impose the physical limits that the Pop II fraction should be between 0 and 1. $F(z, \delta_{40}, T_3)$ is a function depending on the redshift z, the local overdensity averaged over the size of the pixel and normalized to redshift $z = 40$, δ_{40}, and the critical virial temperature for star formation expressed as $T_3 = \log_{10}(T_{\rm crit}) - 3$. We

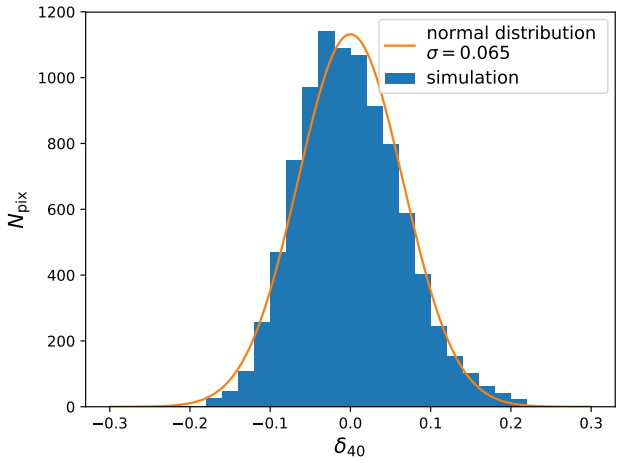

Figure 6.2: Distribution of rescaled overdensities for all 9261 pixels. The best-fitting Gaussian distribution is shown with an orange line. Despite the slight asymmetry, the distribution is statistically consistent with the Gaussian model.

chose the functional form

$$F(z, \delta_{40}, T_3) = F_0 + A \arctan\left(\frac{z_0(\delta_{40}, T_3) - z}{\Delta z}\right). \tag{6.8}$$

Here

$$z_0(\delta_{40}, T_3) = a_2 - a_1 T_3 - (a_3 T_3 + a_4)\delta_{40} \tag{6.9}$$

is the redshift of the Pop III-Pop II transition and Δz is the duration of the transition in units of redshift. Defined in such a way, the transition redshift marks the inflection point in the evolution of the Pop II fraction (rather than e.g. the half-way point). For our data we find that, typically, at z_0 the Pop II fraction is close to 40 per cent. For convenience, we additionally define a characteristic transition redshift as

$$z_{\rm t} = z_0(T_{\rm crit} = 2200\,{\rm K}, \delta_{40} = 0), \tag{6.10}$$

which is the transition redshift at mean cosmic density for a typical critical virial temperature. This characterstic transition redshift is not used in the further analysis, and we merely include it to give readers an indication for the redshift at which the transition occurs in a typical case.

We chose the basic functional form in Eq. 6.8 because the arctan function turned out to be an excellent fit for the redshift dependence of $f_{\rm II}$ at fixed $T_{\rm crit}$ and δ_{40} found in our simulations. We then added higher order terms in T_3 and δ_{40} until

it was possible to fit $f_{\rm II}$ everywhere in the three-dimensional parameter space of redshift, $T_{\rm crit}$ and δ_{40}. The free parameters in this function are F_0, A, Δz, a_1, a_2, a_3 and a_4. The results of this fitting procedure are discussed below.

There are already several haloes with $T_{\rm vir} > 2000\,{\rm K}$ at the earliest time-step of the merger trees (around $z \approx 30$). This leads to an instantaneous burst of Pop III formation in the first time-step for models with low $T_{\rm crit}$ and therefore to a jump in the Pop II fraction exactly one recovery time later. This initial jump is a numerical artifact and we therefore exclude the time-steps smaller than one recovery time since the first snap-shot from our fits.

We show an example of the Pop II fraction for a critical virial temperature of $T_{\rm crit} = 2200\,{\rm K}$ in Fig. 6.3 for the three recovery times. We chose this particular virial temperature as an example because it has been found to be a suitable value for the first collapse of mini-haloes by Hummel et al. (2012) and because around $z \approx 20$ it results in a similar mass-threshold as found by Schauer et al. (2019a) for moderate streaming velocities. Overall we can see that these fits represent the data well. As anticipated, the transition occurs earlier in regions with high overdensities. There is significant noise in the low-density pixels at high redshifts: as a result of small-number statistics, there is more noise in underdense regions, because they contain fewer haloes. As the low density pixels only contain a few haloes at these redshifts, the Pop II fraction changes very significantly with each single halo that transits to metal-enriched star formation. We also find that quicker recovery times show more scatter because Pop II star formation occurs at a time when there are fewer star-forming haloes overall. We present more detailed residuals of the fits in the space of z, δ and $T_{\rm crit}$ in Appendix 6.7.3.

The best-fitting parameters for the fast, the intermediate and the slow transition models are presented in Table 6.1. The characteristic transition redshift for $T_{\rm crit} = 2200\,{\rm K}$ ranges from $z_{\rm t} \approx 25$ in the fast case down to $z \approx 14$ in the slow case. We can also see that the transition at larger recovery times occurs over a shorter redshift interval Δz. However, this shortening of the transition period is only an effect of a similar redshift interval corresponding to more physical time at lower redshifts. The duration of the transition in physical time at the characterstic transition redshift $z_{\rm t}$ is $\Delta t \approx 30\,{\rm Myr}$ for the fast, $\Delta t \approx 72\,{\rm Myr}$ for the intermediate and $\Delta t \approx 114\,{\rm Myr}$ for the slow transition.

As a consistency check, we estimate the redshift at which the transition from metal-free to metal-enriched star formation occurs in cosmological simulations from the First Billion Years project (FiBY Johnson et al., 2013), the Pop III Legacy (P3L

Jaacks et al., 2019) and the *Renaissance* simulations (Xu et al., 2016a,c). The latter is a set of three simulations at different over-densities of $\delta_{40} = (0.27, 0.03, -0.06)$, which are referred to as 'rarepeak', 'normal' and 'void'. For all these simulations, we integrate the SFRs and find the redshift at which exactly 50 per cent of all the stars formed up to that time are metal-free. While this redshift is a marker of the transition to metal-enriched star formation, it is based on SFRs, rather than the halo properties. Thus, it does not have the same definition as our transition redshift defined in Eq. (6.9). To emphasize this difference we refer to the redshift at which 50 per cent of stars formed are metal-free as 'redshift of equality', rather than as transition redshift. Although the redshift of equality and the transition redshift have different definitions, they characterize the same physical process and, thus, are expected to be similar in value. We do not directly compute the transition redshift as we define it in Eq. (6.9) from the simulations. This would require a detailed analysis that goes beyond the scope of this project. We also do not calculate the redshift of equality for the semi-analytical model, as it would introduce dependencies on the star formation efficiencies, which we prefer to avoid. The comparison is therefore qualitative in nature. The redshifts of equality are $z \approx 14$ in FiBY, $z \approx 22.3$ in P3L and $z \approx 25$, 21.5, and 21 in *Renaissance* for their 'rarepeak', 'normal' and 'void' simulations respectively. In all these simulations, star formation predominantly occurs in haloes with a mass of $M_{\rm vir} \gtrsim 10^7\,{\rm M}_\odot$. At a transition redshift around $z \approx 16$ this corresponds to a critical virial temperature of $T_{\rm crit} = 8000\,{\rm K}$ (i.e., $T_3 = 0.9$) and we, therefore, compare the redshifts of equality in the simulations with the fitted transition redshift for this critical virial temperature, i.e., $z_0(T_3 = 0.9\,{\rm K})$ according to eq. (6.9). We show the transition redshift for a range of different overdensities δ_{40}.

The comparison is presented in Fig. 6.4. We find that, despite the large scatter, the redshifts of equality from the simulations are in a broad agreement with the predictions of our model. The transition redshift from FiBY is close to our z_0 in the case of the long recovery time (slow transition), while the ones from the P3L and *Renaissance* simulations fall between the fast and the intermediate models. The change in redshift of equality as function of overdensity seen in the *Renaissance* simulations is similar to our model predictions. We note that the simulations from all three mentioned projects have completely independent implementations and vary in their setup, assumptions and employed methods. It is not clear which of the assumptions cause the large variation in the redshifts of equality found in these simulations. However, the fact that the span of transition redshifts computed from

Model	Fast	Inter.	Slow
$t_{\rm recov}$ (Myr)	10	30	100
F_0	0.378	0.442	0.452
A	0.484	0.481	0.499
Δz	5.11	5.13	3.62
a_1	3.74	2.33	1.48
a_2	26	20.1	14.2
a_3	-8.59	-3.98	-1.45
a_4	-13	-10.3	-8.47
$z_{\rm t}$	24.7	19.3	13.7

Table 6.1: Best-fitting parameters of the analytic expression of the Pop II fraction. The fitting function is defined in Eq (6.7). We additionally show the characteristic transition redshift $z_{\rm t}$, which is z_0 (see Eq. 6.9) at $T_{\rm crit} = 2200\,{\rm K}$ and $\delta_{40} = 0$.

our models covers the variety of the redshifts of equality found in these diverse simulations indicates that our approach brackets cases realized in state-of-the-art cosmological simulations.

6.3 Large-scale simulations of the 21-cm signal

The 21-cm brightness temperature is given by

$$T_{21} = \frac{T_{\rm S} - T_{\rm CMB}}{1+z}\left(1 - e^{-\tau_{21}}\right), \tag{6.11}$$

where $T_{\rm S}$ is the spin temperature (which corresponds to the excitation temperature of the hydrogen ground state), τ_{21} is the 21-cm optical depth (which itself depends on the spin temperature, Madau et al., 1997), and $T_{\rm CMB} = 2.725(1+z)$ K is the temperature of the cosmic microwave background (CMB) radiation[5]. The 21-cm signal can only be seen when the spin temperature is driven away from the background radiation temperature. During Cosmic Dawn and the EoR this is enabled through the subtle Wouthuysen and Field effect (WF, Wouthuysen, 1952, Field, 1958), in which the absorption and re-emission of Ly-α photons by hydrogen atoms couple the spin temperature to the kinetic temperature of the gas. The source of these Ly-α photons are stars in the first galaxies. After the coupling between the spin temperature and the gas temperature is established, the 21-cm signal is expected to be seen in absorption. This is expected because the gas temperature is thought to be

[5]In the presence of high redshift radio sources this temperature is replaced by the total radiation temperature at the wavelength of the 21 cm line (Feng & Holder, 2018, Reis et al., 2020b).

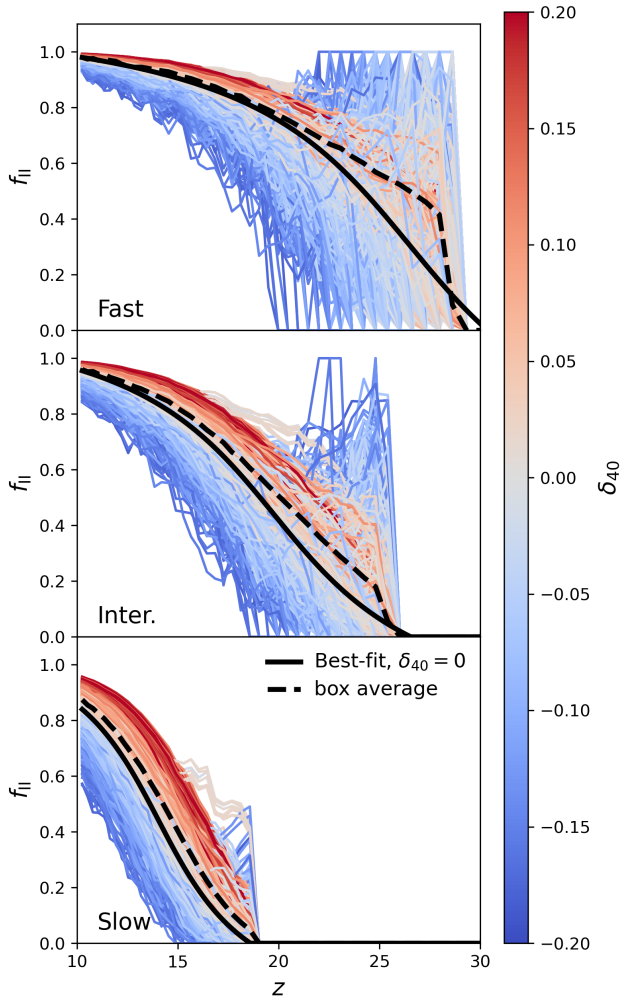

Figure 6.3: Example Pop II fraction as a function of overdensity (colorbar) and redshift for a critical virial temperature of $T_{\rm crit} = 2200\,{\rm K}$ for all three recovery times: fast (top), intermediate (middle) and slow (bottom). We also show the Pop II fraction of the entire simulated region (dashed black line) and the best-fitting curve at $\delta_{40} = 0$ (black). Note that the average Pop II fraction is not equal to the Pop II fraction at average density. The noise in the low-density pixels at high redshift is due to low number statistics.

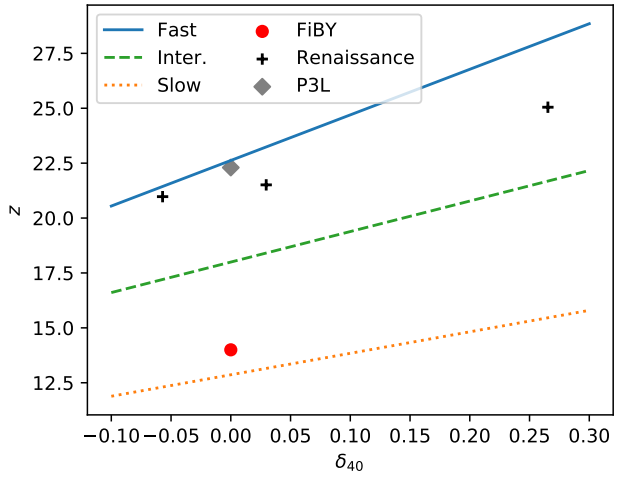

Figure 6.4: Qualitative comparison between our fitted transition redshift z_0 (defined in Eq. 6.9, and calculated for $T_{\rm crit} = 8000\,{\rm K}$) and the redshifts of equality (see text) from FiBY, the Pop III Legacy (P3L) and the *Renaissance* simulations as a function of the large-scale overdensity at $z = 40$, δ_{40}. The comparison is qualitative owing to the discrepancy in the definitions of the transition redshifts.

lower than the background radiation temperature at this stage (since after thermal decoupling, the gas cooled faster than the radiation). Radiation from galaxies can also heat the gas (via X-ray and Ly-α heating, e.g., Madau et al., 1997, Chuzhoy & Shapiro, 2007, Reis et al., 2021), potentially resulting in a 21-cm signal seen in emission, and ionize the gas leading to the disappearance of the 21-cm signal from the inter-galactic medium (IGM). The 21-cm signal is predicted to be non-uniform with fluctuations originating from several sources including non-uniform hydrogen density and velocity as well as fluctuating radiative backgrounds (e.g. Visbal et al., 2012, Fialkov et al., 2014, Cohen et al., 2018, Reis et al., 2021).

Although Cosmic Dawn is unconstrained by observations, it is generally thought that at the onset of star formation the 21-cm signal is dominated by the effects of Ly-α physics as these photons are very efficient in coupling the gas. For instance, exploring a large set of 21-cm simulations with variable astrophysical parameters, Cohen et al. (2017, 2018) found that the redshift of Ly-α coupling can be anywhere between $z \sim 35$ and 15 depending on the properties of star-forming haloes. X-ray heating becomes relevant later ($z \lesssim 20$, Cohen et al., 2017, 2018) owing to the fact that it takes time for the first population of X-ray sources (such as X-ray binaries, Fragos et al., 2013) to emerge. The impact of reionization on the 21-cm signal becomes apparent only at relatively late times ($z \lesssim 15$ in Cohen et al., 2017, 2018)

with the appearance of massive galaxies which are efficient in ionizing the gas (e.g., Park et al., 2020). It is, thus, expected that the Pop III-Pop II transition explored in this paper will mostly affect the 21-cm signal from the era of Ly-α coupling. Therefore, for simplicity, we will ignore the impact of X-ray and ionizing photons in this work. The only heating/cooling mechanisms that might affect the temperature of the IGM in the absence of X-ray and ionizing photons are cooling due to the expansion of the Universe, heating by the Ly-α photons (Chen & Miralda-Escudé, 2004, Chuzhoy & Shapiro, 2007, Reis et al., 2021) and the CMB (Venumadhav et al., 2018), as well as the impact of structure formation. All of these effects are included in the simulation.

We use our own semi-numerical code to calculate the 21-cm signal (e.g., Visbal et al., 2012, Fialkov et al., 2014, Cohen et al., 2017, Fialkov & Barkana, 2019, Reis et al., 2020a, 2021). The simulation size is 384^3 Mpc^3 and resolution is 3 comoving Mpc. The outputs of the simulation are cubes of the 21-cm brightness temperature at each redshift. From these we calculate the global signal and the spherically averaged power spectrum. The input of the simulation is a realization of the initial density and velocity fields (calculated using publicly available code `CAMB`, Lewis et al., 2000). The density and velocity fields are then evolved using linear perturbation theory. To calculate the population of dark matter haloes given the density field we use the hybrid approach of Barkana & Loeb (2004) which combines the previous models of Press & Schechter (1974) and Sheth & Tormen (1999). In the simulation, the minimum halo mass for star formation is parametrized by the circular velocity V_c which is related to $T_{\rm crit}$ by

$$T_{\rm crit} = \frac{\mu m_p V_c^2}{2k_{\rm B}} = 7300\,{\rm K}\left(\frac{V_c}{10\,{\rm km\,s^{-1}}}\right)^2, \tag{6.12}$$

where μ is the mean molecular weight, m_p is the proton mass, and $k_{\rm B}$ is the Boltzmann constant. Note that the value of μ depends on the ionization fraction of the gas. Here, we assume neutral primordial gas for which $\mu = 1.22$. Our simulation includes the effect of the relative velocity between dark matter and gas (following the prescription in Fialkov et al., 2012, Visbal et al., 2012), Lyman-Werner feedback (as described in Fialkov et al., 2013) and photoheating feedback (from Cohen et al., 2016) on the minimum halo mass for star formation.

Haloes accrete gas and convert it into stars with star formation efficiency which is constant (denoted by f_*) for halo masses above the atomic cooling threshold but drops as the logarithm of mass at lower masses (Cohen et al., 2017). To relate

the stellar mass to the radiation produced in the Ly-α line and the LW bands we use our fiducial model for Pop III and Pop II emissivities based on the results of Barkana & Loeb (2005). Our Pop II model is calibrated to the locally measured Scalo IMF (Scalo, 1998) with a metallicity of 5% of the solar value. Pop III stars are all assumed to be 100 solar mass, which was the prediction of the early Pop III simulations by Abel et al. (2002). Stellar spectra are approximated by a series of power law curves (a separate power law for every pair of consecutive levels of atomic hydrogen).

6.3.1 Implementing the Pop III - Pop II transition in 21-cm simulations

Previously, in our 21-cm simulations Pop III and Pop II stars were implemented on equal footing, with the total mass in stars calculated using the accreted gas mass and assuming certain star formation efficiency (e.g. see Cohen et al., 2020, for details). The only difference between Pop III and Pop II stemmed from the different stellar emissivities. Only one type of stars (either Pop III or Pop II) could be selected. In this work we differentiate between Pop III and Pop II star-forming haloes using the results of Section 6.2.3 and change the prescription for the calculation of the stellar mass in Pop III forming haloes (following the single-burst approximation). As before, each type of stars produces radiation according to their respective emissivities. The contributions of Pop III and Pop II to the evolving and fluctuating radiative backgrounds that drive the 21-cm signal are computed separately and then added up.

The total Pop II stellar mass in each pixel of the 21-cm simulation box is computed by multiplying the total mass in stars, calculated as previously using the accreted gas mass and assuming a star formation efficiency $f_{*,\mathrm{II}}$, by the fraction of haloes that actually form Pop II stars, f_{II}. Because the Pop II fraction is a function of redshift, T_{crit} (related to V_c by Eq. 6.12 and affected by the non-uniform LW feedback and streaming velocities) and local overdensity, the Pop II content is inhomogeneous and f_{II} varies across the simulation box. Examples of the mean value and scatter in f_{II} calculated from the 21-cm simulations are shown in the top panel of Fig. 6.5 for an astrophysical scenario with $V_c = 5.4$ km s^{-1} (corresponding to $T_{\mathrm{crit}} = 2200\,\mathrm{K}$) and for the three cases of Pop III-Pop II transition (fast, intermediate, and slow).

To calculate the contribution of Pop III star forming haloes to star formation in every pixel and at a given redshift we find the number of haloes above the star

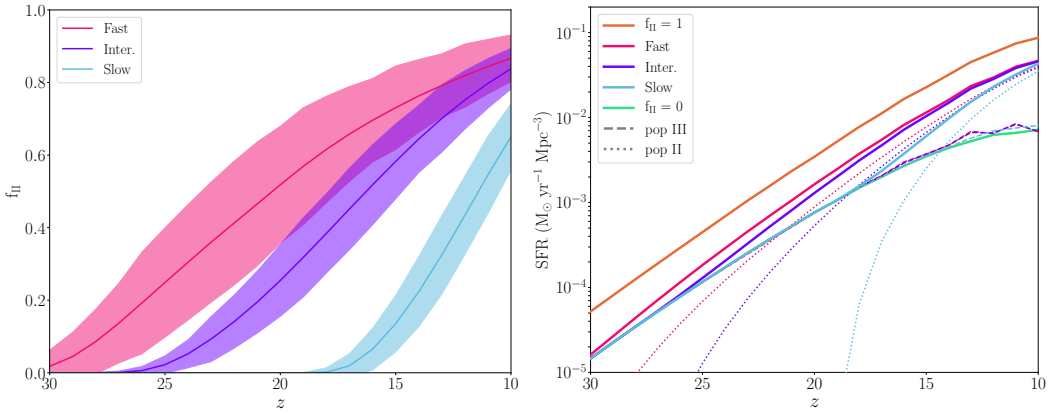

Figure 6.5: Left: The mean Pop II fraction $f_{\rm II}$ (solid lines) calculated from the 21-cm simulations shown for $V_c = 5.4$ km s^{-1} for the three time-delays: fast (magenta), intermediate (purple), and slow (cyan). The shaded regions show the corresponding standard deviation in $f_{\rm II}$ calculated over one simulation box of 384^3 Mpc^3 at the resolution corresponding to the pixel size of 3^3 Mpc^3. **right:** The SFR shown for $V_c = 5.4$ km s^{-1}, and $f_{*,\rm III} = f_{*,\rm II} = 0.05$ and the three cases of star formation transition: fast (magenta), intermediate (purple), and slow (blue). We show the total result (solid) as well as the individual contributions of Pop III (dashed) and Pop II (dotted) stars. We also show the case with Pop III stars only (denoted as $f_{\rm II} = 0$, turquoise) and the full Pop II stars case ($f_{\rm II} = 1$, orange).

formation threshold ($M_{\rm crit}$) that have formed within an interval of time equal to the lifetime of Pop III stars, $t^{\rm popIII}_{\rm lifetime}$. We then assume that each such halo produces

$$M_{*,\rm III} = f_{*,\rm III} \frac{\Omega_{\rm b}}{\Omega_{\rm m}} M_{\rm crit} \tag{6.13}$$

of Pop III stars (in agreement with Eq. 6.2). Note that we cannot simply use $1 - f_{\rm II}$ to calculate the Pop III contribution since $1 - f_{\rm II}$ also includes inactive haloes that have already stopped forming Pop III stars but have not yet started forming Pop II. We also note that for the same values of $f_{*,\rm II}$ and $f_{*,\rm III}$, Pop III formation is a less efficient process compared to the formation of Pop II stars. This is because a halo of mass M forming Pop III stars will generate total stellar mass given by Eq. 6.13, which is smaller than the stellar mass in Pop II stars, $f_{*,\rm II}\,(\Omega_{\rm b}/\Omega_{\rm m})\,M$, that the same halo can host.

The bottom panel of Fig. 6.5 shows the box-averaged contributions of Pop III and Pop II stars to the total SFR for slow, intermediate and fast transition. Here for simplicity we assume $f_{*,\rm II} = f_{*,\rm III} = 0.05$. In addition, we show the cases with Pop III stars only (referred to as $f_{\rm II} = 0$) and the full Pop II stars case ($f_{\rm II} = 1$) where we assume that Pop II stars form from the start, with no recovery delay, and

there is no episode of Pop III star formation.

We see that the contribution from Pop III to the total SFR is the similar (up to a small discrepancy explained by the difference in $M_{\rm crit}$, which is a result of the variation in the LW feedback driven by the difference in the total SFR) in all transition scenarios. The scenarios differ in the contribution from Pop II: Owing to the rapid early rise in the number of Pop II star-forming haloes in the case of the intermediate and fast transitions, the total SFR is driven by the metal-enriched population through the most part of cosmic history. On the contrary, in the slow transition case primordial stars dominate the SFR (and, thus, will drive the 21-cm signal, as we discuss later) all the way down to $z \sim 17$. At lower redshifts, the rapid increase in the number of Pop II star forming haloes in this case results in a fast growth of the SFR.

Finally, we note that the implementation of this model relies on the assumption that the total number of haloes above the critical mass is a good approximation for the total number of haloes that ever formed Pop III stars. This is justified if the number of haloes that ever crossed the critical mass threshold is similar to the number of haloes that are above the critical mass threshold, i.e., that haloes mostly grow via smooth accretion, while mergers between haloes above the critical mass are rare. To ensure that this assumption is fulfilled we compare the total number of haloes above $T_{\rm crit} = 2200\,{\rm K}$ as a function of redshift to the total number of haloes that ever reached $T_{\rm crit} = 2200\,{\rm K}$ until that redshift using the results of the N-body simulations from Section 6.2.1 (see Fig. 6.6). Indeed, we can see that mergers do not affect the halo numbers above $T_{\rm crit}$ strongly for $z > 15$, where our Pop III star formation model is most important. At lower redshifts the expected 21-cm signal is dominated by Pop II star formation, which is only dependent on the HMF and not on their merger histories. However, we note that the discrepancy reaches about a factor of two at redshift $z = 11$, indicating that mergers should not be neglected at lower redshifts.

6.4 Effect of Pop III - Pop II transition on the 21-cm signal from Cosmic Dawn

In the absence of X-ray heating sources, the 21-cm signal from Cosmic Dawn is largely driven by Ly-α photons and, therefore, is tightly linked to the SFR. In this section we explore the impact of the Pop III-Pop II transition on the characteristic features of the 21-cm signal, including the typical deep absorption trough in the

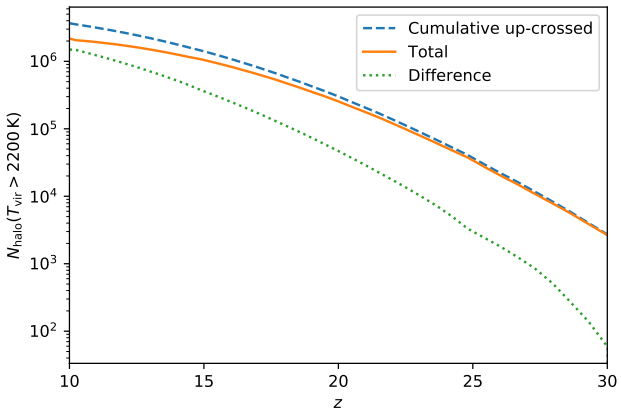

Figure 6.6: Total number of haloes above a critical virial temperature of $T_{\rm crit} = 2200\,{\rm K}$ as a function of redshift (orange solid line) compared to the total number that ever exceeded $T_{\rm crit}$ until that redshift (blue solid line) and the difference between the two (green). If there were no mergers of haloes above $M_{\rm crit}$ the two lines should be the same and the difference should be zero.

global signal and the peak in the power spectrum imprinted by the inhomogeneous Ly-α coupling and Ly-α heating.

Fig. 6.7 shows the redshift dependence of both the global 21-cm signal and its power spectrum calculated for the same astrophysical scenarios that were used to demonstrate the effect of the population transition on the SFR (shown in Fig. 6.5). In addition, here we plot the two limiting cases, $f_{\rm II} = 1$ (full Pop II case) and $f_{\rm II} = 0$ (only Pop III stars). Echoing the growth of SFR with time, the more realistic 21-cm signals which include the Pop III-Pop II transition evolve faster compared to the reference case with Pop III stars only. The higher SFR of the realistic models is manifested by the shift to higher redshifts of the absorption feature in the global signal and the earlier emergence of the corresponding peak in the power spectrum. The resulting global signal is stronger with a deeper and narrower absorption trough (the former is due to the more efficient Ly-α coupling and the latter is a manifestation of the more efficient Ly-α heating compared to the Pop III-only case). Correspondingly, the peak in the power spectrum is higher (although this is a small effect) and narrower. On the other hand, compared to the $f_{\rm II} = 1$ case, the realistic scenarios, which inevitably include an initial phase of Pop III star formation, evolve slower.

In addition to the general impact of the SFR on the timing of the signal, the character of the transition between the two stellar populations is reflected in the

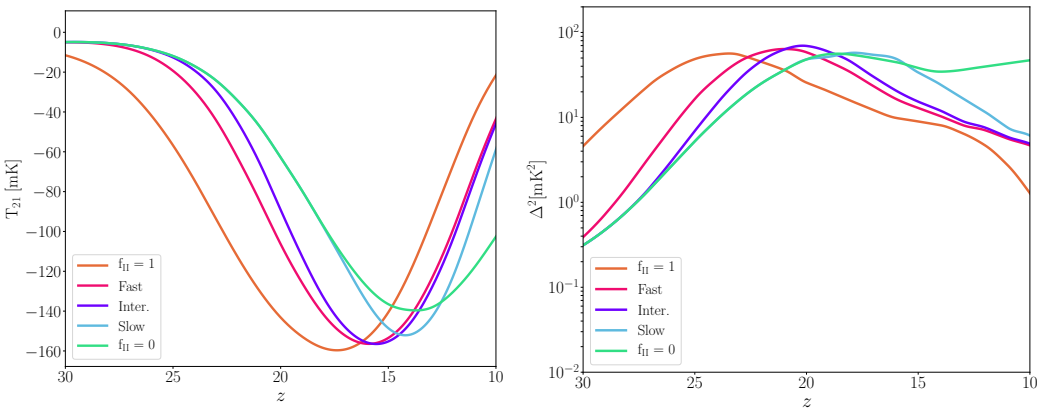

Figure 6.7: Examples of the effect of the transition to Pop II star formation on the 21-cm signal. **left:** The global signal. **right:** The power spectrum at k = 0.1 Mpc^{-1}. We show a model with $V_c = 5.4$ kms^{-1} and $f_{*,\rm III} = f_{*,\rm II} = 0.05$ for the three scenarios with fast (magenta), intermediate (purple), and slow (blue) transition. We also show two reference models, one with $f_{\rm II} = 1$ (orange) and one with $f_{\rm II} = 0$ (turquoise).

shape of the 21-cm signal. In all the realistic scenarios the initial stage of the process of Ly-α coupling is dominated by Pop III star formation, as is evident from the overlapping high-redshift parts of the two 21-cm signals corresponding to the scenario with $f_{\rm II} = 0$ and the slow transition model. However, the onset of Pop II star formation, accompanied by a boost in the number of Ly-α photons, leads to a divergence of these two signals with a Pop III-only case lagging behind. The rapid growth of the enriched population results in a steepening of the 21-cm signal (seen both in the global signal and the power spectrum), which is a potentially testable prediction. Similar, but much stronger effect of the emerging Pop II formation is seen in the signals corresponding to the intermediate and fast transitions which deviate from the $f_{\rm II} = 0$ case very early on and are steeper than both $f_{\rm II} = 0$ and $f_{\rm II} = 1$ cases. In these scenarios the contribution of Pop II stars is important throughout the Cosmic Dawn and affects the 21-cm signal over a broad range of redhifts.

The signature of the Pop III-Pop II transition on the 21-cm signal is model-dependent and varies as a function of astrophysical parameters, as can be seen from the two additional cases shown in Fig. 6.8. The first scenario (top panels of Fig. 6.8) has the same critical temperature as our main model (from Fig. 6.7, also shown with faint dashed curves in Fig. 6.8 for comparison), but less efficient star formation with $f_{*,\rm III} = f_{*,\rm II} = 0.01$ compared to 0.05 in the main case. Because the redshift evolution of the number of Pop II forming haloes (determined by $f_{\rm II}$) is

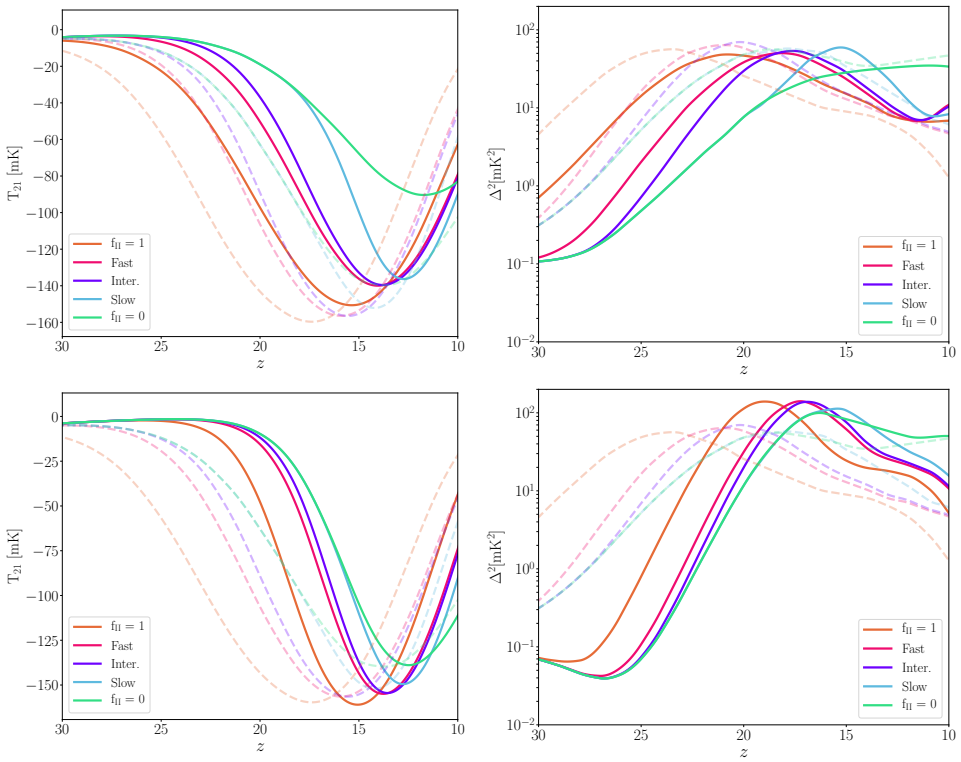

Figure 6.8: Global 21-cm signal (left) and the power spectrum (right) for different astrophysical parameters. Top: Same as Fig. 6.7 but for $f_{*,\rm III} = f_{*,\rm II} = 0.01$. Bottom: V_c of 35.5 km s^{-1} (corresponding to $T_{\rm crit} = 9.3 \times 10^4$ K) and $f_{*,\rm III} = f_{*,\rm II} = 0.1$. For comparison, we also show the curves from Fig. 6.7 (dashed).

independent of star formation efficiency, features of the 21-cm signal that depend on the properties of the Pop III-Pop II transition (such as the relative steepness of the signals and the redshift at which the slow transition curve diverges from the $f_{\rm II} = 0$ reference case) are the same as in our main case. On the other hand, the absolute strength of the Cosmic Dawn signal is mostly determined by the intensity of the Ly-α background and, therefore, directly depends on the values of $f_{*,\rm III}$ and $f_{*,\rm II}$. One major difference between the cases with low and high star formation efficiency is that in the former case the 21-cm signal evolves slower, and so when it peaks there are more Pop II forming haloes compared to the latter case. This example shows that for a fixed value of V_c the contribution of Pop III stars is more important in high f_* models, where major milestones in the evolution of the 21-cm signal occur at higher redshifts where there are more Pop III star forming haloes.

The final example that we consider here has a higher $T_{\rm crit} = 9.3 \times 10^4$ K (corresponding to V_c of 35.5 km s^{-1}) compared to our main setup as well as a higher star

formation efficiency $f_{*,\mathrm{III}} = f_{*,\mathrm{II}} = 0.1$ (bottom panels of Fig. 6.8). This model has a star formation threshold far above the atomic cooling limit, and is only considered as an extreme case. Even though the intensity of the global 21-cm signal is roughly the same in these models, the Pop III-Pop II transition happens much later (shifted by δz between two and six) for the models with $V_c = 35.5$ km s^{-1}. As a result, the related features such as the redshift at which the slow transition curve diverges from the $f_{\mathrm{II}} = 0$ reference case, are shifted to lower redshifts.

The approach presented in this paper provides a flexible basis to test the nature of the Pop III-Pop II transition using 21-cm observations. Because f_{II} is independent on star formation efficiency, it might be possible to measure the time-delay while marginalizing over the rest of the model parameters (in a similar way limits on astrophysical parameters were calculated, e.g. using early data of EDGES and LOFAR by Monsalve et al., 2019, Mondal et al., 2020). However, such analysis is out of the scope of this paper and we leave it for future work.

6.5 Discussion

6.5.1 Comparison to earlier works

Properties of Pop III stars have previously been shown to have an impact on the 21-cm signal (Cohen et al., 2016, Mirocha et al., 2018, Mebane et al., 2018, Tanaka et al., 2018, Tanaka & Hasegawa, 2021, Schauer et al., 2019b, Mebane et al., 2020). In these models the biggest factors in determining the 21-cm background are the star formation efficiencies and the IMF averaged radiation output of the first stars. These previous studies focus only on Pop III stars or introduce a very simple model for the transition. Here we expand this picture by quantifying the transition from Pop III to Pop II star formation based on a semi-analytical model motivated by numerical simulations. We show that the recovery time, which is determined by the efficacy of Pop III stellar feedback, has a distinctive imprint in the 21-cm background, affecting both the global signal and the fluctuations. We have seen in Section 6.2.3 that the range of characteristic redshifts at which the transition to Pop II star formation occurs in our model agrees with the results of cosmological simulations. A better understanding of how the recovery time arises will be key to interpreting upcoming 21-cm observations.

Here we briefly compare our model and results to the work of Mirocha et al. (2018), based on the method of Mebane et al. (2018), where the impact of Pop III-

Pop II transition on the global 21-cm signal was investigated[6]. The modelling of the transition presented here significantly differs from the one adopted by Mirocha et al. (2018). Most importantly, we assume that there is only one episode of Pop III star formation per halo, and that first SNe eject metal-enriched gas which re-collapses after a recovery time initiating the process of Pop II star formation. In contrast, the recovery times are not implemented directly in the prescription of Mebane et al. (2018), where two modes for the Pop III-Pop II transition are considered: an energy-based and a momentum-based prescription. These prescriptions compare the energy (or momentum) injected into a halo by the SNe to the energy (or momentum) required to remove gas from the halo, and expel gas and metals accordingly. In particular, if the halo is small enough all gas and metals will be removed. The halo then proceeds to accrete pristine gas. The transition to Pop II formation occurs if the gas-metallicity within the halo exceeds a certain threshold. Thus the transition is governed by the halo's ability to retain SN ejecta which is computed from the escape velocity (or binding energy) of the halo. This assumption results in a rapid succession of up to $\mathcal{O}(10)$ episodes of Pop III star formation in the same halo. To our knowledge, this behaviour is not reflected in hydrodynamical simulations of Pop III SNe (Ritter et al., 2012, 2015, 2016, Jeon et al., 2014, Smith et al., 2015, Chiaki et al., 2016). In these simulations minihaloes retain enough metals to form Pop II stars shortly after the first SN explosions. The limiting factor is that very energetic SNe may evacuate minihaloes to such a degree that a next episode of star formation could be delayed by up to or above 100 Myr (Whalen et al., 2008, corresponding to our longest recovery time). However, we are unaware of any hydrodynamical simulations in which the stars forming in such a context would be metal-free.

We find that the redshift of the Pop III to Pop II transition from their energy-based model matches well with our results. The momentum-based model, which is also used for further predictions by Mebane et al. (2020), produces much higher transition redshifts ($z_\mathrm{t} > 30$) than what is found in hydrodynamical simulations ($13 < z_\mathrm{t} < 25$ Johnson et al., 2013, Xu et al., 2016a,c, Jaacks et al., 2019).

6.5.2 Measuring the recovery time with the 21-cm signal

As we have shown in this work, the slow Pop III-Pop II transition mode leads to a 21-cm signal that is very different from either the intermediate or the fast transitions. In this mode, the early onset of the signal is dominated by Pop III stars for a significant

[6] To our knowledge, ours is the first work to explore the impact of the transition on the fluctuations of the 21-cm signal.

part of cosmic history, which is evident from the corresponding Cosmic Dawn signal that closely follows the Pop III-only case. This slow transition, with a recovery time of 100 Myr is associated with massive (above $100\,M_\odot$) Pop III stars and their very energetic pair-instability SNe (Jeon et al., 2014, Chiaki et al., 2016) or with many SNe in the same halo (Ritter et al., 2015). In such models the Ly-α coupling and heating happen later, typical 21-cm signals are shifted to lower redshifts (higher frequencies) compared to the models with fast/intermediate transition, and the late onset of Pop II formation leads to a characteristic steepening of the signal. This dependence on the recovery time could allow us to indirectly measure this parameter as well as constrain the primordial IMF and star formation efficiency using the 21-cm data from either radiometers or interferometers. We note that the Pop III IMF also affects the radiation output of the first stars, both in terms of total emission power and in terms of the spectral energy distribution. Investigating these effects on the 21-cm signal will be subject to a follow-up study (Gessey-Jones et al. in prep.).

If the EDGES detection is confirmed to be a cosmological 21-cm signal, its timing at $z \sim 17$ (Bowman et al., 2018) implies early star formation. Models consistent with this signal are characterized by efficient emission of Ly-α photons as well as a strong X-ray background at high redshifts (e.g. Schauer et al., 2019b, Fialkov et al., 2018, Fialkov & Barkana, 2019, Mirocha & Furlanetto, 2019, Reis et al., 2020b), which is unlikely in the case of the slow Pop III-Pop II transition that we considered here, but could be easily achieved in the scenarios with either a fast or an intermediate transition. This would in turn indicate that only a single or very few SNe per halo took place, and that they had relatively low explosion energies.

6.5.3 Future work

As the transition from Pop III to Pop II star formation is predicted to happen at the high redshifts of Cosmic Dawn, we focus here on the signature of sources emitting radiation in Ly-α and LW bands. While the evolving metallicity will also affect the luminosity of X-ray binaries formed as the first population of stars dies (Fragos et al., 2013), we do not consider this effect here, leaving the self-consistent modelling of the X-ray signature to future work. The EoR is predominantly driven by later-time evolved galaxies which are expected to be metal-rich and, therefore, we do not expect the Pop III-Pop II transition to have an important effect on reionization apart from a minor effect on the high-redhsift tail that can be constrained using the CMB polarization data (e.g. Heinrich & Hu, 2018). With the consistent inclusion

of the X-ray and UV sources, we will be able to constrain the delay-time in the formation of Pop II stars from data.

6.6 Summary

In this work we considered for the first time the effect of the transition from primordial star formation (Pop III) to the first generation of metal-enriched stars (Pop II) on the inhomogeneous 21-cm signal from Cosmic Dawn. Stars directly affect the 21-cm signal by emitting ultraviolet radiation and, therefore, the change in the mode of star formation will be imprinted in the shape of the 21-cm signal. Because the duration and timing of this transition is linked to the stellar IMF and the typical mass of the first star-forming haloes, the 21-cm signal from Cosmic Dawn can be used to constrain these properties.

We model the transition using the semi-analytical code a-sloth and compare signatures of fast, intermediate and slow transitions (with recovery times of 10, 30 and 100 Myr respectively) in the 21-cm signal. We find that the fast and intermediate transitions, linked to low efficiency of Pop III formation, weak feedback and a quick recovery after the first SNe, lead to a steeper 21-cm signal compared to all the rest of the explored scenarios. Such models are more likely to explain the tentative 21-cm signal reported by the EDGES collaboration, compared to the slow Pop III-Pop II transition characteristic of the case in which stars form in small haloes and/or multiple SNe explode in each halo.

For the interpretation of observed 21-cm absorption signals it will be of vital importance to understand the connection between the properties of Pop III stars, their birth haloes and the recovery times. Once there is a reliable quantification of this connection, measurements of the Cosmic Dawn 21-cm signal with either radiometers or interferometers can be used to gain new constraints on the formation of the first stars and their environments.

6.7 Additions:

6.7.1 a-sloth model with feedback

Both chemical and radiative feedback crucially depend on the rate of Pop III and Pop II star formation in each modelled halo, and therefore come with many more free parameters. We do not study the dependence of the resulting 21 cm signal on all of these parameters, but merely aim to test the difference between having and not

Model	Fast	Inter.	Slow
$t_{\rm recov}$ (Myr)	10	30	100
F_0	0.382	0.447	0.472
A	0.493	0.474	0.487
Δz	4.96	4.64	2.96
a_1	4.16	2.97	2.03
a_2	26.6	21.2	15.3
a_3	-8.41	-3.26	-1
a_4	-14.5	-12.7	-10.4

Table 6.2: As Table 6.1 but for modelling in full physics mode.

having small-scale feedback. Therefore, we only test one set of parameters, which we adopt from Tarumi et al. (2020), who calibrated the high-redshift star formation module of A-SLOTH using the metallicity distribution function of the Milky Way and reproduce the stellar mass to halo mass ratio from Garrison-Kimmel et al. (2017).

Pop II star formation is implemented as a four-phase bathtub model with the baryonic matter in haloes cycling between hot and cold ISM, stars and outflows (see Tarumi et al., 2020, for details). The haloes can enrich nearby haloes with metals via outflows (Magg et al., 2018). Additionally, we model ionizing bubbles around the haloes with the implicit R-type ionization front scheme (Magg et al., 2018). We describe the numerical method used for deciding whether a halo is inside one of these ionized or enriched regions in Appendix 6.7.2.

We follow the same fitting procedure as in Section 6.2.3 to find the functional form of $f_{\rm II}$, the fraction of Pop II star forming haloes. The best-fitting parameters of this model are shown in Table 6.2. A comparison to Table 6.1 reveals that the differences caused by the additional feedback between the haloes is much smaller than the difference arising from the recovery time. In other words, at the high redshifts we are considering, how exactly ionizing radiation and SNe affect the immediate vicinity of the Pop III stars in the local halo has a bigger impact on the transition to metal-enriched star formation than their effect on the IGM. Therefore, and for the sake of simplicity, we use the semi-analytical model without external enrichment and ionization feedback to predict the 21-cm signature.

6.7.2 Numerical method for assigning feedback

Determining whether a halo is inside any of the ionized or enriched regions in the most simple implementation requires us to compute distances from the halo to the

centres of all bubbles and to compare the distance to the size of the bubble. As Visbal et al. (2020) pointed out, this leads to the cost of the computations scaling as $\propto N_{\rm source} N_{\rm halo} \propto V^2$, where V is the volume of the simulated region. In our case, for the lowest critical temperature and at redshift $z = 11$, we have 70 million haloes in the box, 4 million of which are star-forming. This would mean we would have to compute up to 280 trillion pairwise distances per time-step, which, on the computer we use would take a very long time[7] and make the parameter exploration we perform unfeasible. Visbal et al. (2020) solve this problem by looking at chemical and radiative feedback on a three-dimensional grid which is constructed via fast-fourier-transforms of radiation- and enrichment-fields. We address the issue with a tree-based approach:

Our aim is to reduce the number of distances we need to compute. In order to do this, we sort all actively star-forming haloes into an oct-tree structure. Each star-forming halo is assigned to the smallest node that fully encompasses the ionized and the enriched region around the halo. The tree is chosen such that it is larger than the simulated box and it has a maximum depth of 20 levels. In contrast to a classical oct-tree, such as the ones often used for calculating gravitational interactions in large N-body simulations, haloes are not associated with the parent node of the one they have been assigned to. When checking whether a halo is, e.g., enriched, it is sufficient to see whether it is enriched by any halo associated with every tree-node the target halo is inside of. This leads to a result that is exactly identical to testing every pairwise combination but uses substantially less computation time. For the whole simulation with $T_{\rm crit} = 1500$ K, the number of distances we need to compute is reduced by 99.95 per cent from 4×10^{15} to 2×10^{12}, and it runs in three hours on 40 cores. While this type of external feedback is not used in the main model and only enters in Section 6.7.1, it was developed for this work and will be used in a variety of future applications.

[7] We run these semi-analytical simulations on the 'fat' nodes of the BwForCluster MLS&WISO in Heidelberg. Each node has four Intel Xeon E5-4620v3 processors with a theoretical peak node performance of 320 GFLOP per second. If this performance was reached, computing and comparing the distances would take only one day. However, the task is, unless it is heavily optimized, memory-access limited. Each position and enriched and ionized radius would need to be loaded once per halo and time-step, taking at least one week if the theoretical maximum memory bandwidth of 272 GB per second were reached.

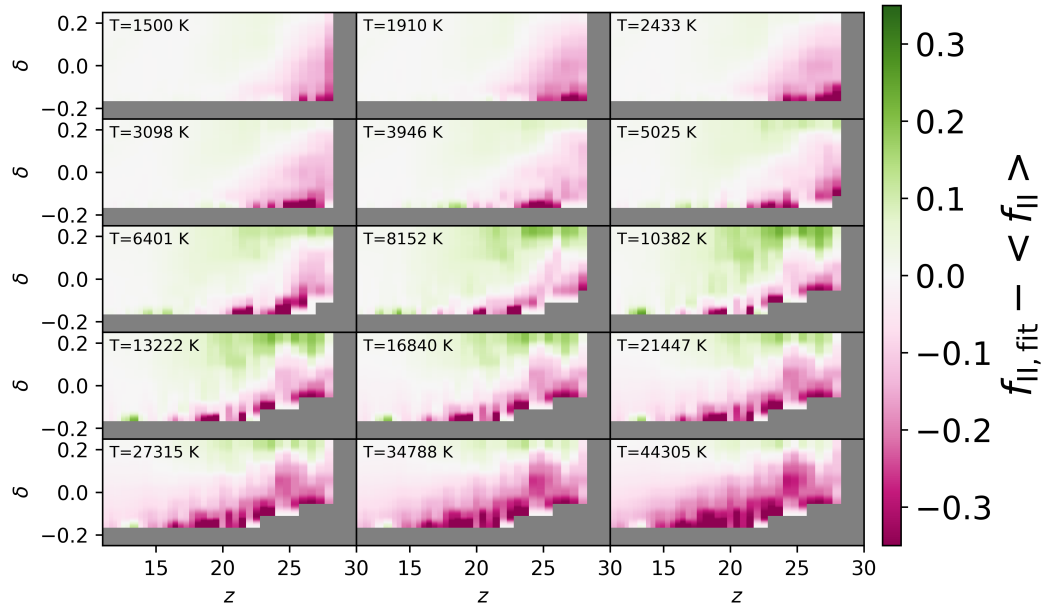

Figure 6.9: Residuals for the fit of the Pop II fraction for the slow transition. The area shaded in grey indicates no data or data that were excluded from the fits.

6.7.3 Fit residuals

In this Section we show the quality of fit for the Pop II fraction as discussed in Section 6.2.3. For easier representation we only show the residuals for every second critical temperature. Figs. 6.9, 6.10 and 6.11 show the residuals for the fast, intermediate and the slow transition respectively. As we excluded the data obtained during the first fall-back time from the fits, the slow transitions have larger areas without data.

Generally the fits work well, with residuals of less than 10 per cent in most areas. The difference between the different transition speeds is much larger than uncertainties introduced by the fitting procedure. The residuals are largest in areas with low over-densities at high redshifts. These are the areas with the fewest star-forming haloes, which means that low-number statistics have a big impact here. However, as these are relatively rare low-density regions with below-average star-forming activity, we do not expect these regions to have a strong impact on the observed global 21cm signal.

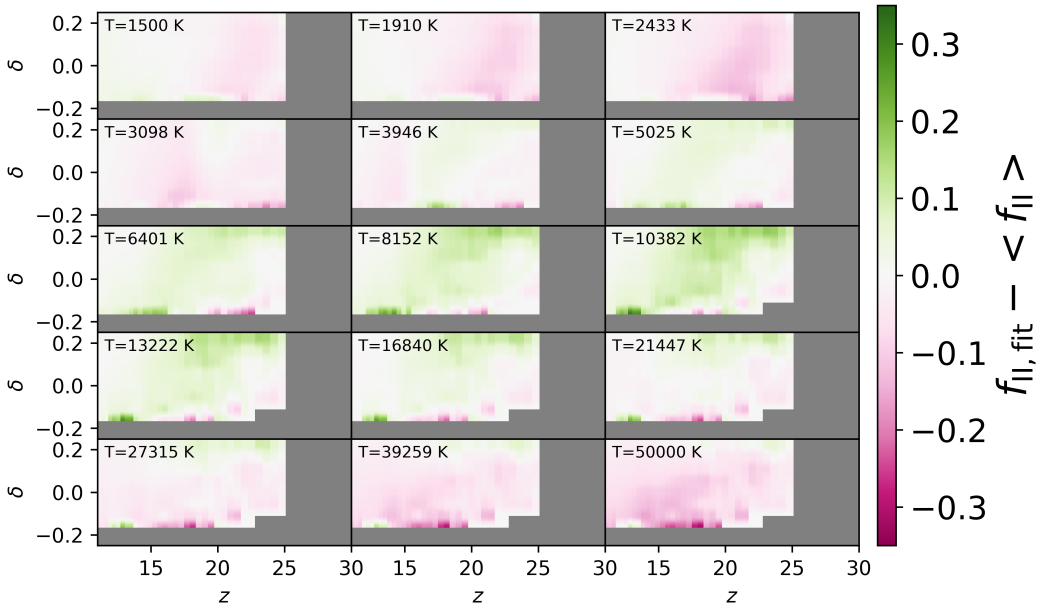

Figure 6.10: Same as Fig. 6.9 but for the intermediate transition.

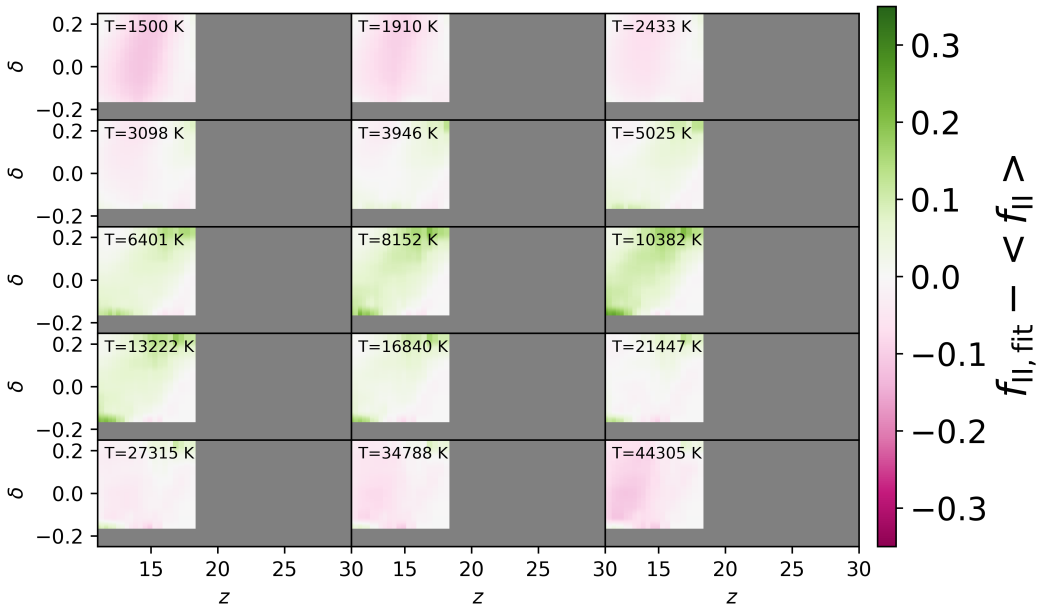

Figure 6.11: Same as Fig. 6.9 but for the slow transition.

7

Conclusion

7.1 Summary

At the beginning of this thesis, I summarized the current state of the research on the earliest generations of stars and the conditions of their formation. Fundamentally, the properties of Pop III stars, especially their IMF, are still very uncertain. Simulations of their formation are still partially contradictory and inconclusive. There are thus far no direct detections of light emitted by Pop III stars, of neither massive stars and their SNe in the high-redshift Universe nor long-lived stars locally. This lack of detections prevents detailed observational studies of the properties of metal-free stars.

Several indirect detection methods can give us some insights. However, these methods are often convoluted, dependent on various assumptions and models and limited in scope. Stellar archaeology is the most accessible of these and relies heavily on modelled SN yields and on assumptions about how these yields mix with the pristine ambient medium. The global 21 cm absorption signal appears to be only sensitive to the overall integrated emission characteristics of Pop III stars. The non-detection of metal-free stars allows to constrain the IMF relatively robustly but only in an extremely narrow range of stellar masses. Detection of compact remnant mergers may carry information about the first stars, but constraints can only be derived when individual events or features in the distribution of their properties can be associated with the first stars. This thesis aims at enhancing our ability to derive properties of the first stars with such indirect methods and emphasizes the importance of the transition to metal-enriched star formation.

In Chapter 3, I develop a new method for analysing the constraints implied by the non-detection of metal-free stars. The method is based on the idea that any observational program finding extremely metal-poor stars is equally suitable to find metal-free ones. The analysis allows us to straightforwardly include surveys and individual detections, without considering the selection functions of these. At the same time, the statistical description results not only in an upper limit of the occurrence rate of metal-free survivors but also in a well-determined confidence level of this result. This analysis leads to the most stringent upper limit on metal-free survivors yet: no more than 1650 metal-free stars in the mass range of $0.6\,\mathrm{M}_\odot \lesssim M \lesssim 0.8\mathrm{M}_\odot$ can be in the Milky Way at 98 per cent confidence. From this, we estimate that there can be only one such survivor in this mass range per $1200\,\mathrm{M}_\odot$ of Pop III stars. Thus, the IMF must be either substantially top-heavy or truncated towards lower masses.

A new look at stellar abundance fitting procedures is presented in Chapter 4. I derived an analytical limit on the mixing behaviour of isolated Pop III SNe and verified it with a comparison against a large set of existing literature on numerical simulations of these SNe. This analytical limit is then integrated into a newly developed Bayesian abundance fitting tool, which simultaneously takes measured abundances and derived upper limits into account. This abundance fitting method is used to reevaluate progenitor scenarios for two individual stars as well as one large selection of EMP stars. Additionally, it is also used for analysing possible progenitor scenarios in Hansen et al. (2020). The findings show that constraining the mixing behaviour of primordial SNe has a decisive impact on how we interpret observed abundance patterns. In particular, faint SNe often fail to explain the observed carbon enhancement, because they produce very small amounts of ejecta. This finding highlights the importance of understanding metal-mixing in the high-redshift Universe and that these processes must be an integral part of any comprehensive framework for stellar archaeology.

In the context of the previously discussed importance of mixing behaviour of high-redshift SNe, Chapter 5 explores the question of PISNe and in particular of the lack of observations of their characteristic abundance patterns. To this end, a large, high-resolution, high-dynamic-range, and multi-physics cosmological simulation is executed. This simulation shows the evolution of extremely energetic SN remnants in unprecedented detail. The results of this simulation indicate that, if extremely energetic PISNe exist, they should commonly result in the formation of EMP stars carrying their nucleosynthetic fingerprint. The simulation also highlights the importance of considering dilution in stellar archaeology and working towards quantification of the dilution and fallback processes. It appears that these processes are governed by the destruction or survival of dense clumps within the host halo. The simulation contains a wealth of data that will be further analysed in follow-up studies.

Chapter 6 explores the impact of the transition from metal-free to metal-enriched star formation on the global 21 cm absorption signal and the 21 cm power spectrum. Since this is an inherently multi-scaled problem, several nested models are used to study this issue. The transition from metal-free to metal-enriched star formation is modelled with the semi-analytical model A-SLOTH and then implemented into a dedicated simulation code for modelling the 21 cm signal (see Reis et al., 2020b). We vary the recovery time in the range of 10–100 Myr and find a significant impact of this variation on the signal and the power spectrum. Once the recovery times,

and in particular, their dependence on the number and energy of the first SNe, are understood better, this finding can be used to infer properties of the first stars from 21 cm signals.

In summary, the work presented within this thesis opens up new and improved ways to constrain the IMF of the first stars through observational means. All these methods rely on the transition from metal-free to metal-enriched star formation, whether it is via the ability or inability to form long-lived stars in Chapter 3 or more directly on the duration of and mixing processes occurring during this transition period in the later chapters. Going forward, gaining a more detailed and quantitative understanding of this epoch will be instrumental for forming a coherent framework that simultaneously explores the hints, relics and observations from the early Universe.

7.2 Outlook

In addition to the direct scientific results presented in this thesis, the developed methods will help to drive the progress in the investigation of early star formation in multiple ways. Several ongoing projects are deploying these methods currently. Chen et al. (2022) use A-SLOTH to investigate the satellites of the Milky Way, and in particular, which conditions could have led to the observed ensemble of satellites. Since such a study requires exploring a multi-dimensional parameter space, especially the numerical methods discussed in Section 6.7.2 are vital for this project. The resulting fitting functions from Chapter 6 have become an integral part of the aforementioned 21 cm simulation code. This addition is currently used to explore the effect of varying the Pop III IMF and star formation efficiency on 21 cm signal and power spectrum (Gessey-Jones et al. in prep.). Additionally, the source code (Magg et al. in prep.) and physical model (Hartwig et al. in prep.) of A-SLOTH are currently being documented and prepared for public release. The applications for this program are numerous and the publication of the code will allow researchers to test hypotheses within a fully developed and understood framework of early star formation, rather than having to develop narrowly scoped models for particular applications.

The simulation methods developed in and for Chapter 5 (also see Jaura et al., 2020), can be applied to the more general study of minihaloes. The simulation code can model Pop III stars based on a user-defined IMF and study the effects of different SN models, star formation efficiencies, stellar multiplicities and more.

Sartorio et al. (in prep.) have extended SPRAI to model X-rays and are using the set-up developed here to model the escape of X-ray photons from minihaloes. This thus far poorly understood process might have a significant impact on the heating of the IGM and therefore on the 21 cm background.

Due to the new instruments, facilities and surveys, the high redshift Universe and the epoch of reionization will become far more accessible in the coming decade. Large multi-object spectroscopic surveys such as the 4-metre Multi-Object Spectroscopic Telescope (4MOST) in the southern and the William Herschel Telescope Enhanced Area Velocity Explorer (WEAVE) in the northern hemisphere are expected to significantly increase the number of low metallicity stars with known chemical abundances. The 4MOST high-resolution Galactic halo survey is projected to provide abundances for around 30000 stars below a metallicity of [Fe/H] $= -2$ (Christlieb et al., 2019). If no metal-free stars are among these, the method developed in Chapter 3 can be used to further constrain the Pop III IMF. Additionally, the high-resolution spectrograph at the Extremely Large Telescope (ELT) will allow one to determine stellar atmospheric abundances with unprecedented precision in the 2030s (Marconi et al., 2021). This wealth of new abundance data will significantly advance the field of stellar archaeology. The studies presented in this thesis demonstrate the importance of accurate chemical mixing models for any interpretative framework attempting to analyse these abundances.

There are many new experiments underway which will be able to investigate the eras of Cosmic Dawn and reionization via 21 cm absorption and emission features (see Section 6.1). The SKA will be the flagship observatory of this era, starting operations in the late 2020s (Koopmans et al., 2015). This project will allow observations of the 21 cm signal and its power spectrum in great detail, offering us unprecedented insights into these eras. Fast quantitative prediction models are required to analyse the obtained data. The obtained power-spectra do not easily translate to the physical parameters governing the high-redshift Universe. Rather, similar to analysis of the CMB power spectrum (see e.g. Planck Collaboration et al., 2016a), the obtained data will be analysed by generating synthetic observations for many different parameter combinations and comparing each of these to the real observations (Fialkov et al., 2018). Thus, fast and accurate models of high-redshift star formation are vital to be able to understand these much-anticipated observations. The advances made in this thesis (Chapter 6) not only help to improve the accuracy of these models but also highlight that 21 cm tomography can constrain early star formation by proxy of the recovery time.

The final significant advancement on the observational frontier is the JWST (Gardner et al., 2006). While JWST is not expected to observe the first stars directly (Schauer et al., 2020), it will still push the observational frontiers deep into the epoch of reionization (Vikaeus et al., 2020). This will give new insights into the first galaxies and constraining their properties will be a great advantage in the study of the first stars. The semi-analytical code A-SLOTH, partially developed in this thesis, can be used to rapidly generate the relevant galaxies under varying assumptions, aiding the interpretation of observational results and constraining the circumstances that gave rise to them. Additionally, the simulation tool presented in Chapter 5 can naturally be extended for simulations of the first galaxies.

Overall, the coming decade will bring unprecedented new insights from the early Universe. The results shown and the methods developed in this thesis can aid the interpretation of the new data and will be essential to enhance our ability to make the most out of what these new instruments will find.

Acknowledgements

My eternal gratitude for far more than words can express goes to my wonderful wife. For many years of scientific and personal advice and guidance, I would like to thank my supervisors Ralf Klessen and Simon Glover. I would like to thank Anna Schauer for being a truly excellent advisor and role model. For discussions, distractions, advice and many coffee breaks I would like to thank the past and present ITA team, in particular: Mattia Sormani, Bhaskar Agarwal, Eric Pellegrini, Robin Treß, Ondrej Jaura and Loke Lönnbald Ohlin. Special thanks for making the Arepo code available go to Volker Springel. For helping with the strangest bugs, I would like to thank Rüdiger Pakmor and the Intel Support forum. Without the support and company of my study-buddies and friends. I would never have made it thus far. Therefore, I would like to thank Eva Weber, Caroline Gieser, Falk Bartels, Maximilian Disch, and most of all Katja Fahrion. Thank you for proofreading and may you never go hollow!

For data analysis, we used the Python packages Astropy (Astropy Collaboration et al., 2013), F2PY (Peterson, 2009), h5py (Collette, 2013), NumPy (Oliphant, 2006), matplotlib (Hunter, 2007) and SciPy (Jones et al., 2001). Rockstar (Behroozi et al., 2013a), HMFcalc (Murray et al., 2013) and Ned Wright's Cosmology Calculator (Wright, 2006) were used during the preparation of this thesis. The simulation in Chapter 5 was carried out on Supermuc-NG and I gratefully acknowledge the Gauss Centre for Supercomputing e.V. (`www.gauss-centre.eu`) for funding this project by providing computing time on the GCS Supercomputer SuperMUC-NG at Leibniz Supercomputing Centre (`www.lrz.de`) under computing grant number pr74nu. I also gratefully acknowledge the data storage service SDShd and the computing service bwHPC, supported by the Ministry of Science, Research and the Arts Baden-Württemberg (MWK) and the German Research Foundation (DFG) through grant INST 35/1314-1 FUGG. Additional computations were carried out at the computing cluster at the institute for scientific computing in Heidelberg.

References

Abbott, B. P., Abbott, R., Abbott, T. D., et al. 2016, Phys. Rev. Lett., 116, 061102

—. 2017, ApJ, 848, L12

Abbott, R., Abbott, T. D., Abraham, S., et al. 2020, ApJ, 900, L13

Abel, T., Bryan, G. L., & Norman, M. L. 2000, ApJ, 540, 39

—. 2002, Science, 295, 93

Abel, T., Wise, J. H., & Bryan, G. L. 2007, ApJ, 659, L87

Agarwal, B., & Khochfar, S. 2015, MNRAS, 446, 160

Agarwal, B., Smith, B., Glover, S., Natarajan, P., & Khochfar, S. 2016, MNRAS, 459, 4209

Alpher, R. A., Bethe, H., & Gamow, G. 1948, Phys. Rev., 73, 803

Aoki, W., Tominaga, N., Beers, T. C., Honda, S., & Lee, Y. S. 2014, Science, 345, 912

Arentsen, A., Starkenburg, E., Shetrone, M. D., et al. 2019, A&A, 621, A108

Arentsen, A., Starkenburg, E., Martin, N. F., et al. 2020, MNRAS, 491, L11

Asplund, M., Grevesse, N., Sauval, A. J., & Scott, P. 2009, ARA&A, 47, 481

Astropy Collaboration, Robitaille, T. P., Tollerud, E. J., et al. 2013, A&A, 558, A33

Baczynski, C., Glover, S. C. O., & Klessen, R. S. 2015, MNRAS, 454, 380

Bailer-Jones, C. A. L. 2017, Practical Bayesian Inference: A Primer for Physical Scientists (Cambridge University Press), doi:10.1017/9781108123891

Barkana, R. 2018a, Nature, 555, 71

—. 2018b, The Encyclopedia of Cosmology. Volume 1: Galaxy Formation and Evolution Rennan Barkana Tel Aviv University, doi:10.1142/9496-vol1

Barkana, R., & Loeb, A. 2004, ApJ, 609, 474

—. 2005, The Astrophysical Journal, 626, 1

Bate, M. R., Bonnell, I. A., & Price, N. M. 1995, MNRAS, 277, 362

Behroozi, P., Wechsler, R. H., Hearin, A. P., & Conroy, C. 2019, MNRAS, 488, 3143

Behroozi, P. S., Wechsler, R. H., & Wu, H.-Y. 2013a, ApJ, 762, 109

Behroozi, P. S., Wechsler, R. H., Wu, H.-Y., et al. 2013b, ApJ, 763, 18

Bell, E. F., Zucker, D. B., Belokurov, V., et al. 2008, ApJ, 680, 295

Bessell, M. S., Collet, R., Keller, S. C., et al. 2015, ApJ, 806, L16

Bollig, R., Yadav, N., Kresse, D., et al. 2021, ApJ, 915, 28

Bond, J. R., Cole, S., Efstathiou, G., & Kaiser, N. 1991, ApJ, 379, 440

Bonifacio, P., Monaco, L., Salvadori, S., et al. 2021, A&A, 651, A79

Bowler, R. A. A., McLure, R. J., Dunlop, J. S., et al. 2017, MNRAS, 469, 448

Bowman, J. D., Rogers, A. E. E., Monsalve, R. A., Mozdzen, T. J., & Mahesh, N. 2018, Nature, 555, 67

Bowman, J. D., Cairns, I., Kaplan, D. L., et al. 2013, PASA, 30, e031

Boylan-Kolchin, M., Springel, V., White, S. D. M., Jenkins, A., & Lemson, G. 2009, MNRAS, 398, 1150

Branch, D., & Wheeler, J. C. 2017, Supernova Explosions, doi:10.1007/978-3-662-55054-0

Brauer, K., Ji, A. P., Frebel, A., et al. 2019, ApJ, 871, 247

Bremer, J., Dayal, P., & Ryan-Weber, E. V. 2018, MNRAS, 477, 2154

Bromm, V. 2013, Reports on Progress in Physics, 76, 112901

Bromm, V., Coppi, P. S., & Larson, R. B. 1999, ApJ, 527, L5

—. 2002, ApJ, 564, 23

Bromm, V., Ferrara, A., Coppi, P. S., & Larson, R. B. 2001, MNRAS, 328, 969

Bullock, J. S., & Boylan-Kolchin, M. 2017, ARA&A, 55, 343

Bullock, J. S., Stewart, K. R., & Purcell, C. W. 2009, 254, 85

Caffau, E., Bonifacio, P., François, P., et al. 2011, Nature, 477, 67

Caffau, E., Bonifacio, P., François, P., et al. 2012, A&A, 542, A51

Chabrier, G. 2003, PASP, 115, 763

Chan, C., Mueller, B., & Heger, A. 2020, MNRAS, 495, 3751

Chan, C., Müller, B., Heger, A., Pakmor, R., & Springel, V. 2018, ApJ, 852, L19

Chandrasekhar, S. 1931, ApJ, 74, 81

Chatzopoulos, E., & Wheeler, J. C. 2012, ApJ, 748, 42

Chen, K.-J., Bromm, V., Heger, A., Jeon, M., & Woosley, S. 2015, ApJ, 802, 13

Chen, K.-J., Heger, A., Whalen, D. J., et al. 2017a, MNRAS, 467, 4731

Chen, K.-J., Whalen, D. J., Wollenberg, K. M. J., Glover, S. C. O., & Klessen, R. S. 2017b, ApJ, 844, 111

Chen, L.-H., Magg, M., Hartwig, T., et al. 2022, arXiv e-prints, arXiv:2202.01220

Chen, X., & Miralda-Escudé, J. 2004, ApJ, 602, 1

Chiaki, G., Marassi, S., Nozawa, T., et al. 2015, MNRAS, 446, 2659

Chiaki, G., Susa, H., & Hirano, S. 2018, MNRAS, 475, 4378

Chiaki, G., Tominaga, N., & Nozawa, T. 2017, MNRAS, 472, L115

Chiaki, G., & Wise, J. H. 2019, MNRAS, 482, 3933

Chiaki, G., Wise, J. H., Marassi, S., et al. 2020, MNRAS, arXiv:2007.06657

Chiaki, G., Yoshida, N., & Hirano, S. 2016, MNRAS, 463, 2781

Chiti, A., Frebel, A., Simon, J. D., et al. 2021, Nature Astronomy, 5, 392

Choplin, A., & Hirschi, R. 2020, in Journal of Physics Conference Series, Vol. 1668, Journal of Physics Conference Series, 012006

Choplin, A., Hirschi, R., Meynet, G., & Ekström, S. 2017, A&A, 607, L3

Christlieb, N., Schörck, T., Frebel, A., et al. 2008, A&A, 484, 721

Christlieb, N., Battistini, C., Bonifacio, P., et al. 2019, The Messenger, 175, 26

Chuzhoy, L., & Shapiro, P. R. 2007, ApJ, 655, 843

Clark, P. C., Glover, S. C. O., & Klessen, R. S. 2008, ApJ, 672, 757

Clark, P. C., Glover, S. C. O., Klessen, R. S., & Bromm, V. 2011a, ApJ, 727, 110

Clark, P. C., Glover, S. C. O., Smith, R. J., et al. 2011b, Science, 331, 1040

Cohen, A., Fialkov, A., & Barkana, R. 2016, MNRAS, 459, L90

—. 2018, MNRAS, 478, 2193

Cohen, A., Fialkov, A., Barkana, R., & Lotem, M. 2017, MNRAS, 472, 1915

Cohen, A., Fialkov, A., Barkana, R., & Monsalve, R. A. 2020, MNRAS, 495, 4845

Collette, A. 2013, Python and HDF5 (O'Reilly)

Côté, B., Silvia, D. W., O'Shea, B. W., Smith, B., & Wise, J. H. 2018, ApJ, 859, 67

Courant, R., Friedrichs, K., & Lewy, H. 1928, Mathematische Annalen, 100, 32

Dayal, P., & Ferrara, A. 2018, Phys. Rep., 780, 1

de Bennassuti, M., Salvadori, S., Schneider, R., Valiante, R., & Omukai, K. 2017, MNRAS, 465, 926

DeBoer, D. R., Parsons, A. R., Aguirre, J. E., et al. 2017, PASP, 129, 045001

Dijkstra, M., Haiman, Z., Mesinger, A., & Wyithe, J. S. B. 2008, MNRAS, 391, 1961

Dopcke, G., Glover, S. C. O., Clark, P. C., & Klessen, R. S. 2011, ApJ, 729, L3

Dopcke, G., Glover, S. C. O., Clark, P. C., & Klessen, R. S. 2013, ApJ, 766, 103

Dorodnitsyn, V. 2001, Applied Numerical Mathematics, 39, 307, themes in Geometric Integration

Draine, B. T. 2011, Physics of the Interstellar and Intergalactic Medium (Princeton Univ. Press)

Druschke, M., Schauer, A. T. P., Glover, S. C. O., & Klessen, R. S. 2020, MNRAS, 498, 4839

Dullemond, C. P., Juhasz, A., Pohl, A., et al. 2012, RADMC-3D: A multi-purpose radiative transfer tool, ascl:1202.015

Eastwood, M. W., Anderson, M. M., Monroe, R. M., et al. 2019, AJ, 158, 84

Eggenberger, P., Ekström, S., Georgy, C., et al. 2021, A&A, 652, A137

Eisenstein, D. J., Zehavi, I., Hogg, D. W., et al. 2005, ApJ, 633, 560

Ezzeddine, R., Frebel, A., Roederer, I. U., et al. 2019, ApJ, 876, 97

Federrath, C., Banerjee, R., Clark, P. C., & Klessen, R. S. 2010, ApJ, 713, 269

Federrath, C., & Klessen, R. S. 2012, ApJ, 761, 156

Federrath, C., Klessen, R. S., Iapichino, L., & Beattie, J. R. 2021, Nature Astronomy, 5, 365

Feng, C., & Holder, G. 2018, ApJ, 858, L17

Fialkov, A., & Barkana, R. 2014, MNRAS, 445, 213

—. 2019, MNRAS, 486, 1763

Fialkov, A., Barkana, R., & Cohen, A. 2018, ArXiv e-prints, arXiv:1802.10577

Fialkov, A., Barkana, R., Tseliakhovich, D., & Hirata, C. M. 2012, MNRAS, 424, 1335

Fialkov, A., Barkana, R., & Visbal, E. 2014, Nature, 506, 197

Fialkov, A., Barkana, R., Visbal, E., Tseliakhovich, D., & Hirata, C. M. 2013, MNRAS, 432, 2909

Field, G. B. 1958, Proceedings of the IRE, 46, 240

Fields, B. D., Olive, K. A., Yeh, T.-H., & Young, C. 2020, J. Cosmology Astropart. Phys., 2020, 010

Fragos, T., Lehmer, B., Tremmel, M., et al. 2013, ApJ, 764, 41

François, P., Caffau, E., Bonifacio, P., et al. 2018, A&A, 620, A187

Fraser, M., Casey, A. R., Gilmore, G., Heger, A., & Chan, C. 2017, MNRAS, 468, 418

Frebel, A., Ji, A. P., Ezzeddine, R., et al. 2019, ApJ, 871, 146

Frebel, A., Johnson, J. L., & Bromm, V. 2009, MNRAS, 392, L50

Frebel, A., & Norris, J. E. 2015, ARA&A, 53, 631

Fryxell, B., Olson, K., Ricker, P., et al. 2000, ApJS, 131, 273

Gardner, J. P., Mather, J. C., Clampin, M., et al. 2006, Space Sci. Rev., 123, 485

Garrison-Kimmel, S., Boylan-Kolchin, M., Bullock, J. S., & Lee, K. 2014, MNRAS, 438, 2578

Garrison-Kimmel, S., Bullock, J. S., Boylan-Kolchin, M., & Bardwell, E. 2017, MNRAS, 464, 3108

Garsden, H., Greenhill, L., Bernardi, G., et al. 2021, MNRAS, arXiv:2102.09596

Gatto, A., Walch, S., Mac Low, M.-M., et al. 2015, MNRAS, 449, 1057

Geen, S., Watson, S. K., Rosdahl, J., et al. 2018, MNRAS, 481, 2548

Gehlot, B. K., Mertens, F. G., Koopmans, L. V. E., et al. 2019, MNRAS, 488, 4271

Genel, S., Vogelsberger, M., Nelson, D., et al. 2013, MNRAS, 435, 1426

Gilmer, M. S., Kozyreva, A., Hirschi, R., Fröhlich, C., & Yusof, N. 2017, ApJ, 846, 100

Girichidis, P., Offner, S. S. R., Kritsuk, A. G., et al. 2020, Space Sci. Rev., 216, 68

Glover, S. 2013, in Astrophysics and Space Science Library, Vol. 396, Astrophysics and Space Science Library, ed. T. Wiklind, B. Mobasher, & V. Bromm, 103

Glover, S. C. O. 2015, MNRAS, 451, 2082

Glover, S. C. O., & Abel, T. 2008, MNRAS, 388, 1627

Glover, S. C. O., & Savin, D. W. 2009, MNRAS, 393, 911

Graziani, L., de Bennassuti, M., Schneider, R., Kawata, D., & Salvadori, S. 2017, MNRAS, 469, 1101

Greif, T. H. 2015, Computational Astrophysics and Cosmology, 2, 3

Greif, T. H., Bromm, V., Clark, P. C., et al. 2012, MNRAS, 424, 399

Greif, T. H., Glover, S. C. O., Bromm, V., & Klessen, R. S. 2010, ApJ, 716, 510

Greif, T. H., Johnson, J. L., Bromm, V., & Klessen, R. S. 2007, ApJ, 670, 1

Greif, T. H., Springel, V., White, S. D. M., et al. 2011a, ApJ, 737, 75

Greif, T. H., White, S. D. M., Klessen, R. S., & Springel, V. 2011b, ApJ, 736, 147

Griffen, B. F., Ji, A. P., Dooley, G. A., et al. 2016, ApJ, 818, 10

Grimmett, J. J., Heger, A., Karakas, A. I., & Müller, B. 2018, MNRAS, 479, 495

Gronow, S., Collins, C. E., Sim, S. A., & Röpke, F. K. 2021, A&A, 649, A155

Gunn, J. E., & Peterson, B. A. 1965, ApJ, 142, 1633

Hahn, O., & Abel, T. 2011, MNRAS, 415, 2101

Haiman, Z., Abel, T., & Rees, M. J. 2000, ApJ, 534, 11

Hansen, C. J., Hansen, T. T., Koch, A., et al. 2019, A&A, 623, A128

Hansen, C. J., Koch, A., Mashonkina, L., et al. 2020, A&A, 643, A49

Hartwig, T., Bromm, V., Klessen, R. S., & Glover, S. C. O. 2015, MNRAS, 447, 3892

Hartwig, T., Bromm, V., & Loeb, A. 2018a, MNRAS, 479, 2202

Hartwig, T., Volonteri, M., Bromm, V., et al. 2016a, MNRAS, 460, L74

Hartwig, T., Latif, M. A., Magg, M., et al. 2016b, MNRAS, 462, 2184

Hartwig, T., Yoshida, N., Magg, M., et al. 2018b, MNRAS, arXiv:1801.05044

Heger, A., Fryer, C. L., Woosley, S. E., Langer, N., & Hartmann, D. H. 2003, ApJ, 591, 288

Heger, A., & Woosley, S. E. 2002, ApJ, 567, 532

—. 2010, ApJ, 724, 341

Heinrich, C., & Hu, W. 2018, Phys. Rev. D, 98, 063514

Hennebelle, P., & Chabrier, G. 2011, ApJ, 743, L29

Hills, R., Kulkarni, G., Meerburg, P. D., & Puchwein, E. 2018, Nature, 564, E32

Hirano, S., & Bromm, V. 2017, MNRAS, 470, 898

Hirano, S., Hosokawa, T., Yoshida, N., et al. 2014, ApJ, 781, 60

Hirano, S., Yoshida, N., Sakurai, Y., & Fujii, M. S. 2018, ApJ, 855, 17

Hirata, C. M. 2006, MNRAS, 367, 259

Hopkins, P. F. 2015, MNRAS, 450, 53

Hosokawa, T., Hirano, S., Kuiper, R., et al. 2016, ApJ, 824, 119

Hosokawa, T., Omukai, K., Yoshida, N., & Yorke, H. W. 2011, Science, 334, 1250

Hummel, J. A., Pawlik, A. H., Milosavljević, M., & Bromm, V. 2012, ApJ, 755, 72

Hunter, J. 2007, Computing in Science & Engineering, 9, 90

Ishigaki, M. N., Tominaga, N., Kobayashi, C., & Nomoto, K. 2014, ApJ, 792, L32

—. 2018, ApJ, 857, 46

Ishiyama, T., Sudo, K., Yokoi, S., et al. 2016, ApJ, 826, 9

Ishiyama, T., Prada, F., Klypin, A. A., et al. 2021, MNRAS, 506, 4210

Jaacks, J., Finkelstein, S. L., & Bromm, V. 2019, MNRAS, 488, 2202

Jaacks, J., Thompson, R., Finkelstein, S. L., & Bromm, V. 2018, MNRAS, 475, 4396

Jablonka, P., North, P., Mashonkina, L., et al. 2015, A&A, 583, A67

Janka, H.-T., Melson, T., & Summa, A. 2016, Annual Review of Nuclear and Particle Science, 66, 341

Jappsen, A.-K., Glover, S. C. O., Klessen, R. S., & Mac Low, M.-M. 2007, ApJ, 660, 1332

Jaura, O., Glover, S. C. O., Klessen, R. S., & Paardekooper, J.-P. 2018, MNRAS, 475, 2822

Jaura, O., Magg, M., Glover, S. C. O., & Klessen, R. S. 2020, MNRAS, 499, 3594

Jeans, J. H. 1902, Philosophical Transactions of the Royal Society of London Series A, 199, 1

Jeon, M., & Bromm, V. 2019, MNRAS, 485, 5939

Jeon, M., Pawlik, A. H., Bromm, V., & Milosavljević, M. 2014, MNRAS, 444, 3288

Ji, A. P., Frebel, A., Chiti, A., & Simon, J. D. 2016a, Nature, 531, 610

Ji, A. P., Frebel, A., Simon, J. D., & Chiti, A. 2016b, ApJ, 830, 93

Ji, A. P., Li, T. S., Simon, J. D., et al. 2020, ApJ, 889, 27

Johnson, J. L. 2015, MNRAS, 453, 2771

Johnson, J. L., Dalla, V. C., & Khochfar, S. 2013, MNRAS, 428, 1857

Johnson, J. L., & Khochfar, S. 2011, MNRAS, 413, 1184

Jones, E., Oliphant, T., Peterson, P., et al. 2001, SciPy: Open source scientific tools for Python

Kannan, R., Vogelsberger, M., Marinacci, F., et al. 2019, MNRAS, 485, 117

Karlsson, T., Johnson, J. L., & Bromm, V. 2008, ApJ, 679, 6

Keller, S. C., Bessell, M. S., Frebel, A., et al. 2014, Nature, 506, 463

Kippenhahn, R., Weigert, A., & Weiss, A. 2012, Stellar structure and evolution, second edition edn., Astronomy and astrophysics library (Springer), xviii, 604 Seiten, doi:10.1007/978-3-642-30304-3

Kitayama, T., Yoshida, N., Susa, H., & Umemura, M. 2004, ApJ, 613, 631

Klypin, A. A., Trujillo-Gomez, S., & Primack, J. 2011, ApJ, 740, 102

Knollmann, S. R., & Knebe, A. 2009, ApJS, 182, 608

Kobayashi, C., Tominaga, N., & Nomoto, K. 2011, ApJ, 730, L14

Komiya, Y., Suda, T., & Fujimoto, M. Y. 2015, ApJ, 808, L47

—. 2016, ApJ, 820, 59

Komiya, Y., Suda, T., Yamada, S., & Fujimoto, M. Y. 2020, ApJ, 890, 66

Koopmans, L., Pritchard, J., Mellema, G., et al. 2015, in Advancing Astrophysics with the Square Kilometre Array (AASKA14), 1

Kroupa, P. 2001, MNRAS, 322, 231

Kruip, C. J. H., Paardekooper, J.-P., Clauwens, B. J. F., & Icke, V. 2010, A&A, 515, A78

Krumholz, M. R. 2011, in American Institute of Physics Conference Series, Vol. 1386, American Institute of Physics Conference Series, ed. E. Telles, R. Dupke, & D. Lazzaro, 9–57

Krumholz, M. R., Klein, R. I., McKee, C. F., & Bolstad, J. 2007, ApJ, 667, 626

Krumholz, M. R., & McKee, C. F. 2005, ApJ, 630, 250

Kulkarni, M., Visbal, E., & Bryan, G. L. 2021, ApJ, 917, 40

Lacey, C., & Cole, S. 1993, MNRAS, 262, 627

Larson, R. B. 1998, MNRAS, 301, 569

Latif, M. A., & Schleicher, D. 2020, ApJ, 902, L31

Latif, M. A., Whalen, D., & Khochfar, S. 2021, arXiv e-prints, arXiv:2109.10655

Lau, H. H. B., Stancliffe, R. J., & Tout, C. A. 2007, MNRAS, 378, 563

Lewis, A., Challinor, A., & Lasenby, A. 2000, ApJ, 538, 473

Li, H., Tan, K., & Zhao, G. 2018, ApJS, 238, 16

Limongi, M., & Chieffi, A. 2012, ApJS, 199, 38

Lucatello, S., Tsangarides, S., Beers, T. C., et al. 2005, ApJ, 625, 825

Machacek, M. E., Bryan, G. L., & Abel, T. 2001, ApJ, 548, 509

Madau, P., Meiksin, A., & Rees, M. J. 1997, ApJ, 475, 429

Maeder, A., & Meynet, G. 2000, ARA&A, 38, 143

Magg, M., Hartwig, T., Agarwal, B., et al. 2018, MNRAS, 473, 5308

Magg, M., Hartwig, T., Glover, S. C. O., Klessen, R. S., & Whalen, D. J. 2016, MNRAS, 462, 3591

Magg, M., Klessen, R. S., Glover, S. C. O., & Li, H. 2019, MNRAS, 487, 486

Magg, M., Schauer, A. T. P., Klessen, R. S., et al. 2021a, arXiv e-prints, arXiv:2110.15372

Magg, M., Nordlander, T., Glover, S. C. O., et al. 2020, MNRAS, 498, 3703

Magg, M., Reis, I., Fialkov, A., et al. 2021b, arXiv e-prints, arXiv:2110.15948

Marconi, A., Abreu, M., Adibekyan, V., et al. 2021, The Messenger, 182, 27

Marigo, P., Chiosi, C., & Kudritzki, R. P. 2003, A&A, 399, 617

Marigo, P., Girardi, L., Chiosi, C., & Wood, P. R. 2001, A&A, 371, 152

McConnachie, A. W. 2012, AJ, 144, 4

McKee, C. F., & Ostriker, E. C. 2007, ARA&A, 45, 565

McWilliam, A., Preston, G. W., Sneden, C., & Searle, L. 1995, AJ, 109, 2757

Mebane, R. H., Mirocha, J., & Furlanetto, S. R. 2018, MNRAS, 479, 4544

—. 2020, MNRAS, 493, 1217

Mesinger, A. 2019, The Cosmic 21-cm Revolution; Charting the first billion years of our universe, doi:10.1088/2514-3433/ab4a73

Meynet, G., & Maeder, A. 2017, Supernovae from Rotating Stars, ed. A. W. Alsabti & P. Murdin, 601

Mirocha, J., & Furlanetto, S. R. 2019, MNRAS, 483, 1980

Mirocha, J., Mebane, R. H., Furlanetto, S. R., Singal, K., & Trinh, D. 2018, MNRAS, 478, 5591

Mocz, P., Vogelsberger, M., Pakmor, R., et al. 2015, MNRAS, 452, 3853

Mocz, P., Vogelsberger, M., Robles, V. H., et al. 2017, MNRAS, 471, 4559

Mondal, R., Fialkov, A., Fling, C., et al. 2020, MNRAS, 498, 4178

Monsalve, R. A., Fialkov, A., Bowman, J. D., et al. 2019, ApJ, 875, 67

Murphy, L. J., Groh, J. H., Ekström, S., et al. 2021, MNRAS, 501, 2745

Murray, S. G., Power, C., & Robotham, A. S. G. 2013, Astronomy and Computing, 3, 23

Naoz, S., Noter, S., & Barkana, R. 2006, MNRAS, 373, L98

Naoz, S., Yoshida, N., & Gnedin, N. Y. 2013, ApJ, 763, 27

Nishimura, N., Takiwaki, T., & Thielemann, F.-K. 2015, ApJ, 810, 109

Noether, E. 1918, Nachrichten von der Gesellschaft der Wissenschaften zu Göttingen, Mathematisch-Physikalische Klasse, 1918, 235

Nomoto, K., Kobayashi, C., & Tominaga, N. 2013, ARA&A, 51, 457

Nordlander, T., Amarsi, A. M., Lind, K., et al. 2017, A&A, 597, A6

Nordlander, T., Bessell, M. S., Da Costa, G. S., et al. 2019, MNRAS, 488, L109

Oey, M. S. 2003, MNRAS, 339, 849

Oliphant, T. 2006, A guide to NumPy

O'Shea, B. W., & Norman, M. L. 2008, ApJ, 673, 14

Ostriker, J. P., & McKee, C. F. 1988, Reviews of Modern Physics, 60, 1

Paardekooper, J.-P., Kruip, C. J. H., & Icke, V. 2010, A&A, 515, A79

Padoan, P., & Nordlund, Å. 2011, ApJ, 730, 40

Pakmor, R., Springel, V., Bauer, A., et al. 2016, MNRAS, 455, 1134

Park, H., Shapiro, P. R., Ahn, K., Yoshida, N., & Hirano, S. 2021, ApJ, 908, 96

Park, J., Gillet, N., Mesinger, A., & Greig, B. 2020, MNRAS, 491, 3891

Peebles, P. J. E., & Yu, J. T. 1970, ApJ, 162, 815

Peterson, P. 2009, International Journal of Computational Science and Engineering, 4, 296

Philip, L., Abdurashidova, Z., Chiang, H. C., et al. 2019, Journal of Astronomical Instrumentation, 8, 1950004

Pillepich, A., Nelson, D., Springel, V., et al. 2019, MNRAS, 490, 3196

Planck Collaboration, Ade, P. A. R., Aghanim, N., et al. 2014, A&A, 571, A16

—. 2016a, A&A, 594, A13

Planck Collaboration, Adam, R., Aghanim, N., et al. 2016b, ArXiv e-prints, arXiv:1605.03507

Press, W. H., & Schechter, P. 1974, ApJ, 187, 425

Price, D. C., Greenhill, L. J., Fialkov, A., et al. 2018, MNRAS, 478, 4193

Pritchard, J. R., & Loeb, A. 2012, Reports on Progress in Physics, 75, 086901

Rahner, D., Pellegrini, E. W., Glover, S. C. O., & Klessen, R. S. 2017, MNRAS, 470, 4453

Rakavy, G., & Shaviv, G. 1967, ApJ, 148, 803

Reis, I., Barkana, R., & Fialkov, A. 2020a, arXiv e-prints, arXiv:2008.04914

Reis, I., Fialkov, A., & Barkana, R. 2020b, MNRAS, arXiv:2008.04315

—. 2021, MNRAS, 506, 5479

Reissl, S., Wolf, S., & Brauer, R. 2016, A&A, 593, A87

Revaz, Y., & Jablonka, P. 2012, A&A, 538, A82

Riaz, R., Bovino, S., Vanaverbeke, S., & Schleicher, D. R. G. 2018, MNRAS, 479, 667

Ritter, J. S., Safranek-Shrader, C., Gnat, O., Milosavljević, M., & Bromm, V. 2012, ApJ, 761, 56

Ritter, J. S., Safranek-Shrader, C., Milosavljević, M., & Bromm, V. 2016, MNRAS, 463, 3354

Ritter, J. S., Sluder, A., Safranek-Shrader, C., Milosavljević, M., & Bromm, V. 2015, MNRAS, 451, 1190

Robitaille, T. P., & Whitney, B. A. 2010, ApJ, 710, L11

Rydberg, C.-E., Whalen, D. J., Maturi, M., et al. 2020, MNRAS, 491, 2447

Salpeter, E. E. 1955, ApJ, 121, 161

Salvadori, S., Bonifacio, P., Caffau, E., et al. 2019, MNRAS, 487, 4261

Salvadori, S., Schneider, R., & Ferrara, A. 2007, MNRAS, 381, 647

Sanders, D. B., Scoville, N. Z., & Solomon, P. M. 1985, ApJ, 289, 373

Scalo, J. 1998, in Astronomical Society of the Pacific Conference Series, Vol. 142, The Stellar Initial Mass Function (38th Herstmonceux Conference), ed. G. Gilmore & D. Howell, 201

Schaerer, D. 2002, A&A, 382, 28

Schauer, A. T. P., Drory, N., & Bromm, V. 2020, ApJ, 904, 145

Schauer, A. T. P., Glover, S. C. O., Klessen, R. S., & Ceverino, D. 2019a, MNRAS, 484, 3510

Schauer, A. T. P., Glover, S. C. O., Klessen, R. S., & Clark, P. 2021, MNRAS, 507, 1775

Schauer, A. T. P., Liu, B., & Bromm, V. 2019b, ApJ, 877, L5

Schauer, A. T. P., Regan, J., Glover, S. C. O., & Klessen, R. S. 2017a, MNRAS, 471, 4878

Schauer, A. T. P., Whalen, D. J., Glover, S. C. O., & Klessen, R. S. 2015, MNRAS, 454, 2441

Schauer, A. T. P., Agarwal, B., Glover, S. C. O., et al. 2017b, MNRAS, 467, 2288

Schneider, R., Omukai, K., Bianchi, S., & Valiante, R. 2012, MNRAS, 419, 1566

Schober, J., Schleicher, D., Federrath, C., et al. 2012, ApJ, 754, 99

Sedov, L. I. 1959, Similarity and Dimensional Methods in Mechanics

Sestito, F., Longeard, N., Martin, N. F., et al. 2019, MNRAS, arXiv:1811.03099

Sharda, P., Federrath, C., Krumholz, M. R., & Schleicher, D. R. G. 2021, MNRAS, 503, 2014

Shen, S., Kulkarni, G., Madau, P., & Mayer, L. 2017, MNRAS, 469, 4012

Sheth, R. K., Mo, H. J., & Tormen, G. 2001, MNRAS, 323, 1

Sheth, R. K., & Tormen, G. 1999, MNRAS, 308, 119

Siegel, D. M., Barnes, J., & Metzger, B. D. 2019, Nature, 569, 241

Sims, P. H., & Pober, J. C. 2020, MNRAS, 492, 22

Singh, S., Subrahmanyan, R., Udaya Shankar, N., et al. 2018, ApJ, 858, 54

Skúladóttir, Á., Hansen, C. J., Salvadori, S., & Choplin, A. 2019, A&A, 631, A171

Smith, B., & Lang, M. 2018, ytree: merger-tree toolkit, doi:10.5281/zenodo.1174374

Smith, B. D., Wise, J. H., O'Shea, B. W., Norman, M. L., & Khochfar, S. 2015, MNRAS, 452, 2822

Sobral, D., Matthee, J., Darvish, B., et al. 2015, ApJ, 808, 139

Sormani, M. C., Treß, R. G., Klessen, R. S., & Glover, S. C. O. 2017, MNRAS, 466, 407

Spergel, D. N., Verde, L., Peiris, H. V., et al. 2003, ApJS, 148, 175

Springel, V. 2005, MNRAS, 364, 1105

—. 2010, MNRAS, 401, 791

Springel, V., Di Matteo, T., & Hernquist, L. 2005a, MNRAS, 361, 776

Springel, V., & Hernquist, L. 2002, MNRAS, 333, 649

Springel, V., White, S. D. M., Tormen, G., & Kauffmann, G. 2001, MNRAS, 328, 726

Springel, V., White, S. D. M., Jenkins, A., et al. 2005b, Nature, 435, 629

Springel, V., Wang, J., Vogelsberger, M., et al. 2008, MNRAS, 391, 1685

Springel, V., Pakmor, R., Pillepich, A., et al. 2018, MNRAS, 475, 676

Stacy, A., & Bromm, V. 2014, ApJ, 785, 73

Stacy, A., Bromm, V., & Lee, A. T. 2016, MNRAS, 462, 1307

Stacy, A., Bromm, V., & Loeb, A. 2011, ApJ, 730, L1

Stacy, A., Greif, T. H., & Bromm, V. 2010, MNRAS, 403, 45

—. 2012, MNRAS, 422, 290

Starkenburg, E., Oman, K. A., Navarro, J. F., et al. 2017a, MNRAS, 465, 2212

Starkenburg, E., Martin, N., Youakim, K., et al. 2017b, MNRAS, 471, 2587

Stewart, K. R., Bullock, J. S., Wechsler, R. H., Maller, A. H., & Zentner, A. R. 2008, ApJ, 683, 597

Strömgren, B. 1939, ApJ, 89, 526

Stutzki, J., Bensch, F., Heithausen, A., Ossenkopf, V., & Zielinsky, M. 1998, A&A, 336, 697

Suda, T., Aikawa, M., Machida, M. N., Fujimoto, M. Y., & Iben, Icko, J. 2004, ApJ, 611, 476

Suda, T., Katsuta, Y., Yamada, S., et al. 2008, PASJ, 60, 1159

Sunyaev, R. A., & Zeldovich, Y. B. 1970, Ap&SS, 7, 3

Susa, H. 2019, ApJ, 877, 99

Susa, H., Hasegawa, K., & Tominaga, N. 2014, ApJ, 792, 32

Suzuki, T. K. 2018, PASJ, 70, 34

Takahashi, K., Umeda, H., & Yoshida, T. 2014, ApJ, 794, 40

Takahashi, K., Yoshida, T., & Umeda, H. 2018, ApJ, 857, 111

Tanaka, S. J., Chiaki, G., Tominaga, N., & Susa, H. 2017, ApJ, 844, 137

Tanaka, T., & Hasegawa, K. 2021, MNRAS, 502, 463

Tanaka, T., Hasegawa, K., Yajima, H., Kobayashi, M. I. N., & Sugiyama, N. 2018, MNRAS, 480, 1925

Tanikawa, A., Suzuki, T. K., & Doi, Y. 2018, PASJ, 70, 80

Tarumi, Y., Hartwig, T., & Magg, M. 2020a, ApJ, 897, 58

Tarumi, Y., Yoshida, N., & Inoue, S. 2020b, MNRAS, 494, 120

Taylor, G. 1950, Proceedings of the Royal Society of London. Series A, Mathematical and Physical Sciences, 201, 159

Tegmark, M., Silk, J., Rees, M. J., et al. 1997, ApJ, 474, 1

Teyssier, R. 2002, A&A, 385, 337

Thornton, K., Gaudlitz, M., Janka, H. T., & Steinmetz, M. 1998, ApJ, 500, 95

Tominaga, N. 2009, ApJ, 690, 526

Tominaga, N., Iwamoto, N., & Nomoto, K. 2014, ApJ, 785, 98

Tominaga, N., Umeda, H., & Nomoto, K. 2007, ApJ, 660, 516

Tress, R. G., Smith, R. J., Sormani, M. C., et al. 2020, MNRAS, 492, 2973

Trott, C. M., Jordan, C. H., Midgley, S., et al. 2020, MNRAS, 493, 4711

Truelove, J. K., Klein, R. I., McKee, C. F., et al. 1997, The Jeans Condition: A New Constraint on Spatial Resolution in Simulations of Isothermal Self-gravitational Hydrodynamics, doi:10.1086/310975

Tseliakhovich, D., & Hirata, C. 2010, Phys. Rev. D, 82, 083520

Tumlinson, J. 2006, ApJ, 641, 1

Turk, M. J., Oishi, J. S., Abel, T., & Bryan, G. L. 2012, ApJ, 745, 154

Umeda, H., & Nomoto, K. 2003, Nature, 422, 871

Valentini, M., Chiappini, C., Bossini, D., et al. 2019, A&A, 627, A173

Venumadhav, T., Dai, L., Kaurov, A., & Zaldarriaga, M. 2018, Phys. Rev. D, 98, 103513

Vikaeus, A., Zackrisson, E., & Binggeli, C. 2020, MNRAS, 492, 1706

Visbal, E., Barkana, R., Fialkov, A., Tseliakhovich, D., & Hirata, C. M. 2012, Nature, 487, 70

Visbal, E., Bryan, G. L., & Haiman, Z. 2017, MNRAS, 469, 1456

—. 2020, arXiv e-prints, arXiv:2001.11118

Visbal, E., Haiman, Z., & Bryan, G. L. 2015, MNRAS, 453, 4456

—. 2016, MNRAS, 460, L59

—. 2018, MNRAS, 475, 5246

Vogelsberger, M., Genel, S., Springel, V., et al. 2014, Nature, 509, 177

von Neumann, J. 1947, NDRC, Div. B, Report AM-9

Walch, S., Girichidis, P., Naab, T., et al. 2015, MNRAS, 454, 238

Watson, D., Hansen, C. J., Selsing, J., et al. 2019, Nature, 574, 497

Whalen, D., Abel, T., & Norman, M. L. 2004, ApJ, 610, 14

Whalen, D., van Veelen, B., O'Shea, B. W., & Norman, M. L. 2008, ApJ, 682, 49

Whalen, D. J., Even, W., Frey, L. H., et al. 2013a, ApJ, 777, 110

Whalen, D. J., Even, W., Lovekin, C. C., et al. 2013b, ApJ, 768, 195

Wise, J. H., & Abel, T. 2008, ApJ, 685, 40

—. 2011, MNRAS, 414, 3458

Wise, J. H., Turk, M. J., Norman, M. L., & Abel, T. 2012, ApJ, 745, 50

Wollenberg, K. M. J., Glover, S. C. O., Clark, P. C., & Klessen, R. S. 2020, MNRAS, 494, 1871

Woosley, S. E., & Heger, A. 2021, ApJ, 912, L31

Wouthuysen, S. A. 1952, AJ, 57, 31

Wright, E. L. 2006, PASP, 118, 1711

Xu, H., Ahn, K., Norman, M. L., Wise, J. H., & O'Shea, B. W. 2016a, ApJ, 832, L5

Xu, H., Norman, M. L., O'Shea, B. W., & Wise, J. H. 2016b, ApJ, 823, 140

Xu, H., Wise, J. H., Norman, M. L., Ahn, K., & O'Shea, B. W. 2016c, ApJ, 833, 84

Yoon, J., Beers, T. C., Placco, V. M., et al. 2016, ApJ, 833, 20

Yoon, S.-C., Dierks, A., & Langer, N. 2012, A&A, 542, A113

Yoshida, N., Omukai, K., Hernquist, L., & Abel, T. 2006, ApJ, 652, 6

Youakim, K., Starkenburg, E., Aguado, D. S., et al. 2017, MNRAS, 472, 2963

Youakim, K., Starkenburg, E., Martin, N. F., et al. 2020, MNRAS, 492, 4986

Zarka, P., Girard, J. N., Tagger, M., & Denis, L. 2012, in SF2A-2012: Proceedings of the Annual meeting of the French Society of Astronomy and Astrophysics, ed. S. Boissier, P. de Laverny, N. Nardetto, R. Samadi, D. Valls-Gabaud, & H. Wozniak, 687–694

Works Created

The following works have been publish or submitted under my authorship or co-authorship during the preparation of this thesis

Chen, L.-H., Magg, M., Hartwig, T., et al. 2022, arXiv e-prints, arXiv:2202.01220

Hansen, C. J., Koch, A., Mashonkina, L., et al. 2020, A&A, 643, A49

Jaura, O., Magg, M., Glover, S. C. O., & Klessen, R. S. 2020, MNRAS, 499, 3594

Magg, M., Klessen, R. S., Glover, S. C. O., & Li, H. 2019, MNRAS, 487, 486

Magg, M., Schauer, A. T. P., Klessen, R. S., et al. 2021a, arXiv e-prints, arXiv:2110.15372

Magg, M., Nordlander, T., Glover, S. C. O., et al. 2020, MNRAS, 498, 3703

Magg, M., Reis, I., Fialkov, A., et al. 2021b, arXiv e-prints, arXiv:2110.15948

Rydberg, C.-E., Whalen, D. J., Maturi, M., et al. 2020, MNRAS, 491, 2447

Tarumi, Y., Hartwig, T., & Magg, M. 2020, ApJ, 897, 58

Acronyms

ΛCDM Λ cold dark matter. 2–4

4MOST the 4-metre Multi-Object Spectroscopic Telescope. 147

A-SLOTH Ancient Stars and Local Observables by Tracing Haloes. 37, 39, 41, 42, 145, 146, 148

BAO Baryon Acoustic Oscillation. 3

CCSN core-collapse supernova. 12, 13, 15, 27, 35, 46, 67, 74

CEMP carbon enhanced metal-poor. 32, 33, 61, 71, 74, 78

CFL Courant-Friedrichs-Levi. 20, 21, 46

CMB cosmic microwave background. 3, 28–30, 147

ELT Extremely Large Telescope. 147

EMP extremely metal-poor. 31, 32, 35, 52, 53, 55–61, 72, 83, 100, 101, 104, 107, 145

HMF halo mass function. 3, 39, 119, 131

IGM intergalactic medium. 5, 28, 29, 38, 42, 147

IMF initial mass function. 18–20, 22, 25, 26, 29, 39, 53–55, 57–60, 88, 105, 106, 117, 118, 129, 135, 137, 138, 144, 146, 147

ISM interstellar medium. 6, 13, 15, 16, 18, 26, 35

JWST the James Webb Space Telescope. 27, 148

LIGO Laser Interferometer Gravitational-Wave Observatory. 30

LTE local thermal equilibrium. 28

LW Lyman-Werner. 4, 5, 22, 38, 42, 95, 106, 117, 129, 131, 137

PISN pair-instability supernova. 12, 14, 15, 27, 30, 35, 36, 47, 48, 67, 84, 88, 89, 100, 103–107, 145

Sprai Simplex Photon Radiation in the Arepo Implementation. 48, 49, 88, 147

SFR star formation rate. 16, 39, 124, 130–132

SKA square kilometre array. 29, 114, 147

SN supernova. 8, 10–15, 23–25, 27, 33–36, 41, 42, 47, 48, 61–74, 76–81, 83–89, 91–98, 100–109, 111, 113, 116–120, 136–139, 144–146

SPH smoothed particle hydrodynamics. 44

UMP ultra metal-poor. 53, 55–58, 60

WEAVE the William Herschel Telescope Enhanced Area Velocity Explorer. 147

WFIRST wide-field infrared survey telescope. 27